Micromachining and Modeling of Focused Field Emitters for Flat Panel Displays

by

Leonard Dvorson

B.S., Physics, California Institute of Technology, 1996
M.S. Electrical Engineering, Massachusetts Institute of Technology, 1999

SUBMITTED TO THE DEPARTMENT OF ELECTRICAL ENGINEERING AND COMPUTER SCIENCE IN PARTIAL FULFILLMENT OF THE REQUIREMENTS FOR THE DEGREE OF

DOCTOR OF PHILOSOPHY
IN
ELECTRICAL ENGINEERING AND COMPUTER SCIENCE
AT THE
MASSACHUSETTS INSTITUTE OF TECHNOLOGY

SEPTEMBER 2001

© Massachusetts Institute of Technology. All rights reserved

Signature of Author________________________________
Department of Electrical Engineering and Computer Science
August 6, 2001

Certified by________________________________
Akintunde Ibitayo (Tayo) Akinwande
Thesis Supervisor

Accepted by________________________________
Arthur C. Smith
Chairman, Department Committee on Graduate Students

BARKER

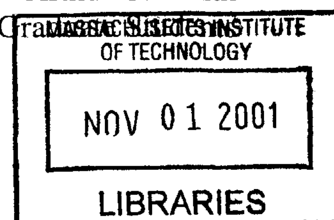

Micromachining and Modeling of
Focused Field Emitters for Flat Panel Displays

by

Leonard Dvorson

Submitted to the Department of Electrical Engineering and Computer Science
on August 5, 2001 in Partial Fulfillment of the
Requirements for the Degree of Doctor of Philosophy in
Electrical Engineering and Computer Science

ABSTRACT

We present a comprehensive study of field emitter arrays with or without an integrated focus electrode. The former configuration is referred to as field emitter with integrated focus (IFE-FEA) or double-gate FEA (DG-FEA). The main application of IFE-FEA is to improve the resolution of field emission displays (FEDs).

We developed the first analytical model of conical field emitters that captures all details of device geometry and produces quantitatively accurate closed-form expressions for the FN coefficients.

A novel CMP-based process for making IFE-FEA is presented. We obtained devices with gate and focus apertures of 0.8 and 1.2 μm diameter, respectively, which is 1.5 times smaller than in any previously reported IFE-FEA.

Single-gate FEAs whose gate was identical to the lower gate of the IFE-FEA were also fabricated. Their emission current was 100 nA/tip at 45 V; for IFE-FEAs with the gate and focus biased at the same potential ($V_G=V_F$) this figure was 100 nA/tip at 42 V, in agreement with the analytical model. It was deduced that the tip radius of curvature (ROC) is 2.4-3.6 nm. Analytical model, numerical simulation, and TEM micrographs all gave tip ROC values in this range.

We generalized the FN equation to IFE-FEA and used 4-terminal measurements to determine gate and focus field factors, β_G and β_F. Their ratio was found to vary from 0.15 (emission current independent of focus voltage) to 2.7. We demonstrated via numerical simulation that this ratio is probably determined by the degree of gate shielding of the tip.

We studied electron beam collimation with lowering V_F at different values of V_G. It was observed that the optimal V_F is about $0.25V_G$. Beam collimation was also studied as a function of cathode-anode separation – a novel experiment. From these measurements we deduced horizontal velocity of electrons and determined that it is practically equal to zero when the beam is optimally collimated. Under optimal collimation, diameter of the spot size produced by a 5x5 array with a 40x40 μm^2 footprint on the phosphor screen biased at 5kV and located 15 mm away was at most 50 μm.

Thesis Supervisor: Akintunde Ibitayo (Tayo) Akinwande
Associate Professor of Electrical Engineering

ACKNOWLEDGEMENTS

In completing graduate school, and with it my formal education, I remain indebted to many... First and foremost are the following (sans the banks):

My research advisor, Tayo Akinwande. For offering guidance, encouragement, cultural discourse, and maybe a little push now and then. And of course for blessing this writ with his John Hancock.

MTL staff. For keeping this place up and running. Without you, our work would be purely theoretical.

Students in our group. David Pflug for helping me out in the beginning and for building the superb test system used for the measurements in this work; Meng Ding for many useful discussions; Guobin Sha for being remarkably speedy in providing Matlab code to improve this thesis; Ching-Yin Hong for taking TEMs; and John (officially Ioannis) Kymissis for "living to help people," in particular me with taking measurements and SEMs.

Students not in our group. Andy Fan, Jim Fiorenza, Isaac Lauer, Fletch Meyer, Samuel Mertens, and Eric Deutsch for help and friendship. Also, my ex-roommate, Tony Chobot, for friendship and support.

Carolyn Collins, For wonderful administrative help.

My thesis committee, Professors Jeff Lang and Terry Orlando. For useful critique.

My mother. For too many things.

My father. For a lot of things.

And finally, *my teachers at Caltech, particularly my undergraduate research advisor, Professor Michael Roukes.* For generously sharing their time, knowledge, and talent. Things I learned in their lectures and in Michael's lab have proved invaluable in my graduate studies.

TABLE OF CONTENTS

1 INTRODUCTION 9

1.1 THE FIELD EMISSION DISPLAY 9
1.2 THE TRADE-OFF PROBLEM 10
1.3 DIVERGENCE OF THE ELECTRON BEAM PRODUCED BY FIELD EMISSION FROM SHARP TIPS 11
1.4 PROPOSED APPROACH 14
1.5 THESIS OUTLINE 16
1.6 CHAPTER SUMMARY 16

2 GEOMETRY OF THE FOCUS ELECTRODE – DESIGN AND PRIOR WORK 19

2.1 ELECTRON OPTICS AND MICROMACHINED ELECTRON LENSES 19
2.2 POSITION OF THE FOCUS ELECTRODE IN IFE-FEA 22
2.3 PRIOR WORK IN IFE-FEA FABRICATION 23
2.3.1 Global In-Plane Focusing Structure 23
2.3.2 Local Out-of-Plane and Global Focusing Structures with Silicon tips 23
2.3.3 Global Out-of-plane Focusing with Metal Tips 23
2.3.4 Local Out-of-Plane Focusing with Metal Tips 24
2.3.5 External Focusing Grid 25
2.3.6 Proximity Focusing 26
2.4 CHAPTER SUMMARY 26

3 BOWLING PIN MODEL OF CONICAL FIELD EMITTERS 29

3.1 FEA MODELING – OVERVIEW OF PRIOR WORK 29
3.2 THE BOWLING PIN MODEL (BPM) FOR A SINGLE GATE EMITTER 34
3.2.1 The Bowling Pin Structure and Its Equipotentials 34
3.2.2 IV Equation for a Conical Field Emitter 37
3.2.3 Calculation of Gate Capacitance 39
3.2.4 Dependence of Fower-Nordheim Coefficients on Device Geometry: Summary and Comparison with Other Models 44
3.3 EXTENSION OF THE BOWLING PIN MODEL TO FIELD EMITTERS WITH FOCUSING ELECTRODE 48
3.3.1 Potential of Two Charged Rings in the Presence of a Grounded Cone 48
3.3.2 Derivation of Capacitance Coefficients 49
3.3.3 Derivation of the Gate and Focus Field Factors, β_G and β_F. 50
3.3.4 Trajectory Calculations 51
3.4 CHAPTER SUMMARY 53

4 FABRICATION OF IFE-FEA 55

4.1 FORMATION OF 3-MICRON TALL SILICON TIP 55
4.2 DEPOSITION, PLANARIZATION AND ETCHBACK OF GATE INSULATOR 56
4.3 OXIDATION SHARPENING OF THE TIP AND FORMATION OF THE GATE ELECTRODE 57

4.4 DEPOSITION, PLANARIZATION AND ETCHBACK OF THE FOCUS INSULATOR AND FORMATION OF THE FOCUS ELECTRODE ... 58
4.5 CHAPTER SUMMARY ... 61

5 IV CHARACTERISTICS OF IFE-FEA ... 63

5.1 MEASUREMENT SETUP ... 63
5.2 IV CHARACTERISTICS OF SINGLE-GATE FEAS ... 64
5.2.1 Device Description ... 64
5.2.2 Turn-on Voltage ... 65
5.2.3 Measurement and Analysis of Fowler-Nordheim Coefficients ... 66
5.3 IV CHARACTERISTICS OF DOUBLE-GATED FEAS (IFE-FEAS) ... 73
5.3.1 Device Description ... 73
5.3.2 Three-Terminal Measurements ... 74
5.3.3 Four-Terminal Measurements ... 78
5.3.4 Investigation of Space Charge at Focus Voltages below 10 V ... 87
5.4 CHAPTER SUMMARY ... 90

6 OPTICAL CHARACTERIZATION OF IFE-FEA ... 93

6.1 MEASUREMENT SETUP FOR IMAGE ACQUISITION ... 93
6.2 COLLIMATION OF THE ELECTRON BEAM AT DIFFERENT VALUES OF GATE VOLTAGE ... 96
6.3 COLLIMATION OF THE ELECTRON BEAM AT DIFFERENT VALUES OF CATHODE-ANODE SEPARATION — REDUCTION OF HORIZONTAL VELOCITY ... 100
6.4 CHAPTER SUMMARY ... 102

7 THESIS SUMMARY AND SUGGESTIONS FOR FURTHER WORK ... 103

7.1 THESIS SUMMARY ... 103
7.2 MAIN CONTRIBUTIONS ... 105
7.3 SUGGESTIONS FOR FURTHER WORK ... 106

8 APPENDIX 1. ... 107

9 APPENDIX II. ... 115

BIBLIOGRAPHY ... 120

1 INTRODUCTION

1.1 The Field Emission Display

Field emission displays (FEDs) promise the best of display worlds – performance and portability [1, 2, 3, 4, 5, 6,]. The standard for display performance is set by cathode ray tubes (CRTs), which are found in almost every TV and desktop monitor. But for reasons to be explained shortly, the CRT is inherently bulky. (Ever tried moving a TV?) So when sophisticated portable electronics, particularly laptop computers, required thin and light screens, manufacturers turned to liquid crystal displays, popularly known as LCDs. Although space-saving LCDs are now starting to replace CRTs even in desktop monitors, the LCD technology is at an inherent performance disadvantage. While in the CRT – and in the FED – each pixel acts as an independent light source, pixels of an LCD act as spatial light modulators or valves that either block or transmit light coming from a lamp in the back. Light that gets blocked is effectively lost, which results in reduced brightness, lower luminous efficiency, and smaller viewing angle. Moreover, LCDs are fundamentally limited to operation within a rather narrow temperature range, precluding their use in aerospace and other similarly demanding applications. FEDs suffer from no such limitation [7, 8, 9]. Thus, although performance of LCDs has recently been improved – and prices lowered – the fundamental advantages of the FED make it worth pursuing [10, 11, 12, 13, 14, 15, 16, 17]. Of course, as a new technology, the FED also has room for improvement, which precisely the subject at hand.

The FED is sometimes described as "a flat CRT" because the two are so similar in concept: an electron beam strikes the phosphor where hole-electron pairs are created and emissive recombination of electrons produces light [18, 19, 20, 21]. However, unlike the CRT, in which the cathode consists of a single electron gun that is raster scanned across the display, the FED employs an addressable array of miniature electron guns. Since each pixel of the FED has a dedicated electron source, there is no need to raster. This makes it possible to drastically reduce cathode-anode separation and obtain 'a thin CRT.'

As can be seen in **Figure 1-1**, a mini electron gun is itself an array of microscopic field emitters. The field emitter of the type examined in this work consists of a sharp cone centered in an annular opening of the gate conductor. When the gate is biased relative to the emitter, by laws of electrostatics, very high electric field appears at the cone apex and nearby. Once the gate voltage is sufficiently positive, this field is strong enough to cause field emission of electrons from the tip. This process will be discussed in Section 1-3. Operation of the display as a whole is achieved by periodically activating each electron gun through a matrix-addressing scheme driven by specialized control electronics [22, 23, 24, 25, 26, 27].

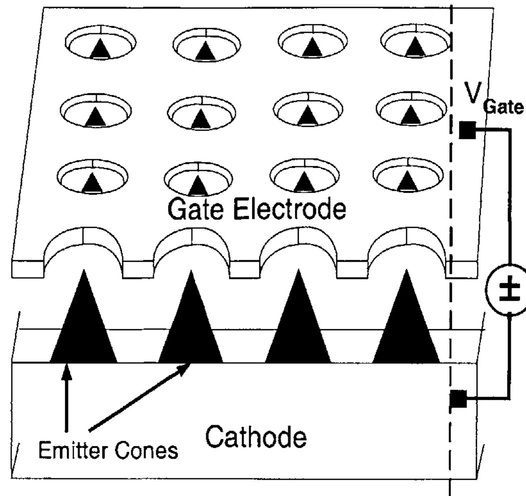

Figure 1-1. Structure of a miniature electron gun composed of a 4x4 array of field emitters.

1.2 The Trade-off Problem

The space the between the cathode and the screen in the FED must be kept under vacuum, and the screen itself has to be made of fairly thin glass. This necessitates supporting the screen with insulating spacers positioned between the pixels. Spacers must be thin and transparent, which usually means they are fairly leaky dielectrics with breakdown fields of about 1 V/μm [28, 29, 30, 31],. Thus, if the spacer is 100 μm thick, the anode voltage cannot exceed 500 V.

Screen voltage in the CRT is typically in the 5-30 kV range. The CRT employs what can be called high-voltage phosphors, which offer high luminous efficiency, high brightness, and long lifetime. But if the anode voltage is reduced below ~1 kV, electrons arriving at the screen would have insufficient energy to activate the phosphor and produce light. Furthermore, to carry away excess charge, the backside of the phosphor is coated with a thin layer of aluminum, which would absorb lower energy electrons. To make the FED screen operate at 500 V, high-voltage phosphor is replaced with low voltage phosphor [32, 33, 34, 35, 36, 37, 38, 39, 40, 41, 42] that can be activated by 500 eV electrons, and the aluminum is removed from the phosphor backside and replaced with a transparent and conducting indium-tin oxide (ITO) layer in the front (**Figure 1-2**). Unfortunately, ITO has lower conductivity than aluminum, which leads to gradual charge accumulation in the phosphor. Since phosphor lifetime is effectively determined by the total accumulated charge, high resistance of the LTO layer drives LVF into an early grave. The low voltage phosphor is also less efficient because a fraction of low energy electrons undergo recombination near the surface of the phosphor, and surface recombination processes are usually non-radiative. Moreover, the removed aluminum layer also served to double the efficiency by reflecting back light that was emitted downward. Thus, as compared to the CRT screen, the low voltage FED has lower efficiency, lower brightness and shorter screen lifetime.

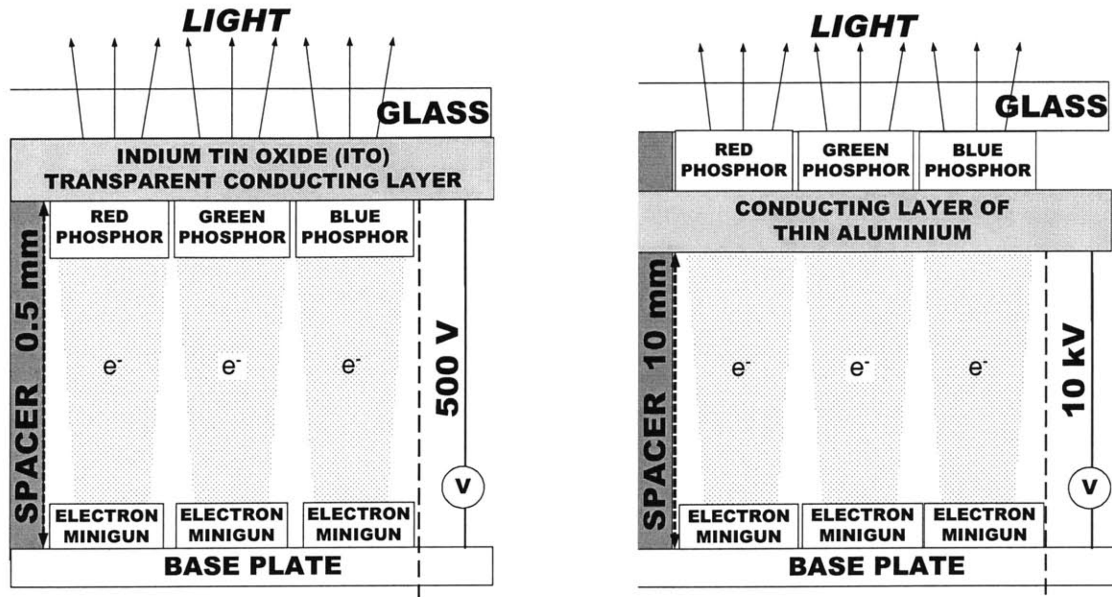

Figure 1-2. Low voltage FED (left) vs. high voltage FED.

Conversely, to make the FED screen operate at 10 kV, the spacer thickness needs to be increased to 1 mm. However, the electron beam produced by field emitters is intrinsically divergent because the spherical field near the tip imparts horizontal velocity to electrons emitted at points away from the apex. (The reasons for beam divergence will be explored in greater detail in the next section.) Thus, the thicker the spacer the larger the spot size produced on the phosphor screen by the field emission beam. Larger spot size translates into larger pixels and hence lower resolution. Thus, in today's FEDs there exists a tradeoff: luminous efficiency, brightness, and screen lifetime *versus* display resolution. The goal of our work is to overcome this limitation.

1.3 Divergence of the Electron Beam Produced by Field Emission from Sharp Tips

The first reason for the divergence of the field emission beam is inherent in the nature of field emission from sharp tips, which now examine.

The theory of field emission from metals was put forth in 1928 in the seminal paper of R. Fowler and L. Nordheim [43], and has since become a classic re-stated and extended in many subsequent publications [44, 45, 46, 47, 48]. Electrons in a metal are considered to be in a square potential well in relation to the surrounding vacuum, as shown in **Figure 1-3**. If the vacuum is taken to be at zero potential, the most energetic electrons in the metal, i.e. those at or near the Fermi energy, have the energy of -φ, where φ is the work function. The metal-vacuum interface is usually taken to be the plane x = 0. When there is a strong electric field, *E*, at the surface of the metal, the classically forbidden region, in which even the most energetic electrons have negative energy, is changed from the half plane $x > 0$ to the interval $0 < x < |\varphi/E|$. Typically, metal workfunctions are 4-5 eV, and electric fields needed to induce emission are 3-5 V/nm, so that the width of the forbidden region for Fermi energy electrons is no more than 1-2 nm.

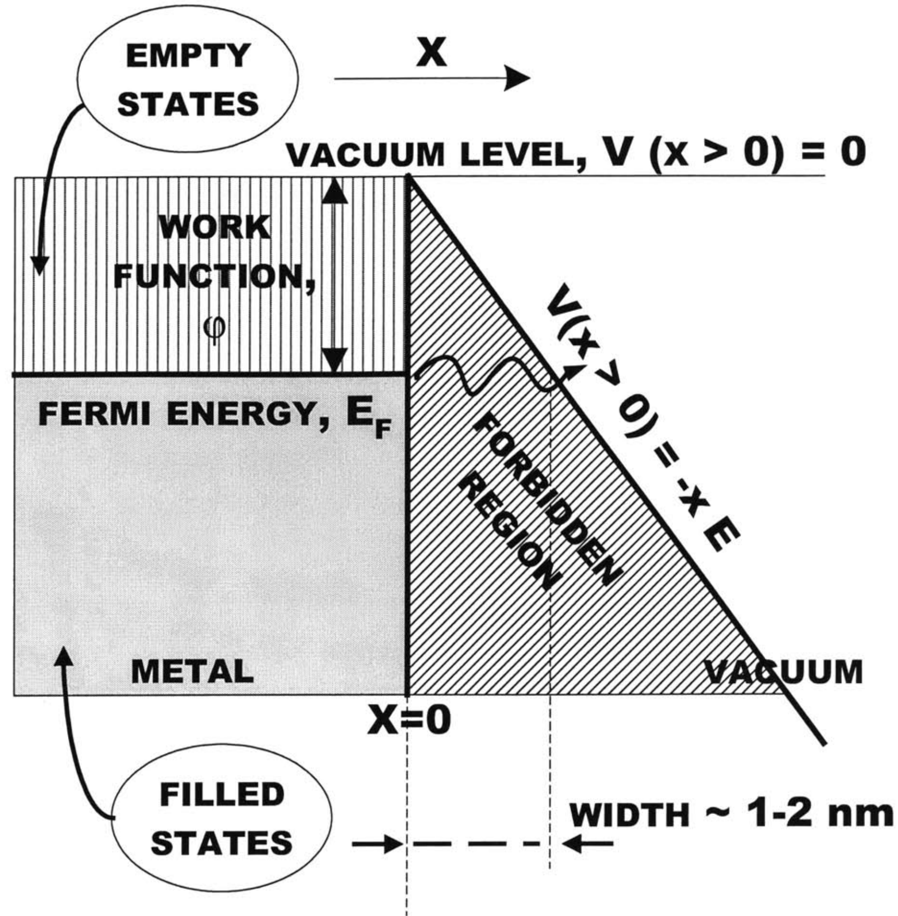

Figure 1-3. Electrons in the metal are in a potential well. For electrons at the Fermi energy, the height of the barrier is given by the work function. Application of a strong electric field, E, at the surface of the metal, changes the shape of the barrier from V(x>0) = 0 to V(x>0) = - xE. It is now possible for the electron to tunnel through the forbidden region and escape from the metal.

It is customary to define:

$W = \frac{1}{2}mv_x^2 + V\left(x\right)$: x-part of the electron energy

$N\left(W'\right)dW'$ – number of electrons incident on the barrier per unit time per unit area with x-energy W between W' *and* $W'+dW'$, referred to as "supply function"

$D(W')$ – probability that an electron incident on the barrier with the x-energy equal to W' will be transmitted, referred to as "transmission coefficient"

Then, the number of electrons that tunnel through the barrier per unit time, per unit area, i.e. the local field emission current density is given by:

$$J = \int_{-\varphi-E_F}^{\infty} D\left(W'\right) N\left(W'\right) dW'$$

With several approximations, the integral is evaluated to

$$J(E)=\frac{1.27273\times10^{-6}e^{9.86814/\sqrt{\varphi}}}{\varphi}E^2\times\ \exp\left[-\frac{6.5265\times10^7\ \varphi^{3/2}}{E}\right]\equiv a_J(\varphi)E^2\times\exp\left[-\frac{b_J(\varphi)}{E}\right]$$

$$a_J(\varphi)\equiv\frac{1.27273\times10^{-6}e^{9.86814/\sqrt{\varphi}}}{\varphi};\qquad b_J(\varphi)\equiv6.5265\times10^7\ \varphi^{3/2}$$

This is the well-known Fowler-Nordheim (FN) equation. A reader may wonder about the effect of temperature on field emission. Although the tip obviously heats up during field emission, the temperatures never get high enough to appreciably alter the energy distribution of electrons. Thus, this expression derived using the zero temperature Fermi-Dirac distribution, is valid in our application [44].

The preceding equation is valid metals. While field emission from semiconductors presents a number of additional theoretical issues [46], experimental data for emission from silicon still follows this equation with one correction: the workfunction needs to be replaced by electron affinity because in semiconductors the most energetic electrons are at the bottom of the conduction band, not at the Fermi energy.

We are now ready to explain the origin of the inherent angular spread in the emission beam. In real emitters the solid-vacuum boundary is not a plane, as shown in **Figure 1-3**, but a curved, almost spherical, surface. On the other hand, the width of the tunneling barrier (1-2 nm) is much less than the curvature of emitters that we will be dealing with (10-15 nm). Therefore, at any given point on the emitter, a curved surface can be replaced by a plane tangent to the emitter surface at that point, which brings us back to the situation in **Figure 1-3**. [There have been reports in the literature on extending the FN theory to cases where the curvature of the emitter is comparable to the width of the tunneling barrier [48,49]; but to the best of the author's knowledge, there has been no application to experimental data.] Electrostatics dictates that the electric field is maximized at the apex of the tip; however, it is also large enough for field emission at points close to the apex. Thus, as shown in **Figure 1-4 A,** emission is taking place from the points that are, for example, 10°, 20°, and 30° from vertical. Emitted electrons are accelerated by the local electric field, which is directed normal to the tip within a few tip radii of the tip. In this way, all electrons that are not emitted directly from the apex acquire a horizontal velocity component, and thus introduce an angular spread into the field emission beam.

After electrons move more than a few tip radii away from the emitter, their horizontal velocity is further amplified by the gate electrode. To see why this happens, consider an electron in the plane of the gate opening, for example to the right of the center, as depicted in **Figure 1-4 B**. The charge on the rim of the gate is labeled Q_{TOT}. It is positive because the gate is biased above the cathode. The charge to the left of the electron, designated Q_L, attracts the electron toward the axis, while the charge to the right of the electron, Q_R, pulls it away from the axis. While Q_L is greater than Q_R, the difference between the two is linear in the distance between the electron and the center of the opening, designated **d** in the figure. However, the forces they exert on the electron vary as the inverse square of electron's distance from the center. Thus, the pull of Q_R,

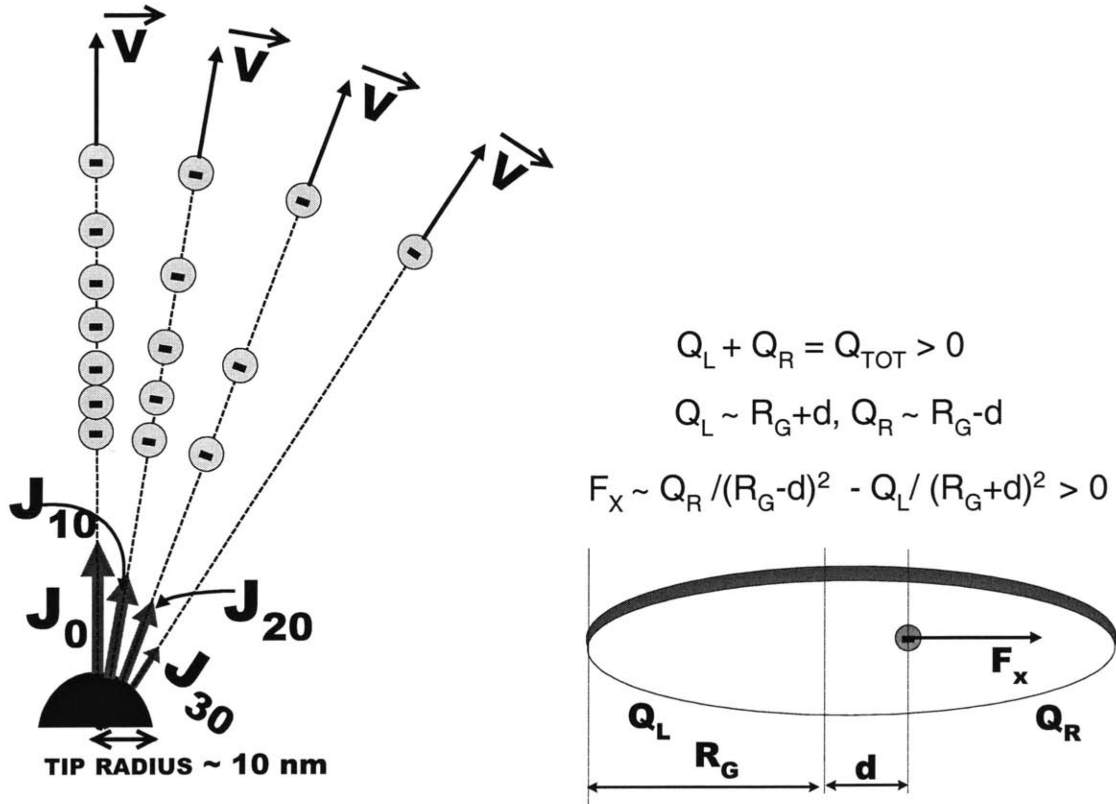

Figure 1-4. Origins of angular spread of the field emission beam. (A) Emission current density at different point on the tip. Non-zero emission from points other than the apex introduces an inherent angular spread into the field emission beam because electrons emitted at non-zero angles acquire horizontal velocity from the tip field. (B) An electron in the plane of the positively charged gate opening experiences a horizontal force directed away from the center, which further amplifies its horizontal velocity.

which is smaller but on average closer to the electron than Q_L, outweighs that of Q_L, and the net horizontal force on the electron is directed away from the z-axis.

It is clear by now that there is no way to prevent the beam spreading from happening in the first place, we can only attempt to re-collimate the beam at a later stage. A way to do this will be developed in the next section.

1.4 Proposed Approach

If an electron in the opening of a positively charged gate electrode experiences an outward horizontal force, then reversing the charge on the gate electrode should produce an inward horizontal force. Thus, the electrons' horizontal velocity can be reduced, or completely eliminated. If electrons have zero horizontal velocity, they travel vertically up to the anode regardless of how far away the anode is. In other words, once the electron beam has been collimated, the cathode anode distance can be increased without incurring pixel-to-pixel crosstalk and the resultant loss of resolution. And increased cathode-anode separation would make it possible to employ the more efficient high-voltage scheme. In this way, collimation of the field emission beam would allow the

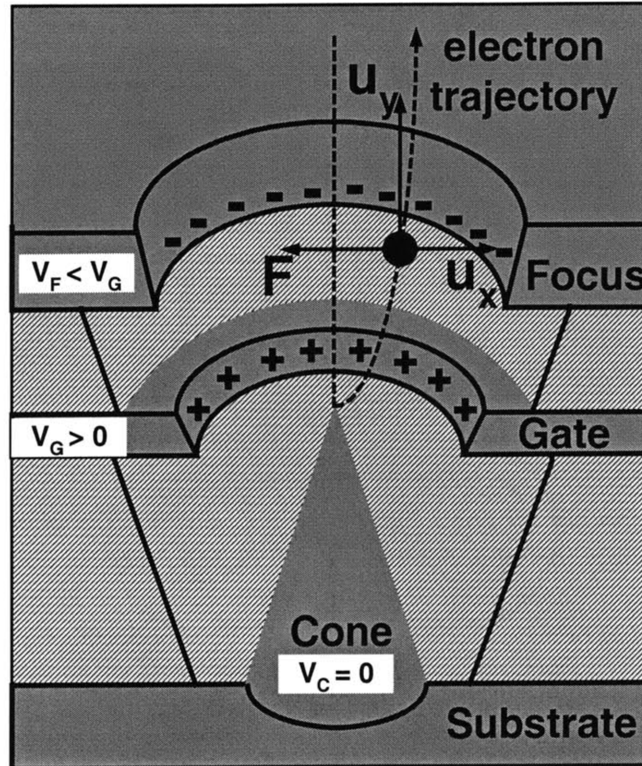

Figure 1-5. Negative charge on the rim of the focus electrode exerts a horizontal force, F. of the electron that is directed toward the z-axis. This has the effect of collimating the electron beam.

FED to employ HVF and achieve higher luminous efficiency, brightness, and screen lifetime without sacrificing resolution.

Of course, the charge on the gate cannot be negative; otherwise there would be a negative field at the grounded emitter tip and hence no field emission. However, it is entirely possible to add a second gate, stacked on top of the first one as shown in **Figure 1-5**. The second gate will be called the focus, in keeping with the literature, although strictly speaking it does not focus the electron beam into a single point.
The name probably reflects the appearance of a light spot produced by on the phosphor screen by an emitter with integrated focus. When the focus bias is lowered and the electron beam is collimated, a dim, large spot about 2 mm in diameter is reduced to a much brighter and smaller spot (less than 0.1 mm in some cases). Superficially, it appears that the electron beam is being focused on the screen.

To make the focus electrode accumulate negative charge, one simply biases it sufficiently below the gate. Although several different placements of the focus electrode are possible and will be discussed in the next chapter, the intuitive geometry in Figure 1-5 has been shown to be the most effective in beam collimation [50]. The objective of this work will be modeling, fabrication, and characterization of electrical and optical performance of this structure, which we call Field Emitter Array with Integrated Focus Electrode or IFE-FEA.

1.5 *Thesis Outline*

In more detail, the outline of this work is as follows:

In **Chapter 2** starts with the framework of macroscopic electron optics, then examines different geometries for IFE-FEA, and concludes with a summary of IFE-FEAs that have been reported in the literature.

Chapters 3-6 contain original contributions of this thesis. With the exceptions of Matlab numerical simulations and some micrographs, credit for which is carefully attributed, all the contents constitute original work of the author.

In **Chapter 3** we develop an analytical model for conical field emitters with a focusing electrode. The model provides formulas that show effects of device geometry on performance, which is useful for device design and interpreting the data.

Chapter 4 will discuss fabrication of arrays of silicon field emitters with integrated focusing electrode. Our novel process makes it possible to achieve devices with dimensions that are several times smaller than those of any previously reported IFE-FEAs.

Chapters 5 and 6 are devoted to presentation and analysis of the data. **Chapter 5** deals with IV characteristics and overall electrical characterization. **Chapter 6** examines reduction of spot size as a function of lower focus bias, i.e. collimation of the field emission beam by the focus electrode.

A summary of the thesis and suggestions for further work are given in **Chapter 7.**

1.6 Chapter Summary

The purpose of this chapter was to introduce a problem, or rather a performance limitation, that exists in today's field emission displays (FEDs) and to propose a solution. This was done in **Sections 1-1 – 1-4**. In **Sections 1-1 and 1-2** we discussed the structure of the field emission display, paying particular attention to the difference between high-voltage and low voltage screens. We explained that an FED with a high voltage screen (HV-FED) would deliver superior performance in brightness, luminous efficiency, and phosphor lifetime. However, it is currently impossible to realize HV-FED because it requires large cathode anode separation. Due to an angular spread in the emission beam, increased cathode-anode separation would lead to pixel-to-pixel cross-talk and hence a loss of resolution. We then argued that if the electron beam was perfectly collimated, increased cathode-anode separation – and hence high voltage screen operation – could be effected *without loss of resolution.* The problem thus became one of collimating the field emission beam.

In **Section 1-3** we traced the reasons for beam divergence back to the physics of field emission, which was briefly reviewed, and to the electrostatic field of a circular gate

opening with a positively charged rim. Then, in **Section 1-4**, we explained how a beam could be collimated by the electrostatics of a circular gate opening with a negatively charged rim, in other words by reversing one of the two factors that produce beam divergence in the first place. Of course, the original gate must remain positively charged to produce field emission. So, in the device structure we proposed, a second gate, which we called *focus*, is added on top of the first one. When the focus is biased sufficiently below the gate, it acquires negative charge that can collimate the electron.

Finally, in **Section 1-5**, we gave an outline for the rest of the thesis: a review of the possible focusing schemes and prior work is in Chapter 2; device model is in Chapter 3; fabrication process in Chapter 4; electrical data in Chapter 5; and optical data, i.e. evidence of beam collimation by the focus, in Chapter 6. A thesis summary and suggestions for further work are in Chapter 7.

2 Geometry of the Focus Electrode – Design and Prior Work

2.1 Electron Optics and Micromachined Electron Lenses

Our task of collimating the field emission beam falls in the category of electron optics [51]. Electron optics deals with properties of beams of electrons propagating through vacuum usually in the presence of electromagnetic fields. The subject was born in the 1920's as a result of several scientific advances. First, Louis de Broglie postulated that a wavelength should be associated with moving particles, electrons in particular (1925). Then, in 1927 Hans Busch demonstrated that the action of an axially symmetric coil on electrons could be described in terms of focal length, an optical concept. Also in 1927, de Broglie's hypothesis was confirmed by experiments on electron diffraction (Davisson and Germer; Thomson and Reid). Five years later, in 1932, Ruska and Knoll built the first electron microscope. Today, in addition to scanning and transmission electron microscopes, applications of electron optics include cathode ray tubes; electron spectrometers, and by extension mass (ion) spectrometers; image converters; electron interferometers and diffraction devices; electron welding machines; and electron-beam lithography. All of these technologies rely on manipulation of electron beams by suitably placed electrostatic and magnetic fields. Typically, the fields can be used to collimate, raster (deflect), and/or focus the beam. Conductors that produce the necessary fields are known as electron lenses. Analysis of the effect that a given electron lens would have on the electron beam almost always involves calculation of electron trajectories. The most difficult part of this task is determining the field produced by the conductor system that serves as the lens. This can be done analytically, via an orthonormal expansion or the method of Green's functions, or by either of several numerical methods – FEM (finite element method), FDM (finite difference method), or BEM (boundary element method.) In our analysis in Chapter 3, we will use an orthonormal expansion.

Any particular lens design starts with the application, i.e. the effect that the lens should have on the electron beam. Suppose we want to collimate a divergent electron beam, which requires reducing the horizontal velocity of the electrons to zero. In general, that can be achieved by an electric field whose horizontal component is directed outward, i.e. away from the optical axis (the z-axis, or the axis of symmetry.) The specific magnitude and spatial dependence that the field should have in order to produce a well-collimated beam can only be determined via numerical trials. In practice, various conductor geometries and potentials are tested in the simulation environment for their effectiveness in collimating electron beams. Although numerical simulation and complicated analytical methods are the only ways to quantitatively describe any electron lens, some insight into the field pattern created by a given conductor system can be gleaned from simple geometrical arguments.

Consider the electron lenses shown in **Figure 2-1.** A plane with a circular opening (**Figure 2-1A**) can be expected to produce a field pattern that peaks in the plane of the opening and then decays rapidly. A field profile that is less abrupt and offers

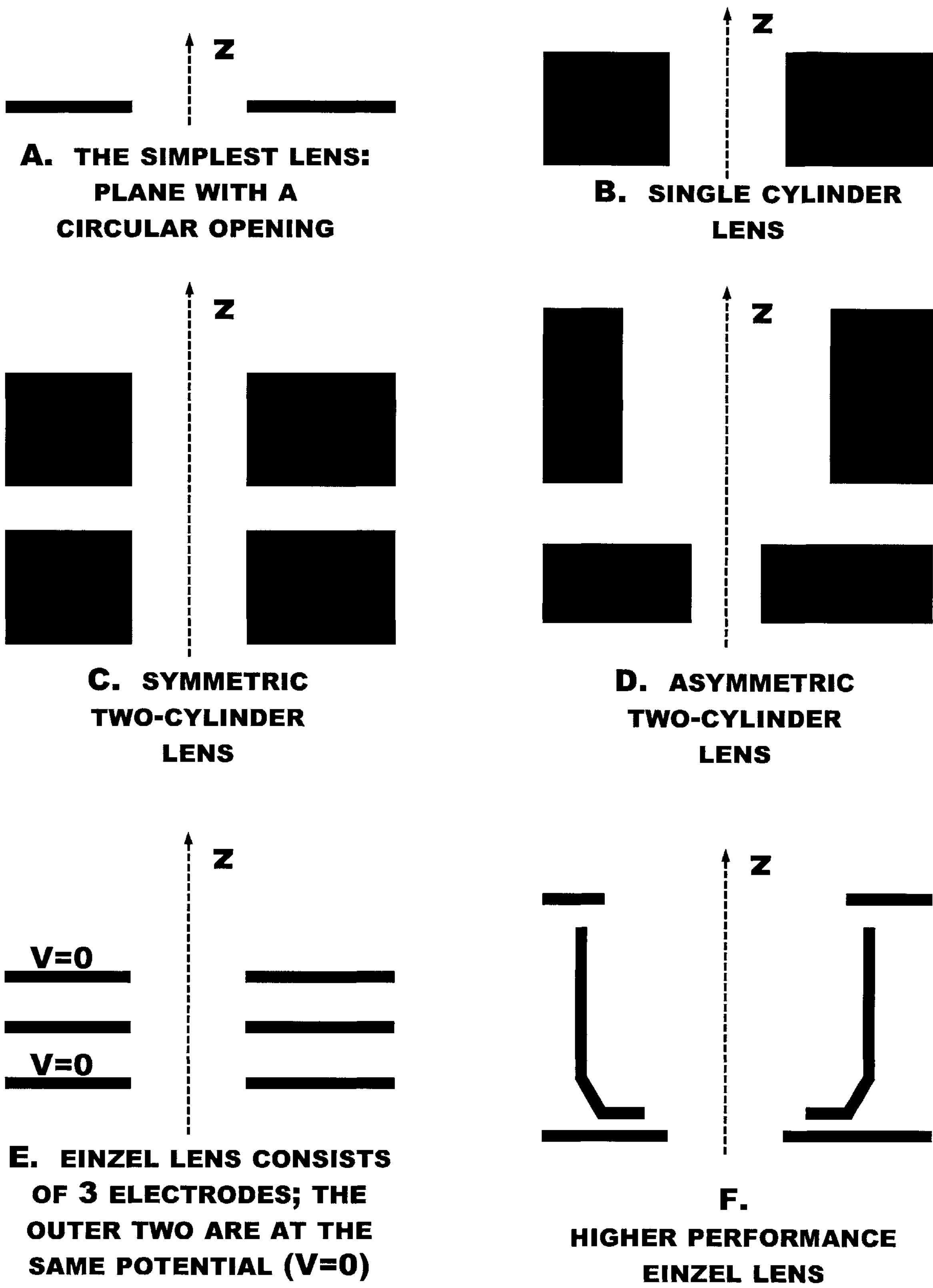

Figure 2-1. These electron lens geometries can potentially be miniaturized with micromachining. The simplest lens shown in part A is implemented in this work.

greater vertical extent can be obtained with a cylinder lens shown in **Figure 2-1B**. A two-cylinder lens in **Figure 2-1C** provides the added flexibility of changing the field by placing a different bias on the upper cylinder. If the bottom cylinder is viewed as doing most of the focusing, and the top cylinder merely provides a correction, it makes sense to make the top cylinder have larger radius and greater length, as shown in **Figure 2-1D**. This makes the field in the bore of the upper cylinder smaller in magnitude but greater in vertical extent. **Figures 2-1 E** and **F** show *einzel* or uni-potential lenses, so-called because only the center electrode has adjustable potential. Since the lens has no net accelerating or decelerating effect on the electron beam, it is easier to model in a system of several lenses. Note that although the outer two lenses are grounded, they have non-zero surface charge density due to the presence of the biased central lens and thus participate in focusing.

While an infinite variety of lenses can be fabricated for conventional applications, only the simplest designs can be successfully miniaturized at the present time. Micromachined electron lenses are still in the earliest stages of development, and our capabilities are limited. The main difficulty is fabricating conducting structures with significant vertical extent, which presents serious challenges in terms of film deposition and etching. For example, if the lens opening is 1 micron in diameter, the vertical extent for a cylindrical lens must be 2-3 microns. Metal films of that thickness tend to have large built-in stresses that cause them to peel off or warp the wafer making it extremely brittle and likely to break in subsequent processing. Moreover, etching equipment built for CMOS-compatible processing is not meant for etching through thick stacks of films and in general performs poorly in this task. This author has little experience with specialized micromachining equipment, which may be more suitable for such applications. Despite the challenges, any of the lenses in **Figure 2-1** can probably be made in today's micromachining laboratory but not in a manufacturing environment. However, this may change as equipment improves. Fortunately, as we shall see, the simplest configuration of **Figure 2-1A,** which is the one we fabricated, is sufficient for collimating the emission beam for the FED application.

2.2 Position of the Focus Electrode in IFE-FEA

Although, the geometry the focus electrode is limited to the simple plane with an opening, there are different ways to integrate it into the FEA triode. We classify them into four groups, according to focus position. As illustrated in **Figure 2-2**, the *global vs. local* distinction tells us whether each tip has a dedicated focus (local scheme), or a single focus is used to collimate emission beams from several tips (global scheme). Independently, *in-plane vs. out-of-plane* describes whether the focus is coplanar with or stacked above the gate. These schemes vary in performance and fabrication difficulty.

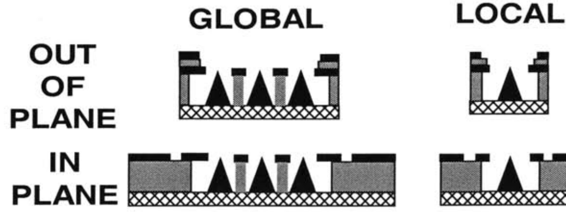

Figure 2-2. Classification of IFE-FEA according to device geometry.

We will now argue *qualitatively* that for focusing purposes the most effective device geometry is local, out-of-plane (L/OP). This has been confirmed by detailed numerical modeling [52]. The L/OP configuration has the smallest radius of the focusing aperture; thus, the focusing field is maximized, and the distance between the tip and the focus is minimized. Minimizing the tip to focus separation improves beam collimation for two reasons. One is that the path of the electron can be viewed as going from the region dominated by the divergent gate field to the region dominated by the collimating focus field. The beam is obviously collimated better when electrons pass from the gate region to the focus region sooner. Moreover, this also maximizes the time, τ, spent by the electrons in the focusing field since electron trajectories start at the tip with virtually zero velocity and are rapidly accelerated outward. It is desirable to maximize τ because it determines the total impulse provided by the focusing field in the direction parallel to the plane of the anode:

$$I_x = -e\int_{t_{Fin}-\tau}^{t_{Fin}} E_x\left[x(t),y(t)\right]dt \qquad \textbf{(2.1)}$$

The preceding considerations also suggest that for optimal focusing the vertical distance between the gate and the focus should be minimized, subject to the breakdown limit of the gate/focus insulating layer. On the downside, when the focus electrode is close to the field emitter, its negative charge will reduce the field at the tip and hence decrease emission current. This is a potentially inevitable trade-off of effective collimation and lower operating voltage. Since our stated objective is to optimize focusing, our design, modeling, and fabrication efforts were concentrated on the L/OP IFE-FEA. Moreover, since the gate is closer to the tip than the focus, we expect to be able to compensate for field reduction due to the focus by a relatively small increase in gate voltage.

Let us conclude this section with a couple of comments concerning L/IP in-plane geometries. These are usually easier to fabricate but less effective [53]. (G/IP geometries have been found to be completely inadequate for collimating FEAs larger than 2x2 [53].) While suppression of the tip field due to the focus is not a problem because the tip is shielded by the gate, operating voltage will not necessarily be lower in practical situations. The reason is that L/IP schemes have lower tip packing density, and thus require higher gate voltage to produce a given emission current *per unit area.* There is one more trade-off worth mentioning: IP geometries have no insulator between gate and focus and thus avoid the problems of gate-to-focus leakage and capacitive power dissipation ($\frac{1}{2}CV^2$). On the other hand, the lead from the gate electrode to the contact pad in the in-plane configuration, requires a break in the focus electrode; the resulting asymmetry creates some distortion in the electron beam.

2.3 Prior Work in IFE-FEA fabrication

2.3.1 Global In-Plane Focusing Structure

Cha-Mei Tang et al. [54] reported an IP global focusing structure, which has a 1x100 array enclosed between two long parallel focus electrodes. With the phosphor screen biased at 2.5 kV and placed 10 mm away, and the gate biased at 50-60 V, an unfocused image is 4-5 mm long by about 3 mm wide. With optimal focusing, obtained for focus voltages of 3-11 V, "the full width, half maximum of the image is no more than 35 microns wide," which is almost 100 times smaller. Although this structure does not hold the potential for similar performance with a 2D FEA, it serves as convincing proof of the focusing concept.

2.3.2 Local Out-of-Plane and Global Focusing Structures with Silicon tips

Excellent focusing results have been obtained by J. Itoh et. al. [55,56] with L/OP Si IFE-FEA. With the anode at 1000 V, 20 mm above the cathode, gate voltage at 80 V, and focus voltage at 50 V, the spot size diameter was about 6 mm. Under optimal focusing conditions, (focus biased at 4 V), the spot size was approximately 0.5 mm, which is five times the original array size and constitutes a reduction of more than a factor of 10. Devices also exhibited a high degree of tip-to-tip uniformity. The main drawback of Itoh's device is high operating voltage, necessitated by large gate opening (2 μm diameter), which in turn is a consequence of the fabrication process. Moreover, this process relies on vertical, non-conformal deposition making it difficult to scale to large areas. The process that we have developed allows one to achieve aperture openings that are up 4 times smaller and without relying on vertical deposition or any other 'exotic' steps. The same laboratory has also investigated performance of global focusing structures [53] and found them inadequate for FEAs larger than 2x2.

2.3.3 Global Out-of-plane Focusing with Metal Tips

In the next few sections we will discuss devices utilizing metal tips. While Si emitters are typically much more uniform – a characteristic that in general improves reliability and lowers operating voltage because all the tips are making approximately

equal contributions to the total current -- metal (typically molybdenum) tips can significantly lower display cost as they do not require a single crystal substrate. In today's commercial FEDs, cathodes are primarily made of metal tips evaporated on glass by what is known as a Spindt cone process.

Tsai et. al. [57] have reported integrating a square G/OP focusing electrode with 2x2 arrays of metal tips. With the 5 kV screen 5 mm away, and the gate biased at 60-80 V, the authors found that focusing can bring the spot size from 1.6 mm down to 0.6 mm, i.e. approx. a factor of 2.5 reduction. Using the focus electrode also reduces the emission current by a factor of 10.

2.3.4 Local Out-of-Plane Focusing with Metal Tips

This crowning achievement of my first two years at MTL (i.e. my Master's thesis) remains the only example of L/OP IFE-FEA fabricated without reliance on the silicon substrate [58,59]. I just wish it worked better... The main problem, which motivated the work to be presented next, was breakdown in the gate/focus insulator that made it impossible to run the device in the focusing mode for longer than a few seconds. Presumably, it occurred because the oxide layer was too thin (0.6 μm, c.f. **Figure 2-3**) and/or poor quality, and the operating voltages too high. The latter was due to lack of tip-to-tip uniformity. Specifically, **Figure 2-4 A** shows that the metal tip is highly non-uniform, so the array current is likely dominated by emission from sharp surface features on a few tips. This is confirmed by the fact that the total array current does *not* scale with the number of tips **Figure 2-4 B**. Metal tips, formed by thermal evaporation, are not expected to be uniform. In the industry this problem is sometimes addressed by post-processing methods (e.g. plasma etch of the tips), which are kept secret. On the other hand, silicon tips sharpened by thermal oxidation are intrinsically much more uniform, and hence have lower operating voltage.

Silicon tips are also a lot easier to model because the tip surface is smooth and can be well approximated as spherical. This a consequence of the method by which it is fabricated (thermal oxidation). In contrast, metal tips, which are formed by thermal evaporation, are not uniform at all, as shown in **Figure 2-4A**. Thus, they cannot be approximated closely with any smooth surface.

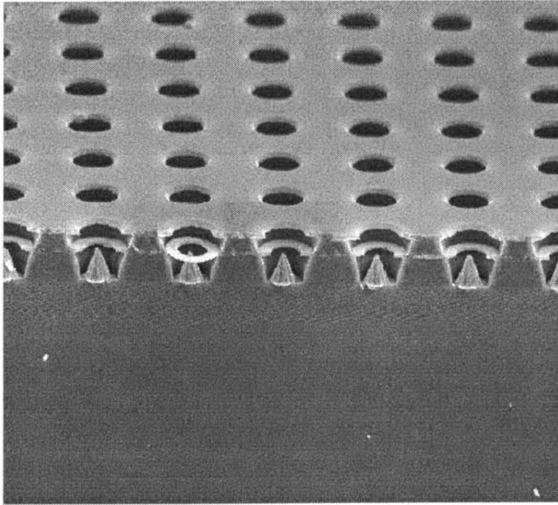

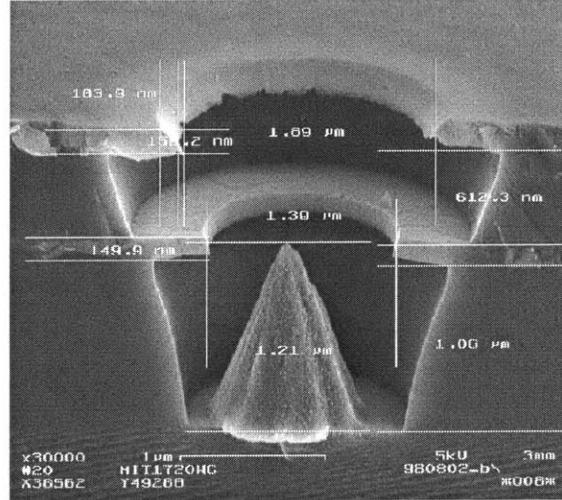

Figure 2-3. (A). L/OP metal IFE-FEA. **(B). L/OP metal IFE-FEA cone with dimensions.**

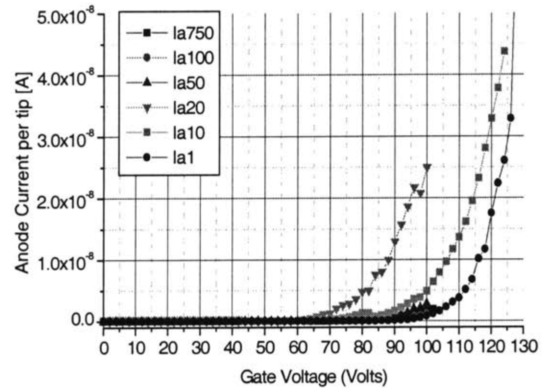

Figure 2-4 (A) Zoom-in on a sharp metal tip. **(B) IV data per tip for metal IFE FEAs of different sizes.**

2.3.5 External Focusing Grid

For completeness, we mention an approach to FED focusing attempted at Raytheon. Instead of fabricating an IFE-FEA, this work produced a fine metal grid with 70-200 µm openings that was manually mounted and aligned above the cathode. Alignment is obviously the hardest step here; in fact, the authors found only one pixel that was perfectly aligned to the corresponding opening in the focusing mesh.

Notwithstanding technical difficulties and associated higher manufacturing costs, this approach does have some advantages over IFE-FEA: The grid not only *focuses* the beam on the screen (i.e. spot size is less than grid openings) but also directly intercepts stray electrons. Moreover, the focal point can be controlled with the voltage applied to the grid. If any positive ions are created at the anode, without the grid, they would be accelerated back to the cathode and cause damage. The grid can shield the cathode from this ion bombardment. This device also avoids current suppression by the focus

electrode. Moreover, it doesn't have the difficulties involved in fabricating IFE FEA and doesn't have the additional problems of power dissipation and dielectric breakdown in the gate/focus insulator.

2.3.6 Proximity Focusing

In the conclusion, it would be useful to mention *proximity focusing*. In fact, proximity focusing involves nothing more than placing the screen very close (0.5 mm) to the cathode and using low voltages with low voltage phosphors. Acceleration due to the anode field gives the appearance of focusing. The scheme is currently the industry favorite because of its simplicity. Rather than achieving high voltage operation through IFE-FEA and greater cathode/anode separation, efforts are focused on improving dielectric spacers and vacuum envelope to enable the display to withstand higher anode fields.

2.4 Chapter Summary

This chapter examined the focusing approach in greater detail. We started from the standpoint of electron optics and lenses used to collimate electron beams in macroscopic systems. We pointed out that although we have only miniaturized the simplest lens design, other slightly more complicated geometries maybe within reach of micromachining. Next, we went on to discuss the different ways in which the electron lens can be integrated into the FEA. These approaches are compared in **Table 2-1**.

The last section discussed prior work in IFE-FEA fabrication. In that group, devices fabricated by Itoh et. al. stand out for their reliable and effective focusing performance with a L/OP structure. While also working on a L/OP structure, we will attempt to improve on their work in several ways.

♦ Our process will not rely on vertical (non-conformal) oxide deposition, which is an "exotic" step, in that equipment for it is not widely available; all steps in our process will be accomplished with conventional equipment used in CMOS fabrication.

♦ We will attempt to lower operating voltages by making sharper tips and reducing apertures of the gate and focus electrodes.

♦ Itoh's work presents very little analysis of the electrical data from IFE-FEA. We will generalize the single-gate FN equation to IFE-FEA and use it to study its IV characteristics.

♦ Finally, we will aim to explore optical (beam collimation) data in greater depth.

Table 2-1. Pros and cons of different approaches to FED focusing.

	Advantages	Disadvantages
Proximity Focusing	• simple to fabricate the cathode • adequate focusing	♦ lower luminous efficiency ♦ lower brightness ♦ shorter lifetime
External Focusing Grid	• effective focusing • protects the cathode from stray ions ejected from the anode • easier and more reliable than microfabrication of IFE at the beginning stage • focus does not reduce emission current	♦ Laborious manufacture and assembly ⇒ higher cost than IFE
Global, In-Plane IFE	• probably the easiest IFE to fabricate • focus does not reduce emission current • No gate-focus leakage or ½CV^2 power dissipation	♦ inadequate focusing (except for 2x2 arrays) ♦ lower tip packing density ♦ asymmetry in the focusing electrode, leading to spot distortion
Global, Out-of-Plane IFE	• possibly better focusing than global, in-plane IFE	♦ inadequate focusing (except for 2x2 arrays) ♦ lower tip packing density ♦ usually harder to fabricate ♦ Greater chance of gate-focus leakage; more power dissipation; greater chance of breakdown.
Local, In-plane IFE	• easier to fabricate • focus does not reduce emission current • No gate-focus leakage or ½CV^2 power dissipation	♦ lower tip packing density ♦ asymmetry in the focusing electrode, leading to spot distortion
Local, Out-of-plane IFE	• the most effective and efficient focusing (hence, lower focusing voltage) • higher tip packing density	♦ probably, the hardest to fabricate ♦ focus reduces emission current ⇒ higher operating voltage ♦ gate-focus leakage, power dissipation, and greater chance of breakdown (due to failure of the gate-focus isolation)

3 Bowling Pin Model of Conical Field Emitters

3.1 FEA Modeling – Overview of Prior Work

A critical component of the effort to advance FED technology is development of models to predict FEA behavior. Modeling of FEAs is extremely useful because (i) it identifies the parameters that determine FEA performance and thus serves as a valuable design tool; (ii) given device parameters, modeling can predict device performance and operating conditions and expose potential failure modes; and (iii) modeling provides a physical insight into device operation and thus helps to interpret the data.

The models intended for FEA simulation have, broadly speaking, two objectives – computation of emitter current as a function of gate voltage and computation of electron trajectories. The latter has remained up till now entirely in the domain of numerical models.

Computation of the emitter current as a function of gate voltage begins with an equation for the emission current density as a function of the applied electric field. The simplest and most commonly used is the Fowler-Nordheim equation [60,61], which we already encountered in Chapter 1. After the usual simplifications and approximations [60], it reduces to:

$$J(E) = \frac{1.27273\times10^{-6} e^{9.86814/\sqrt{\varphi}}}{\varphi} E^2 \times \exp\left[-\frac{6.5265\times10^7\ \varphi^{3/2}}{E}\right] \equiv a_J(\varphi) E^2 \times \exp\left[-\frac{b_J(\varphi)}{E}\right]$$

$$a_J(\varphi) \equiv \frac{1.27273\times10^{-6} e^{9.86814/\sqrt{\varphi}}}{\varphi}; \qquad b_J(\varphi) \equiv 6.5265\times10^7\ \varphi^{3/2} \tag{3.1}$$

where E – electric field on the emitting surface [V/cm]; J – emission current density [A/cm^2]; φ – material work function [eV].

Theoretical objections have been raised against using the Fowler-Nordheim equation to describe emission from ultrasharp tips [62]. The argument is that when the tip radius of curvature is comparable to the width of the tunneling barrier, which is about 1-2 nm (c.f. **Figure 1-3**), it is no longer valid to treat the emitter surface as a plane, or more accurately, to replace each area element of the emitter surface with the area element of the local tangent plane. In practice, **Equation (3.1)** shall be the basis of calculations throughout this work since our model is concerned with describing the electrostatics rather than the quantum mechanics of device operation. Results of our electrostatic modeling can then be easily incorporated into a more sophisticated quantum mechanical treatment of field emission from ultrasharp tips. The sharpest tips we will end up dealing with will have ROC values of less than 3 nm. However, **Equation (3.1)** has been successfully used to describe tips as sharp as 1.7 nm ROC [63, 64].

Another procedure that has been criticized on theoretical grounds [65] but is nonetheless widely and successfully used in analyzing the data is based on the fact that

the plot of $\mathrm{Ln}(I/V^2)$ vs. 1/V, where I is the emission current and V is the gate voltage, is empirically found to be a straight line, i.e.

$$\ln\left(\frac{I}{V^2}\right) = a_{FN} + \frac{b_{FN}}{V} \tag{3.2}$$

The questionable step used in deriving the above equation is setting:

$$I(V) = \alpha J\left[E(V)\right]; \quad E(V) = \beta V \tag{3.3}$$

where α is the effective emission area and β is the field factor. An analytical model can provide a mathematical, rather than empirical, demonstration of the validity of **Equation (3.3)** and limitations thereof.

Mathematically, the total current should be computed by taking the integral of the current density over the emitter surface:

$$I = \int_S J\left[E(\vec{r})\right] dA \tag{3.4}$$

Now computation of the emission current becomes a problem of determining the electric field E everywhere on the tip, which can be done by numerical or analytical means. The majority of existing FEA models are numerical partly because the geometry of an FEA cell does not fit very well into any one coordinate system which makes it difficult to develop an accurate analytical model. Moreover, numerical models have the advantage of versatility. For example, a numerical electrostatic model of a conical emitter usually can be easily adapted to describe ridge emitters, while an analytical electrostatic model as a rule is limited to a narrow range of geometries.

On the other hand, when a quantitatively accurate analytical model *is* possible, it provides a lucid, quantitative picture of the effects of various device parameters on device performance. Obtaining the same insight numerically would require a number of simulations, which is more laborious and not as direct. Moreover, analytical model is simpler than numerical in several ways: (i) it is usually easier to implement and troubleshoot and is thus more convenient to use for other workers in the field (ii) computations for varying geometric parameters in a numerical model typically require generation of new meshes and thus a repetition of a part of the layout process, while in the analytical model the same task is accomplished by simply changing the values of the corresponding variables. (iii) analytical model should be easier to incorporate into circuit simulation software.

The most commonly used crude models of conical field emitters represent the device as a sphere positioned either between two parallel plates (the floating sphere model [65]) or inside a larger, concentric spherical shell (ball in a sphere [66]). The radius of the smaller sphere is set equal to the emission tip radius of curvature (ROC), R_ε. Such models yield simple analytical solutions and are useful for qualitative study of certain dependencies, such as electrical field on the surface versus the tip radius of curvature. For example, in the ball-in-a-sphere model, the electric field at the apex is given by:

$$E_A = \left(1 + \frac{R_\varepsilon}{R_d}\right)\frac{V}{R_\varepsilon} \tag{3.5}$$

where R_d is the sphere radius and E_A is the apex electric field.

However, the range of validity of such models is severely limited by the crudeness of approximations; for example, in the floating sphere model, the geometry of the gate aperture is completely unaccounted for, and in the ball-in-a-sphere model, the angular dependence of the field is lost.

Before the days of microfabrication field emitters were made of etched tungsten wire and activated by macroscopic gates/anodes. The shape of the gate was thus easily controllable, and it was practically possible to test a model that represented the emitter and the gate as surfaces of the same family, or had the emitter surrounded by the gate. For example, the emitter could be modeled as a cone with a sphere centered on its apex and the gate as a larger sphere, concentric with the first one [67]. Alternatively, the emitter and the anode could be modeled as two conical surfaces [68] or as two parabolloids [69]. In the latter case, illustrated in **Figure 3-1**, the field at the emitter tip (E_0) is given by:

$$E_0 = \left(\frac{2}{\ln\left(1 + 2d/R_\varepsilon\right)} \right) \frac{V_G}{R_\varepsilon} \qquad (3.6)$$

where d is the tip to gate distance measured between the apexes, and V is gate voltage. The reduction of the field along the tip in that model is:

$$E_h = \frac{E_0}{\sqrt{1 + 2h/R_\varepsilon}} \qquad (3.7)$$

where h is the vertical distance between a given point and the apex. In a recent work [66], Equation (3.7) is recast in terms of the conventional parameter, which is angle from the apex:

$$E(\theta) = \frac{E_0}{\sqrt{1 + \alpha^2(\theta)/\tan^2(\theta)}}; \qquad \alpha(\theta) = \begin{cases} 1 + \sqrt{1 + 2\tan^2(\theta)}, & \theta \geq 90^\circ \\ 1 - \sqrt{1 + 2\tan^2(\theta)} & \theta \leq 90^\circ; \end{cases} \qquad (3.8)$$

(The equation for $\alpha(\theta)$ in the original paper [66] apparently contains a misprint.)

An expression that is somewhat similar to Equation (3.6) is obtained by treating the emitter as an ellipsoid [70]:

$$E_0 \approx \left(\frac{2}{\ln\left(4c/R_\varepsilon\right) - 2} \right) \frac{V_G}{R_\varepsilon} \qquad (3.9)$$

(The equation in the original paper [70] apparently contains a misprint.) Here c is the distance between the gate and the cathode plane (i.e. oxide thickness). It is not clear how the expression accounts for the gate radius. The main drawback of the preceding two models is that they do not incorporate a good picture of the gate geometry. Moreover, it is unclear if the shape of the parabolic or elliptic tips can be varied with respect to the rate

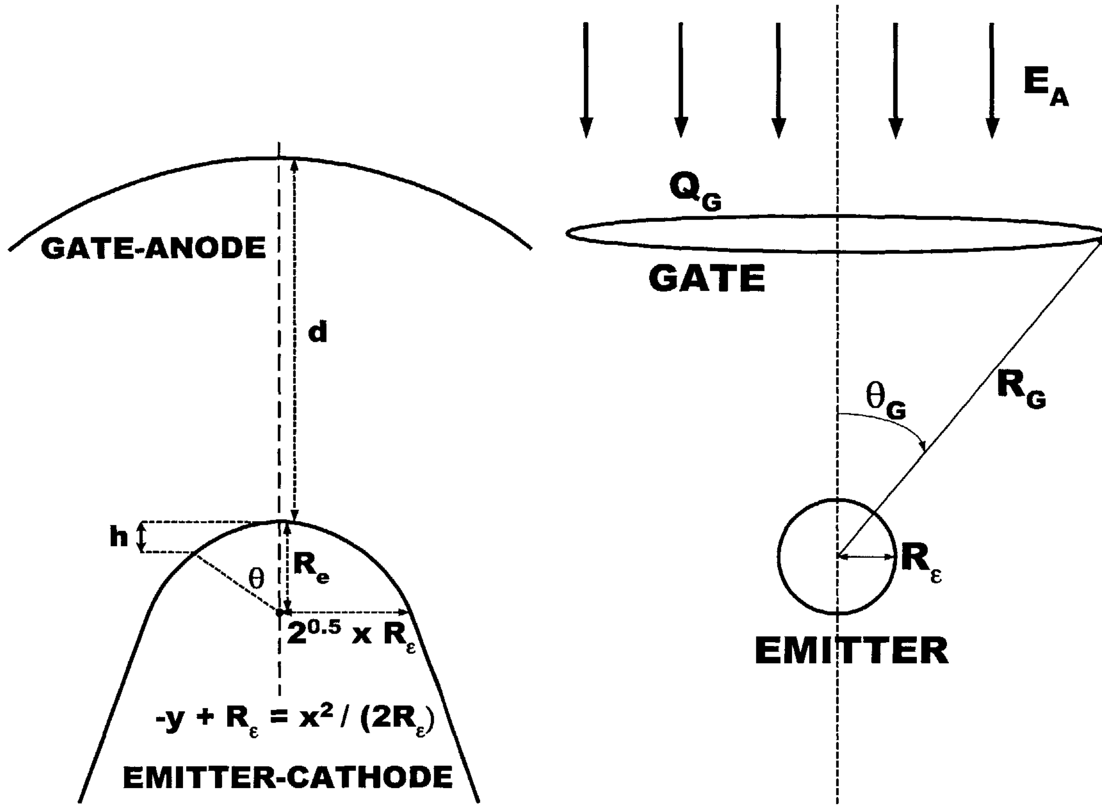

Figure 3-1. Variable definitions for the parabolloid (left) and Saturn models.

of change of radius of curvature with angle. For example, the equation of the paraboloid gives, in spherical coordinates, $r(\theta=0) = R_\varepsilon$, $r(\theta=90°) = R_\varepsilon\sqrt{2}$; however, the real tip will not necessarily conform to that curve. In the ellipsoid model, the expression for field variation with angle is not given.

The Saturn model [71] provides a better picture of the gate geometry by representing the gate as a ring of charge, as shown in **Figure 3-1**. Its main results will be summarized here for comparison with our model. The emitter is modeled as a ball centered on the axis of symmetry of the ring (but not necessarily concentric with the ring), and a uniform field is imposed perpendicular to the plane of the ring to account for the effect of the anode. With this setup the field on the ball is given by (in spherical coordinates (r, θ, ϕ)):

$$E(\theta) = 3E_A\cos(\theta) + \frac{Q_G}{R_G R_\varepsilon} \times \sum_{l=0}^{\infty}(2l+1)\left(\frac{R_\varepsilon}{R_G}\right)^l P_l(\cos(\theta_G))P_l(\cos(\theta)) \quad (3.10)$$

Here, E_A – the anode field; Q_G, R_G, θ_G – the charge on, the radial coordinate, and the angular coordinate of the gate ring; R_ε – the ball radius; $P_l(x)$ – Legendre polynomial

[71]. Based on the preceding equation, the Saturn model proposes that "a good parametric representation of E(θ) is given by:"

$$E(\theta)=\frac{E_0}{1+\lambda(1-\cos(\theta))} \qquad (3.11)$$

where E_0 is the apex field and λ is an unknown parameter. This yields an approximate expression for the total emission current from the tip:

$$I(V_G)\approx\frac{2\ \pi\ R_\varepsilon^2}{\lambda}F_2\left(\lambda,\frac{4v_0\sqrt{2m\phi^3}}{3\hbar E_A(V_G)}\right)J_{FN}(E_A(V_G))$$

$$F_n(\lambda,x)=\int_0^\lambda (1+y)^{-n}e^{-xy}dy \qquad (3.12)$$

In Equation **(3.12)**, the J_{FN} as defined by Equation 1 can be replaced by any other, more accurate, expression for the emission current density. Equation **(3.12)** suggests an expression for the slope of the FN plot, b_{FN}, as defined in Equation **(3.2)**

$$b_{FN}\approx\frac{4}{3}\sqrt{\frac{2m}{\hbar^2}}\frac{v_0}{\beta}\phi^{3/2} \qquad (3.13)$$

where β is the field factor, as defined in Equation **(3.3)**, and v_0=0.9369. The Saturn model estimate for the intercept of the FN plot, a_{FN}, is a very rough estimate and will not be included here. The authors of the Saturn model also obtained an approximate expression for the field factor, valid "for sharp tips roughly coplanar with the gate and neglecting the anode:"

$$\beta\approx\frac{\pi}{R_\varepsilon\ln(8R_G/t)} \qquad (3.14)$$

where t is an unknown parameter. Based on Equation **(3.14)**, they proposed an equation for the *gate to sphere capacitance* (i.e. the ratio of the charge on the sphere to gate voltage):

$$C_{CG}=\beta R_\varepsilon^2\approx\frac{\pi\ R_\varepsilon}{\ln(8R_G/t)} \qquad (3.15)$$

For comparison with the results to be derived below, it is useful to determine the closely related parameter of *gate capacitance*, which is the ratio of *gate charge* to gate voltage. The apex field on the ball can be written $E_0=Q_G/(R_G R_\varepsilon)$, as obtained by truncating the summation in Equation **(3.10)** at the l=0 term and neglecting the anode field. Then, after inserting a factor of $4\pi\varepsilon_0$ in the final result [71], we obtain,

$$C'_{CG}=\frac{Q_G}{V_G}=\frac{Q_G}{E_0/\beta}=\beta R_G R_\varepsilon\approx\frac{\pi R_G}{\ln\left(8\frac{R_G}{t}\right)} \qquad (3.16)$$

Practically speaking, the unknown parameters in Equations **(3.11)** – **(3.16)**, in particular λ and β, have to be found numerically; the Saturn model is thus a semi-numerical model.

In summary, all of the preceding models make only a rough approximation to the real device geometry and thus have limited accuracy. Our Bowling Pin Model (BPM) attempts to achieve greater accuracy by using a better representation of the real device geometry.

3.2 The Bowling Pin Model (BPM) for a Single Gate Emitter

3.2.1 The Bowling Pin Structure and Its Equipotentials

On the basis of the solution for the potential of a charged ring in the presence of a cone [67] and potential of a cone with a small sphere centered on its apex in the presence of a larger sphere [67], we obtain, by combination and trial-and-error, the potential of a charged ring in the presence of a "bowling pin," which is a cone with a small sphere centered on its apex, as shown in **Figure 3-2A** [72]:

$$V(r,\theta)=\frac{Q_G}{4\pi\varepsilon_0 R_G}\sum_{k=0}^{\infty}A_k P_{\nu_k}(\mu)P_{\nu_k}(\mu_G)\times\begin{cases}\left(\dfrac{r}{R_G}\right)^{\nu_k}\left(1-\left(\dfrac{R_\varepsilon}{r}\right)^{2\nu_k+1}\right), & r<R_G\\[2ex] \left(\dfrac{R_G}{r}\right)^{\nu_k+1}\left(1-\left(\dfrac{R_\varepsilon}{R_G}\right)^{2\nu_k+1}\right), & r>R_G\end{cases} \qquad \textbf{(3.17)}$$

$$A_k=\frac{1}{\left(\nu_k+\frac{1}{2}\right)\int_{\mu_0}^{1}P_{\nu_k}(\mu')^2\,d\mu'}\quad ;\ Q_G=C_G V_G$$

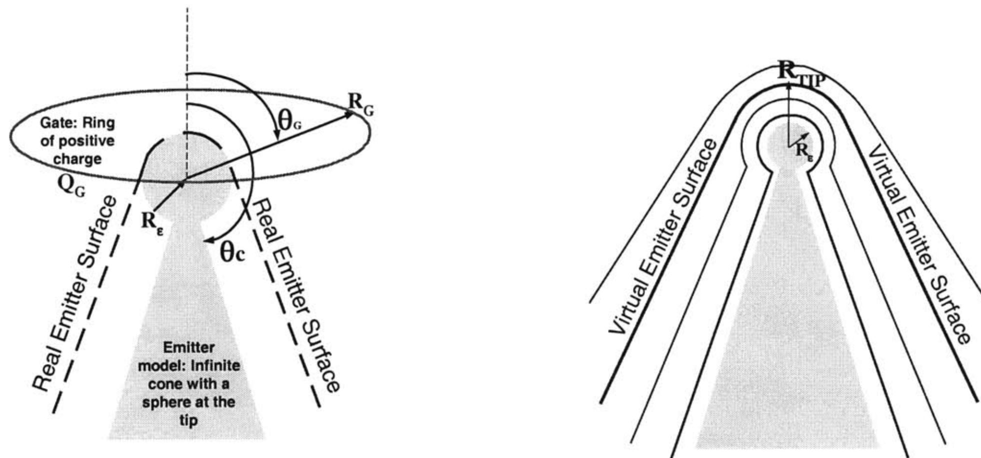

Figure 3-2. (A) Variable definitions for the Bowling Pin Model (B) Some equipotential surfaces of the Bowlign Pin closely resemble the real emitter surface.

where θ_C – cone angle ($\theta = \theta_C$ defines the conical surface); R_G, θ_G – spherical coordinates of the charged ring representing the gate; Q_G – charge on the gate ring; V_G- gate voltage (measured); C_G – gate capacitance, either calculated or treated as an adjustable parameter; $\mu = \cos(\theta)$; $\mu_G = \cos(\theta_G)$; $\mu_0 = \cos(\theta_C)$; $P_{\nu k}$ – Legendre functions of degrees ν_k, chosen to make the potential vanish on the surface of the cone [73]. It can be verified that this expression is a solution of the Laplace's equation (in spherical coordinates) and also satisfies our boundary conditions.

Legendre functions form a complete orthonormal basis [73], so for a given cone angle, there is an infinite sequence of positive real numbers, ν_k, such that Legendre functions of degrees ν_k vanish on the surface of the cone:

$$P_{\nu_k}(\mu_0) = 0 \quad \textbf{(3.18)}$$

Calculation of ν_k for a given μ_0 and subsequent calculation of the respective Legendre functions had been reported to be "highly complicated"[74] Analytical and semi-numerical methods for approximating ν_k have been developed [75] Our solution of this problem is based on recursion and on numerical root finding, implemented in Mathematica [76]. Mathematica can solve Equation **(3.18)** for ν_k, given two starting values. It finds the value of ν_k that is closest to the given starting values. We make sure the complete ν_k sequence is computed, without omissions, by observing that (i) $0 < \nu_0 < 1$ and (ii) $\nu_{k+1} - \nu_k \approx 1.2$. These are sufficient to compute the proper starting values for ν_{k+1} given ν_k.. Since calculations of Legendre functions of higher orders are time-consuming, we calculated and recorded values of P_{ν_K} , $0 \le k \le 200$, on a grid with 0.001 radian mesh and from then on used interpolation (accurate to a fraction of a percent for the most rapidly varying function.)

Comparison of the actual tip shape and the bowling pin in **Figure 3-2A** suggests that while the model may give a somewhat accurate value for the apex field, the calculated dependence of the field on the angle from the apex would be much weaker than in a real device. The field drop-off with angle on the real cone is largely due to increase in the local radius of curvature on the tip, which goes from R_ε at the apex to infinity on the wall of the cone.

The real cone surface can be more closely approximated with *equipotentials* of the bowling pin [77], as shown in

Figure 3-2**B**. For a given tip ROC, R_T, the shape of an equipotential surface can be adjusted by varying R_ε or ν_0. For example, **Figure 3-3** shows six tips which have the same ROC, 10 nm, but different values of eccentricity, generated by varying the ratio

$$\gamma = \frac{R_\varepsilon}{R_T} \quad \textbf{(3.19)}$$

between 0 and 1 in steps of 0.2. It can be seen that the most realistic-looking tip surface is obtained with γ=0.4, which is thus the most reasonable value for that parameter. The second parameter, ν_0, is equal to 0.2 in all cases, which corresponds to the cone angle θ_C=170°. While this specification of ν_0 is admittedly somewhat arbitrary, the error is not

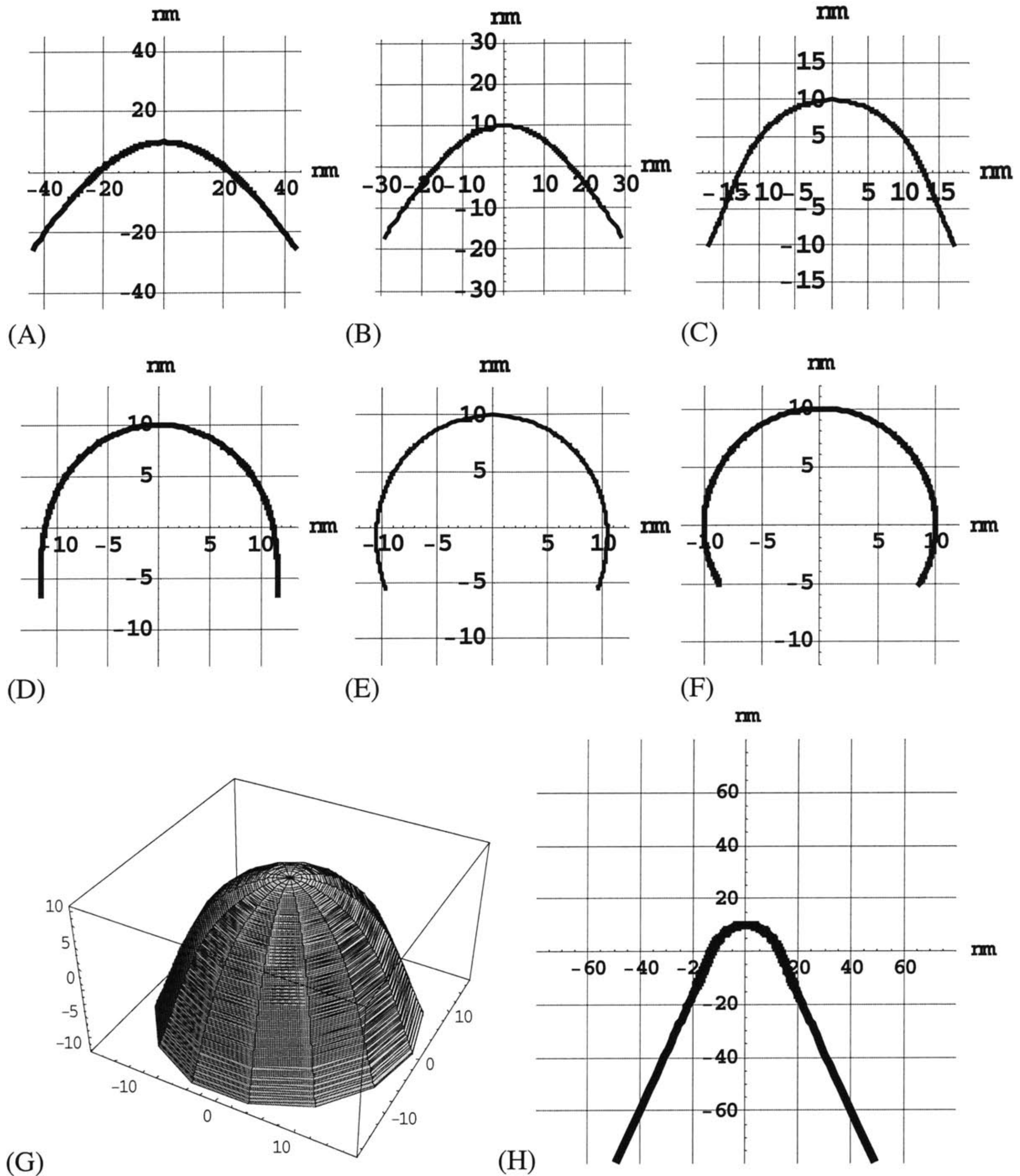

Figure 3-3. Bowling Pin equipotentials corresponding to different values of eccentricity, $\gamma = R_\varepsilon / R_T$ (A) $\gamma = 0.00001$ (B) $\gamma = 0.2$ (C) $\gamma = 0.4$ (D) $\gamma = 0.6$ (E) $\gamma = 0.8$ (F) $\gamma = 1$ (G) 3D picture (surface of revolution) for $\gamma = 0.4$. (H) $\gamma = 0.4$ tip corresponds to the cone angle of θ_C=155°.

appreciable since ν_0 changes fairly slowly with cone angle when cone angle is less than 170°. For example, when θ_C=150°, which is about the smallest cone angle seen in real devices, ν_0=0.35. However, if we are primarily interested in the examining effect of the gate radius, it would be better to take θ_C equal to the cone angle of the actual device which would in general make ν_0>0.2. However, in silicon structures, the actual device is

often not a perfect cone, but a cone on a cylinder, as in this work, or a hyperboloid of revolution. This makes more accurate modeling even more difficult. For the rest of this chapter we will use ν_0=0.2, but the summary will discuss the range of possible ν_0 values.

Note also that the equipotential is not at zero voltage. The BPM in general looses a degree of freedom because the cone is grounded by construction, whereas in the real FEA the cone may be biased below zero. In structures with etched emitters and macroscopic anodes this did not matter because the anode provided a Dirichlet boundary everywhere in space, so that only the voltage difference between gate and cathode was relevant. In FEA, the problem in general involves *three* surfaces: cathode, gate, and infinity (at 0). This has to be handled with care for the purposes of trajectory calculations; however, to compute emission current it is sufficient to simply modify the expression for gate voltage, so that the gate-cathode voltage difference is the same in the model as in the real device.

$$\begin{aligned} V_G^{meas} - V_C^{meas} &= V_G^{meas} = V_G^{model} - V_C^{model} \\ V_C^{model} &= \delta\, V_G^{model} \\ V_G^{model} &= \frac{V_G^{meas}}{1-\delta} \end{aligned} \quad (3.20)$$

To avoid complicating notation, we leave out this factor until the very end of the following derivation.

3.2.2 IV Equation for a Conical Field Emitter

Derivatives of Equation (3.17) provide us with the radial and angular electric fields throughout all space, including the equipotential surface.

$$E_r(r < R_G, \theta) = \frac{C_G V_G}{4\pi\varepsilon_0 R_G r} \sum_{k=0}^{\infty} A_k P_{\nu_k}(\mu_G) P_{\nu_k}(\mu) \left(\frac{r}{R_G}\right)^{\nu_k} \left(\nu_k + (\nu_k + 1)\left(\frac{R_\varepsilon}{r}\right)^{2\nu_k+1}\right) \quad (3.21)$$

$$E_\theta(r < R_G, \theta) = \frac{C_G V_G}{4\pi\varepsilon_0 R_G r} \sum_{k=0}^{\infty} A_k P_{\nu_k}(\mu_G) \nu_k \frac{\mu P_{\nu_k - 1}(\theta) - P_{\nu_k}(\mu)}{\sqrt{1-\mu^2}} \left(\frac{r}{R_G}\right)^{\nu_k} \left(1 - \left(\frac{R_\varepsilon}{r}\right)^{2\nu_k+1}\right) \quad (3.22)$$

In the region $r \ll R_G$, the field in Equation (3.21) is closely approximated by the $k = 0$ term. Thus, the field at the apex of the equipotential surface representing the tip is:

$$E_A \equiv E(r = R_T, \theta = 0) \approx \frac{C_G V_G}{4\pi\varepsilon_0 R_G R_T} A_0 P_{0.2}(\mu_G) \left(\frac{R_T}{R_G}\right)^{0.2} 0.2\left(1 + 6\gamma^{1.4}\right) \quad (3.23)$$

We postpone the derivation of gate capacitance until the following section so as not to impede the flow of the main presentation. To simplify notation for now, we define dimensionless normalized capacitance as:

$$C_G' \equiv \frac{C_G}{4\pi\varepsilon_0 R_G} \quad \textbf{(3.24)}$$

Further, we confine our derivation to the case of the gate coplanar with the tip, since this is the predominant FEA configuration. The constant term in Equation (3.23) becomes

$$A_0 \times P_{0.2}(\mu_G = 0) \times 0.2 = 1.10 \times 0.84 \times 0.2 = 0.18 \quad \textbf{(3.25)}$$

So that the expression for the apex field in Equation (3.23) reduces to:

$$E_A \equiv E(r = R_T, \theta = 0) \approx 0.18\, C_G' \frac{1}{R_T}\left(\frac{R_T}{R_G}\right)^{0.2} \left(1 + 6\gamma^{1.4}\right) V_G \quad \textbf{(3.26)}$$

Although the equipotential surface that describes the tip cannot be specified analytically, there is a way to simplify the area integral in Equation **(3.4)** and show that the total current is proportional to the apex emission density and thus determined by the apex electric field.

$$\begin{aligned} I = \int_S J\left[E(\vec{r})\right] dA = \int_{\varphi=0}^{2\pi} \int_{\theta=0}^{17\pi/18} J\left[E(r(\theta),\theta)\right] r(\theta) \sin(\theta)\, d\varphi \; r(\theta)\, d\theta = \\ = 2\pi \int_{\mu_c}^{1} J\left[E(\mu)\right] r(\mu)^2\, d\mu = 2\pi R_{TIP}^2 \alpha' J_A \end{aligned} \quad \textbf{(3.27)}$$

where the second equality expresses the mean value theorem with J_A being the emission density at the apex.

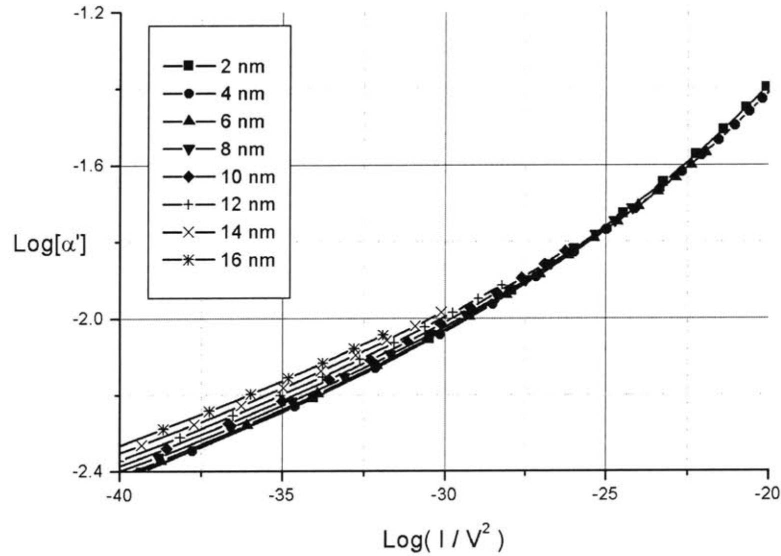

Figure 3-4. Plot of the voltage dependent component of the area factor shows that for all practical purposes it is constant in the range of interest.

Of course, the mean value α' would in general depend on the curve J[μ] and thus on gate voltage. However, empirical evidence for the correctness of Equation (3.3) suggests that this dependence may be weak (compared to the exponential dependence) in the range of interest. This is confirmed by **Figure 3-4** which shows a plot of *Log*(α) *vs. Log*(I/V^2) for currents spanning the typical operating range between 10 pA and 1 μA, tip radii ranging from 1 nm to 13 nm; $\gamma = 0.4$; and C = 1. It can be seen that the range of *Log*(I/V^2), which is the ordinate in the FN plot, is far greater than the maximum change in *Log*(α), which is a component of the intercept in the linear FN plot. The small systematic increase of *Log*(α) with *Log*(I/V^2) has the effect of reducing the absolute value of the slope of the FN plot from what it otherwise would have been, without affecting the linearity of the plot. It is shown in the Appendix that this introduces an error of 2-3%.

We can now put it all together to obtain a closed-form IV equation for a conical field emitter. Using Equation (3.1) and (3.26), we can write the apex emission density as

$$J_A \approx a_J(\phi)\left[0.03\,C_G'^{2}\,\frac{1}{R_T^2}\left(\frac{R_T}{R_G}\right)^{0.4}\left(1+6\gamma^{1.4}\right)^2\right]V_G^2\times Exp\left[-\frac{b_J(\phi)\left(5.56\,R_G^{0.2}R_T^{0.8}\right)}{C_G'\left(1+6\gamma^{1.4}\right)}\frac{1}{V_G}\right] \qquad \textbf{(3.28)}$$

Now we further confine ourselves to silicon tips, with the work function of 4.04 eV so that,

$$\begin{aligned} a_J\left(\phi=4.04eV\right) &= 4.27\times10^{-5} \\ b_J\left(\phi=4.04eV\right) &= 5.30\times10^{8} \end{aligned} \qquad \textbf{(3.29)}$$

Finally, we reintroduce the factor (1-δ) that accounts for non-zero voltage on the equipotential (Equation (3.20)) and write down the full IV equation (note that the factor of R_T^2 in the intercept cancels out):

$$I\left[V_G\right]\approx 8\times10^{-6}\,\alpha' C_G'^{2}\left(\frac{R_T}{R_G}\right)^{0.4}\left(\frac{1+6\gamma^{1.4}}{1-\delta}\right)^2 V_G^2\times Exp\left[-\frac{295\,R_G^{0.2}R_T^{0.8}}{C_G'\left(1+6\gamma^{1.4}\right)}\frac{1-\delta}{V_G}\right] \qquad \textbf{(3.30)}$$

where gate and tip radii are given in *nanometers* and the current is in Amperes. The primary objective of this analysis is to derive a relationship between Fowler-Nordheim coefficients, a_{FN} and b_{FN}, and geometric parameters of the device. The effect of the tip geometry is clear by now; however, the full effect of the gate radius is not obvious until we obtain an expression for the gate capacitance in terms of gate radius. This is done in the next section. We shall see that normalized gate capacitance, C_G',is approximately independent of gate radius.

3.2.3 Calculation of Gate Capacitance

It remains to relate the model parameter, Q_G, which is the gate charge in (3.17), to the measured parameter of gate voltage. Since the cone is grounded, the model parameter

Q_G (gate charge) can be written as a product of gate voltage, which is a measured parameter, and gate-to-cone capacitance. The Saturn model [71] proposes to determine capacitance by specifying the voltage at some point near the gate to be equal to the gate voltage. This generates an approximately toroidal surface centered on the charged ring and held at gate potential. However, the capacitance obtained in this way is quite sensitive to the choice of that point, which is not unique. This poses a problem since the emission current depends strongly on the value of capacitance. Our attempts to specify this point based on the thickness of the gate electrode (i.e. by making the inner part of the toroidal surface coincide with the contour of the gate opening) did not give meaningful results. Hence, we adopted a different approach. On the basis of the expression for the ring-to-cone capacitance [70], we can obtain the capacitance of a ring in the presence of a bowling pin:

$$C_{R-BP} = \frac{4\pi\varepsilon_0 R_G}{\sum_{n=0}^{\infty}\left[1-\left(\frac{R_\varepsilon}{R_G}\right)^{2n+1}\right]\left(P_n(\cos\theta_G)\left[P_n(\cos\theta_C)Q_n(\cos\theta_G)-P_n(\cos\theta_G)Q_n(\cos\theta_C)\right]\right.} \quad \textbf{(3.31)}$$

where $P_n(x)$ and $Q_n(x)$ are Legendre polynomials of the first and second kinds. If $\theta_G=90°$ (i.e. the tip is coplanar with the gate), only even terms remain.

The ball on the tip of the cone can be neglected for capacitance calculations when $R_{BALL} \ll R_{RING}$, which is usually true. Then we are back to the expression for the ring-to-cone capacitance:

$$C_{R-C} = \frac{4\pi\varepsilon_0 R_G}{\sum_{n=0}^{\infty} P_n(\mu_G)\left[P_n(\mu_C)Q_n(\mu_G)-P_n(\mu_G)Q_n(\mu_C)\right]} \quad \textbf{(3.32)}$$

Incidentally, it has been stated in the literature that C_{R-C} gives "the capacitance between an infinitely thin ring and two cones joined head to head." [78] In our opinion this is incorrect, and **Figure 3-5**, which is not symmetric about $\theta_G=90°$, demonstrates this. In fact, the expression for potential from which C_G was derived [70] only vanishes on the cone $\theta=\theta_C$. It does not vanish on the cone $\theta = \pi-\theta_C$ because Legendre polynomials of the first and second kinds, $P_n(x)$ and $Q_n(x)$ exhibit opposite parity (i.e. $Q_{2n}(x)$ are odd.) The expression does have a logarithmic singularity on the axis $\theta=0$. Thus it is not equivalent to Equation **(3.17)**.

Figure 3-5 also provides additional insight is the effect of the vertical position of the tip relative to the gate. The Saturn model suggests that "the [tip] field is not maximized for the tip of the emitter lining up with the gate plane. The emitter should be below (or above) the gate plane" to maximize the tip field [71]. Neglecting the effect of the anode field, the Saturn model does not distinguish whether the tip is above or below the gate. Other models mentioned above do not treat the gate as a horizontal circular opening and thus cannot incorporate the effect of the vertical position of the tip. However, it has been observed experimentally [60, 79] that the field at the tip effectively increases as the tip goes from below the gate, to level with the gate, to above the gate. We believe that this is due to the increasing interaction between the gate and the cone. This is reflected in a sharp increase in cone-to-gate capacitance (**Figure 3-5**) as the tip

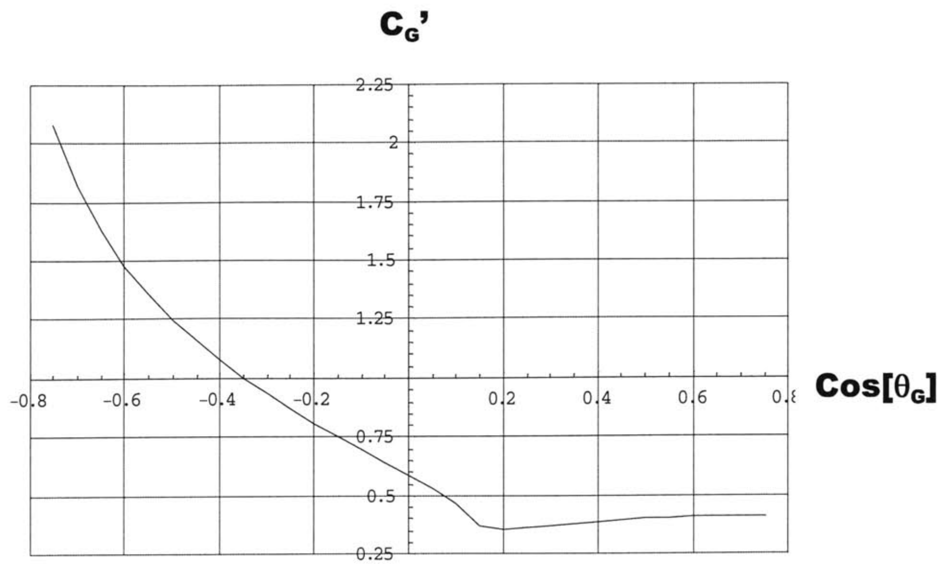

Figure 3-5. Approximate value of the ring-to-cone capacitance as a function of cosine of the angular position of the ring (θ_G).

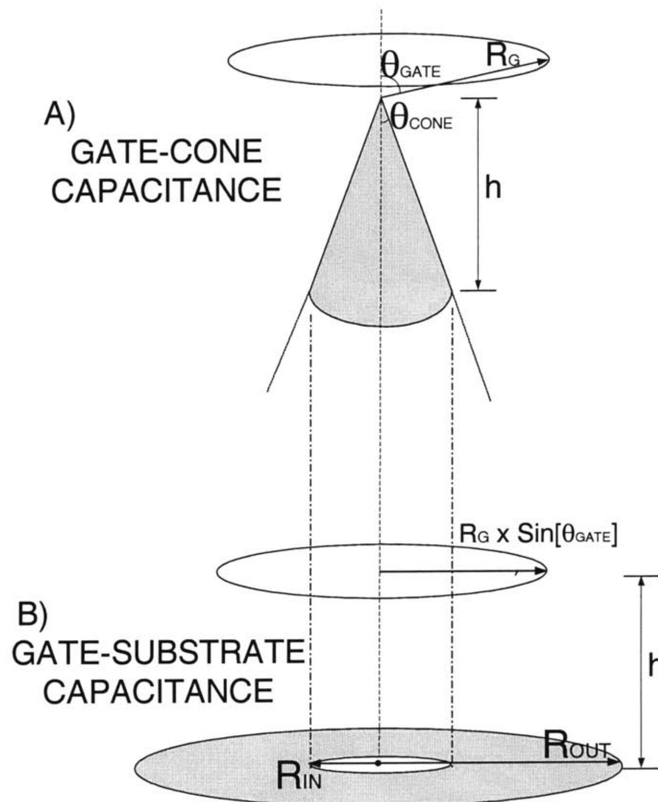

Figure 3-6. Diagram of capacitance calculation. Gate-to-cathode capacitance is equal to the sum of the gate-to-cone capacitance (a) and the gate-to-plane capacitance (b).

moves from below the gate to above the gate. This effect outweighs the increase in separation between the gate and the tip (tip-to-gate distance is minimum when the two are coplanar).

Equation (3.32) gives the capacitance for a cone of infinite vertical extent. Assuming the real cone has height *h*, as in **Figure 3-6A**, we can write:

$$C_{R-C(h)}(h) = \frac{Q(h)}{Q_{tot}} C_{R-C} = \frac{\int_0^{S(h)} \varepsilon_0 E_\theta(S)\,dS}{Q} \times C_{R-C} \tag{3.33}$$

Writing the (radially symmetric) surface charge density on the cone as σ(r) and invoking Gauss's Law leads to:

$$Q(h) = 2\pi\sqrt{1-\mu_c^2}\int_0^{h/|\mu_C|} r\sigma(r)\,dr = -2\pi\,\varepsilon_0\sqrt{1-\mu_c^2}\int_0^{h/|\mu_C|} r\,E_\theta(r)\,dr \tag{3.34}$$

With the angular field $E_\theta[r]$ given by **Equation (3.22)** and assuming $R_{RING} < h / |\mu_G|$ (which is true for most real devices), this gives:

$$Q(h) = -\frac{Q_G}{2}\sum_{k=0}^{\infty} A_k P_{\nu_k}(\mu_G) P_{\nu_k-1}(\mu_c) \times \left[\left(\frac{2\nu_k+1}{(\nu_k+1)} - \left(\frac{R_G}{h/\mu_C}\right)^{\nu_k}\right)\right] \tag{3.35}$$

Thus, the tip to ring capacitance becomes:

$$C_{R-tip}(h) = \frac{C_{R-C}}{2}\sum_{k=0}^{\infty} A_k P_{\nu_k}(\mu_G) P_{\nu_k-1}(\mu_c) \times \left[\left(\frac{2\nu_k+1}{(\nu_k+1)} - \left(\frac{R_G}{h/|\mu_C|}\right)^{\nu_k}\right)\right] \tag{3.36}$$

For a 1-micron tall cone, the difference between **Equation (3.36)** and **Equation (3.32)** is only a few percent [72]. It is also possible to use the original expansion for the potential (Equation (3.17)) to compute the capacitance. This approach is illustrated in the following section that deals with extending the BPM to double gate field emitters.

Next, we need to incorporate the interaction between the gate and the cathode plane. The cathode plane may be modeled as a cylindrical ring with the outer radius R_{max} (the specification of which would have to be somewhat arbitrary) and the radius of the opening R_{base} (set equal the radius of the base of the cone) Figure 3-6B. The cathode plane to ring capacitance is then equal to the difference $C_{R\text{-}Disk}(R_{max})$ - $C_{R\text{-}Disk}(R_{base})$. The ring to disk capacitance can be written exactly in oblate spheroidal coordinates [70,80], note that our formula, obtained on the basis of Reference 80, differs slightly from the one in the former reference]

$$C_{Ring-Disk}(a) = \frac{4\pi\,\varepsilon_0\, a}{i\sum_{n=0}^{\infty}(4n+1)(1-A_{2n})P_{2n}^2(\xi_0)P_{2n}(i\zeta_0)Q_{2n}(i\zeta_0)} \tag{3.37}$$

where, $A_{2n} = \frac{2i}{\pi}\times\frac{Q_{2n}(i\zeta_0)}{P_{2n}(i\zeta_0)}$, *a – disk radius;* ($\zeta_0$, ξ_0) – ring coordinates

Legendre polynomials with imaginary argument are given by [80]:

$$\begin{aligned} P_n(i\zeta) &= (-1)^{n/2}\sum_{s=0}^{n/2}\frac{(2n-2s)!}{2^n s!(n-s)!(n-2s)!}\zeta^{n-2s}, \quad for \quad even \quad n \\ Q_n(i\zeta) &= (-i)^{n+1}2^n\sum_{s=0}^{\infty}\frac{(-1)^s(n+2s)!(n+s)!}{s!\,(2n+2s+1)!}\zeta^{-n-2s-1} \end{aligned} \tag{3.38}$$

The transformation equations between cylindrical coordinates (r, z, φ) and oblate spheroidal coordinates (ζ, ξ, φ) are (assuming rotational symmetry):
$z = a\zeta\xi, \quad r = a\left[(1+\zeta^2)(1-\xi^2)\right]^{1/2}$. Inverting these equations gives:

$$\begin{aligned} \zeta &= \sqrt{\frac{(z^2+r^2-a^2)+\left((z^2+r^2-a^2)^2+4a^2z^2\right)^{1/2}}{2a^2}}; \\ \xi &= \sqrt{\frac{-(z^2+r^2-a^2)+\left((z^2+r^2-a^2)^2+4a^2z^2\right)^{1/2}}{2a^2}} \end{aligned} \tag{3.39}$$

[Note that instead of using curvilinear coordinates, we could have solved this problem by treating the plane as a cone with μ_C=0, and following the procedure used for calculating the ring to cone capacitance.]

Putting it all together, the ratio of the gate charge to gate voltage becomes:

$$\frac{1}{4\pi\,\varepsilon_0\,R_G}\frac{Q_G}{V_G} = \frac{C_G}{4\pi\,\varepsilon_0\,R_G} = C_G' = \frac{C_{R-tip}(h)+C_{R-disk}(R_{\max})-C_{R-disk}(R_{base})}{4\pi\,\varepsilon_0\,R_G} \tag{3.40}$$

For most real device configurations this quantity is *independent* of gate radius. For fabrication reasons most silicon tip devices have either h<R_G<2h, which is the most common configuration, or h>>R_G, as in the device presented in this work. In the latter case, the total capacitance is dominated by the ring-to-cone interaction, as given in **Equation (3.32)**, which makes C_G' independent of R_G. When h=R_G, $C_{R-tip}(h)/(4\pi\,\varepsilon_0\,R_G)$ is still independent of R_G (c.f. **Equation (3.36)**). To see that the same holds for the $C_{R\text{-}disk}$ terms, consider the plane as a cone with θ_C = 90°. Then $C_{R\text{-}disk}$ can be expressed in terms of **Equation (3.32)** as

$$C_{R-C} = \frac{4\pi\varepsilon_0 \left(R_G^2 + h^2\right)^{1/2}}{\sum_{n=0}^{\infty} P_n(\mu_G)\left[P_n(\mu_C = 0)Q_n(\mu_G) - P_n(\mu_G)Q_n(\mu_C = 0)\right]} \qquad \textbf{(3.41)}$$

which is approximately proportional to R_G

Though analytical expressions for capacitances did give quantitatively accurate results in modeling certain device geometries [72], our own device structure is such that it will be necessary to treat C_G' as an adjustable parameter.

3.2.4 Dependence of Fower-Nordheim Coefficients on Device Geometry: Summary and Comparison with Other Models

With the gate capacitance, C', being approximately constant, and the eccentricity factor, γ, also fixed in the range 0.4-0.6 for a typical tip, the FN coefficients become functions of the gate radius and the tip radius of curvature, as summarized in the following equations:

$$a_{FN} = -8.5 + Log\left[\alpha' C_G'^2\right] + 2\nu_0 Log\left[\frac{R_T}{R_G}\right] + 2Log\left[\frac{\nu_0 + (1+\nu_0)\gamma^{1+2\nu_0}}{1-\delta}\right] \qquad \textbf{(3.42)}$$

$$b_{FN} = -59\frac{R_G^{\nu_0} R_T^{1-\nu_0}}{C_G'\left(\nu_0 + (1+\nu_0)\gamma^{1+2\nu_0}\right)}(1-\delta) \qquad \textbf{(3.43)}$$

R_T is tip radius of curvature (ROC);

R_G is the gate radius in *nm*, measured as the distance from the tip to the gate. The equations above have been confined to the case of the gate co-planar with the tip, since it is the most common. In this case, R_G is equal to half the gate diameter.

$0.2 < \nu_0 < 0.4$ ($\nu_0 = 0.2$ will be used in fitting data) **(3.44)**

$0.4 < \gamma < 0.6$ **(3.45)**

$$\delta \approx 0.92 C_G' \left(\frac{R_T}{R_G}\right)^{\nu_0} \left(1 - \gamma^{1+2\nu_0}\right) \qquad \textbf{(3.46)}$$

$$Log(\alpha') \approx -2 \qquad \textbf{(3.47)}$$

In summary, the Bowling Pin Model developed in this chapter for the case of a single gate emitter enabled a proof of linearity of the FN IV equation (Eq. (3.2)) and then provided closed-form solutions for the FN slope and intercept as functions of device parameters, particularly gate radius and tip radius of curvature (Eq. (3.42) - (3.47)).

Other models reviewed in the beginning of this chapter also provide equations for b_{FN} as a function of R_T and R_G; Table 3-1 compares them to BPM results. The specific parameter compared in the table is the "field factor:"

$$\beta \equiv \frac{V_{GATE}}{E_{APEX}} \qquad (3.48)$$

For the BPM, the field factor is given by Equation (3.26). It is seen that the BPM is in agreement with the results from finite element (FEM) simulation, and is more accurate than other analytical models. In addition, the BPM

♦ captures the true geometry of a circular gate around a conical field emitter and provides describes the dependence of the field factor on gate radius

♦ provides a fairly accurate approximation for the FN intercept, a_{FN}.

♦ explains the effect of the vertical position of the gate with respect to the tip through gate-to-cone capacitance

♦ demonstrates the importance of tip eccentricity through the γ parameter.

Table 3-1. Dependence of the field factor, β, on the tip ROC and on the gate radius.

	Ball in a Sphere Model[66]	**Parabo-lloid Model**[69]	**Ellipsoid Model**[70]	**Saturn Model**[71]	**Matlab FEM**[81]	**Bowling Pin Model (BPM)**
$\beta \equiv \frac{V_G}{E_A}$	$\left(1+\frac{R_T}{R_G}\right)\frac{1}{R_T}$	$\frac{2R_T^{-1}}{Log\left(1+2\frac{d}{R_T}\right)}$ d – distance between apexes the equivalent of R_G	$\frac{2R_T^{-1}}{\ln\left(4\frac{c}{R_T}\right)-2}$ c—is the gate-to-cathode distance, i.e. oxide thickness which is comparable to R_G	$\frac{\pi}{R_T Log\left(8\frac{R_G}{t}\right)}$ t is an unknown parameter	$R_T^{-0.7}$	$0.18\,C_G{}'\,\frac{1}{R_T}$ $\times\left(\frac{R_T}{R_G}\right)^{\nu_0}$ $\times\left(1+6\gamma^{1+2\nu_0}\right)$
Dependence on R_T as $\frac{R_T}{R_G}\to 0$	R_T^{-1}	R_T^{-x}, $x<1$ or $x\approx 1$	R_T^{-x}, $x<1$ or $x\approx 1$	R_T^{-1}	$R_T^{-0.7}$	$R_T^{-(1-\nu_0)}$ $0.6<1-\nu_0<0.8$

Before we conclude, let's examine the last point in more detail. In numerical modeling, the tip is usually assumed to be a section of a sphere smoothly joined to the top of a cut-off cone. Although this configuration is not reproducible with BPM, there is also no reason to assume that actual tips have perfectly spherical tops. While micrograph resolution is insufficient to settle this point conclusively, in the opinion of this author, a

typical tip is a section of an ellipsoid. This is represented in BPM. There is also a distribution of eccentricities among different tips, although extreme values are unlikely.

Eccentricity as represented in BPM matters for several reasons. One is that tips with higher eccentricity have a higher apex field for the same tip ROC (**Equation (3.26)**). Moreover, eccentricity determines the rate of drop-off of emission density with angle from the apex, which has effect on the total current and on the angular spread of the emission beam. Thus in a tip with eccentricity much greater than 1 (low value of γ), the radius of curvature increases rapidly with angle, so that the field and hence the emission density falls, and the beam has a smaller angular spread.

In order to compare the predictions of various models for angular dependence of field at the tip, we used the BPM to generate the tip profile similar to the one produced by the parabolloid model of **Equations (3.6) and (3.7)**. Since the parabolic model describes the tip by the equation $-y+R_\varepsilon = x^2/2R_\varepsilon$, the tip "half-width" is fixed at $x(y=0)=R_\varepsilon\sqrt{2}=r(\theta=90^\circ)$. A tip of the same half width can be generated by BPM when γ = 0.338. Although the tip shapes are very similar (**Figure 3-7A**), the BPM predicts a slower drop-off in the field over the range of interest **(Figure 3-7B)** and thus leads to greater emission current density (**Figure 3-8**) and higher total current. It was observed that the Saturn model with the adjustable parameter λ set to 0.76 gives a field profile that is very close to the parabolic model [71]. We also found that with λ = 0.52 the Saturn model closely approximated the BPM. [**Figure 3-7B**, **Figure 3-8**].

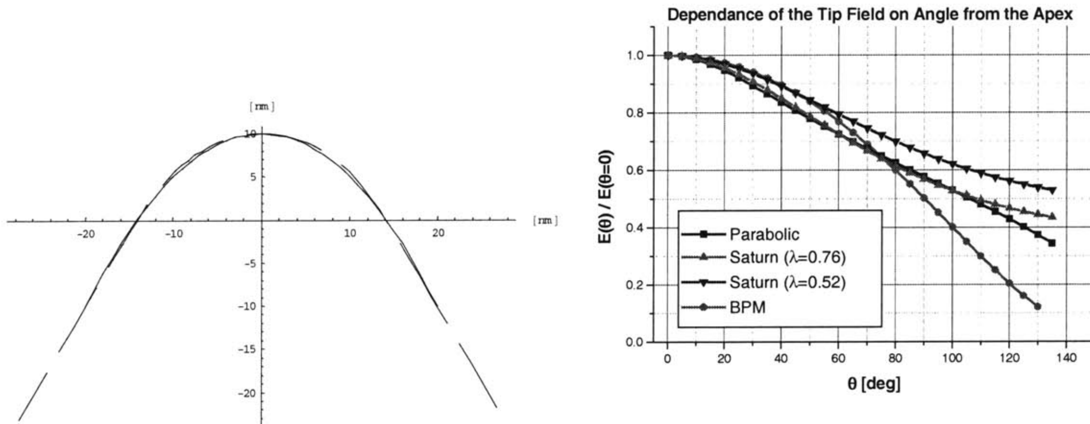

Figure 3-7. (A) Comparison of tip shapes from the parabolic model (solid line) and the BPM (dashed line) with γ = 0.338. (B) Variation of tip field with angle from the apex as predicted by different models.

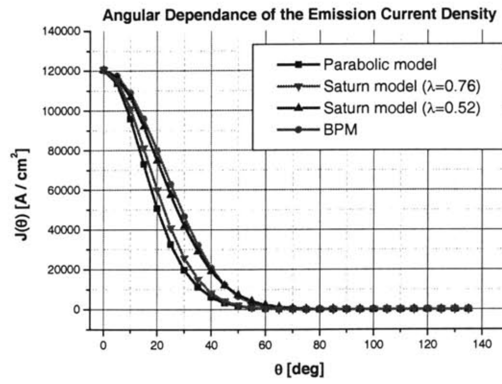

Figure 3-8. Variation of emission current density with angle from the apex as predicted by different models [based on Figure 3-7B with E_A=4 V/nm]

3.3 Extension of the Bowling Pin Model to Field Emitters with Focusing Electrode

3.3.1 Potential of Two Charged Rings in the Presence of a Grounded Cone

Field emitters with integrated focusing electrode (IFE-FEA's) have been a subject of comprehensive numerical modeling [82, 83, 84, 85, 86, 87, 88, 89, 90]; however, to the best of our knowledge, this work is the first analytical model for these devices. In fact, with the exception of the Saturn model [71], gross approximations to device geometry present in the earlier analytical models of field emitters make it impossible to extend them to IFE-FEAs. At the same time, an effective analytical model would provide a quick and clear insight into the operation of IFE-FEAs and the effects of various geometric parameters on device performance. This is the goal of extending BPM for double-gate emitters [91]. Generalization of the BPM model to include the focus electrode is based on superposition. If the focus electrode is represented by another charged ring, as indicated in , we can write (cf. Equation (3.17)):

$$V(r,\theta)=\begin{cases}\dfrac{Q_G}{4\pi\varepsilon_0 R_G}\sum\limits_{j=0}^{\infty}A_j P_{\nu_j}(\mu_G)P_{\nu_j}(\mu)\left(\left(\dfrac{r}{R_G}\right)^{c_j}-\dfrac{R_\varepsilon^{2\nu_j+1}}{R_G^{\nu_j}r^{\nu_j+1}}\right)+\\ \dfrac{Q_F}{4\pi\varepsilon_0 R_F}\sum\limits_{k=0}^{\infty}A_k P_{\nu_k}(\mu_F)P_{\nu_k}(\mu)\left(\left(\dfrac{r}{R_F}\right)^{c_k}-\dfrac{R_\varepsilon^{2\nu_k+1}}{R_F^{\nu_k}r^{\nu_k+1}}\right)\end{cases}$$

$$A_k=\frac{1}{\left(\nu_k+\frac{1}{2}\right)\int_{\mu_0}^{1}P_{\nu_k}(\mu')^2\,d\mu'};\quad c_j=\begin{cases}\nu_j & for\ r<R_G\\ -(\nu_j+1) & for\ r>R_G\end{cases};\quad c_k=\begin{cases}\nu_k & for\ r<R_F\\ -(\nu_k+1) & for\ r>R_F\end{cases}$$

(3.49)

where θ_C – cone angle ($\theta=\theta_C$ defines the conical surface); R_G, θ_G – spherical coordinates of the charged ring representing the gate; R_F, θ_F – spherical coordinates of the charged ring representing the focus; Q_G – charge on the gate ring; Q_F – charge on the focus ring; $\mu=\cos(\theta)$; $\mu_G=\cos(\theta_G)$; $\mu_0=\cos(\theta_C)$; $P_{\nu k}$ – Legendre functions of degrees ν_k, chosen to make the potential vanish on the surface of the cone.

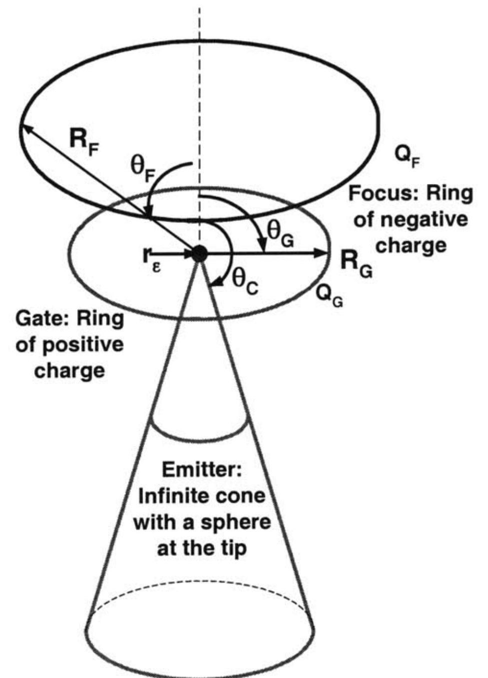

Figure 3-9. Variable definitions in the Bowling Pin Model for a Double Gate field emitter

3.3.2 Derivation of Capacitance Coefficients

Again we can write the electrode charges (Q_G and Q_F) as superpositions of the voltages [80]:

$$\frac{Q_G}{4\pi\varepsilon_0 R_G} = C_{11}V_{GATE} + C_{21}V_{FOCUS}$$
$$\frac{Q_F}{4\pi\varepsilon_0 R_F} = C_{12}V_{GATE} + C_{22}V_{FOCUS} \tag{3.50}$$
$$C_{12} = \left(R_G/R_F\right)C_{21} < 0; \quad C_{11} > 0; \quad C_{22} > 0$$

where V_{GATE} and V_{FOCUS} are voltages on the gate and focus electrodes respectively and C_{ij} are capacitance coefficients which incorporate the radial factors. To compute C_{ij}, we write down expressions for the potentials on the gate and focus rings:

$$\begin{pmatrix} V_G \\ V_F \end{pmatrix} = \begin{pmatrix} M_{11} & M_{12} \\ M_{21} & M_{22} \end{pmatrix}\begin{pmatrix} V_G \\ V_F \end{pmatrix}$$
$$M_{11} = C_{11}\sum_{j=0}^{\infty} A_j\left[P_{\nu_j}(\mu_G)\right]^2 + C_{12}\sum_{j=0}^{\infty} A_j\omega^{\nu_j}P_{\nu_j}(\mu_F)P_{\nu_j}(\mu_G);$$
$$M_{12} = C_{21}\sum_{j=0}^{\infty} A_j\left[P_{\nu_j}(\mu_G)\right]^2 + C_{22}\sum_{j=0}^{\infty} A_j\omega^{\nu_j}P_{\nu_j}(\mu_F)P_{\nu_j}(\mu_G);$$
$$M_{21} = C_{11}\sum_{j=0}^{\infty} A_j\omega^{\nu_j+1}P_{\nu_j}(\mu_F)P_{\nu_j}(\mu_G) + C_{12}\sum_{j=0}^{\infty} A_j\left[P_{\nu_j}(\mu_F)\right]^2;$$
$$M_{22} = C_{21}\sum_{j=0}^{\infty} A_j\omega^{\nu_j+1}P_{\nu_j}(\mu_F)P_{\nu_j}(\mu_G) + C_{22}\sum_{j=0}^{\infty} A_j\left[P_{\nu_j}(\mu_F)\right]^2;$$
$$\omega = \frac{R_G}{R_F} \tag{3.51}$$

It is clear that the matrix M must equal identity, which yields two pairs of equations for the capacitance coefficients.

As a practical matter, the summations whose terms do not include the ω factor exhibit poor convergence. Effectively this is the problem of evaluating the potential in equation (3.49) directly on the charged rings. With 200 terms, accurate values for the potential in Equation (3.49) can be obtained everywhere in the range $|r-R_G|>0.04\ R_G$ and $|r-R_F| > 0.04\ R_F$. To compute the voltage directly on the gate ring, we use

$$V_G\left(r = R_G, \mu = \mu_G\right) \approx V_G\left(r = 0.96R_G, \mu = \mu_G\right) - E_{Gr}\left(r = 0.96R_G, \mu = \mu_G\right)\left(0.04R_G\right) \tag{3.52}$$

where E_{Gr} is the radial electric field due to the gate ring. The explicit expression for E_{GR} will be given shortly.

One more point needs to be mentioned. Computation of Legendre functions of higher orders is fairly time consuming, particularly for negative arguments. In fact it was

not possible to compute values of $P_\nu(x)$ when $\nu > 100$ *and* $x < 0$. The difficulty may be due to a bug in Mathematica whose earlier versions had major problems with higher order Legendre functions. This means that our model as currently implemented in Mathematica could not be used to compute capacitance values when the tip is above the plane of the gate, but this configuration is rare.

3.3.3 Derivation of the Gate and Focus Field Factors, β_G and β_F.

With two electrodes, the electric field at the apex of the tip is given by the radial derivative of **Equation (3.49)** truncated at k=0:

$$E_A \equiv E(r = R_T, \theta = 0) = \frac{\partial V(r = R_T, \theta = 0)}{\partial r} \approx$$

$$\frac{C_{11}V_G + C_{21}V_F}{R_T} A_0 P_{0.2}(\mu_G)\left(\frac{R_T}{R_G}\right)^{0.2} 0.2\left(1+6\gamma^{1.4}\right) + \frac{C_{12}V_G + C_{22}V_F}{R_T} \omega A_0 P_{0.2}(\mu_F)\left(\frac{R_T}{R_G}\omega\right)^{0.2} 0.2\left(1+6\gamma^{1.4}\right) =$$

$$\left(\frac{A_0 P_{0.2}(\mu_G)(R_T/R_G)^{0.2}\, 0.2\left(1+6\gamma^{1.4}\right)}{R_T}\right)\left(C_{11}V_G + \frac{P_{0.2}(\mu_F)}{P_{0.2}(\mu_G)} C_{21}V_F + \omega^{0.2} C_{12}V_G + \frac{P_{0.2}(\mu_F)}{P_{0.2}(\mu_G)} \omega^{0.2} C_{22} V_F\right); \tag{3.53}$$

We can re-write this in terms of gate and focus field factors as:

$$E_A = \beta_G V_G + \beta_F V_F$$

$$\beta_G = \left(\frac{A_0 P_{0.2}(\mu_G)(R_T/R_G)^{0.2}\, 0.2\left(1+6\gamma^{1.4}\right)}{R_T}\right)\left(C'_{11} + \omega^{0.2} C'_{12}\right)$$

$$\beta_F = \left(\frac{A_0 P_{0.2}(\mu_G)(R_T/R_G)^{0.2}\, 0.2\left(1+6\gamma^{1.4}\right)}{R_T}\right)\left(\frac{P_{0.2}(\mu_F)}{P_{0.2}(\mu_G)}\right)\left(C'_{21} + \omega^{0.2} C'_{22}\right) \tag{3.54}$$

It is particularly interesting to find an expression for the *ratio* of the gate and focus field factors as it determines the relative effect of each electrode on the emission current:

$$\frac{\beta_F}{\beta_G} = 1.1 \frac{\left(C'_{21} + \omega^{0.2} C'_{22}\right)}{\left(C'_{11} + \omega^{0.2} C'_{12}\right)} \tag{3.55}$$

3.3.4 Trajectory Calculations

In the final stage of our analysis we apply the model to trajectory calculations. The electric fields throughout all space are given by the gradient of Equation **(3.49)**:

$$E_r(r,\theta)=\begin{cases} -\dfrac{Q_G}{4\pi\varepsilon_0 rR_G}\sum_{j=0}^{\infty}A_jP_{\nu_j}(\mu_G)P_{\nu_j}(\mu)\times\left(c_j\left(\dfrac{r}{R_G}\right)^{c_j}+\left(\nu_j+1\right)\left(\dfrac{R_\varepsilon^{2\nu_j+1}}{R_G^{\nu_j}r^{\nu_j+1}}\right)\right)+ \\ -\dfrac{Q_F}{4\pi\varepsilon_0 rR_F}\sum_{k=0}^{\infty}A_kP_{\nu_k}(\mu_F)P_{\nu_k}(\mu)\times\left(c_k\left(\dfrac{r}{R_F}\right)^{c_k}+\left(\nu_k+1\right)\left(\dfrac{R_\varepsilon^{2\nu_k+1}}{R_F^{\nu_k}r^{\nu_k+1}}\right)\right) \end{cases} \tag{3.56}$$

$$E_\theta(r,\theta)=\begin{cases} -\dfrac{Q_G}{4\pi\varepsilon_0 rR_G}\sum_{j=0}^{\infty}A_jP_{\nu_j}(\mu_G)\dfrac{\mu\nu_jP_{\nu_j-1}(\mu)-\nu_jP_{\nu_j}(\mu)}{\sqrt{1-\mu^2}}\times\left(\left(\dfrac{r}{R_G}\right)^{c_j}-\dfrac{R_\varepsilon^{2\nu_j+1}}{R_G^{\nu_j}r^{\nu_j+1}}\right)+ \\ -\dfrac{Q_F}{4\pi\varepsilon_0 rR_F}\sum_{k=0}^{\infty}A_kP_{\nu_k}(\mu_F)\dfrac{\mu\nu_kP_{\nu_k-1}(\mu)-\nu_kP_{\nu_k}(\mu)}{\sqrt{1-\mu^2}}\times\left(\left(\dfrac{r}{R_F}\right)^{c_k}-\dfrac{R_\varepsilon^{2\nu_k+1}}{R_F^{\nu_k}r^{\nu_k+1}}\right) \end{cases} \tag{3.57}$$

In Cartesian coordinates, which are more convenient for trajectory calculations and focusing analysis, the fields become:

$$E_x(x,y)=-\frac{\partial V}{\partial x}=\frac{x}{\sqrt{x^2+y^2}}E_r\left(\sqrt{x^2+y^2},\frac{y}{\sqrt{x^2+y^2}}\right)+\frac{y}{\sqrt{x^2+y^2}}E_\theta\left(\sqrt{x^2+y^2},\frac{y}{\sqrt{x^2+y^2}}\right) \tag{3.58}$$

$$E_y(x,y)=-\frac{\partial V}{\partial y}=\frac{y}{\sqrt{x^2+y^2}}E_r\left(\sqrt{x^2+y^2},\frac{y}{\sqrt{x^2+y^2}}\right)-\frac{x}{\sqrt{x^2+y^2}}E_\theta\left(\sqrt{x^2+y^2},\frac{y}{\sqrt{x^2+y^2}}\right) \tag{3.59}$$

It is now straightforward to calculate trajectories via Newton's equation, which is easily implemented in Mathematica's numerical solver for differential equations. It is impossible to calculate trajectories starting from the equipotential surface that is used to represent the tip because it has positive potential. It would be equivalent to placing electrons in a potential well. Thus, trajectories need to be started directly on the surface of the bowling pin, which causes the beam to have a larger angular spread than in a real device. Despite this, trajectories present strong evidence of the collimation effect of the focus ring, as demonstrated in **Figure 3-10.**

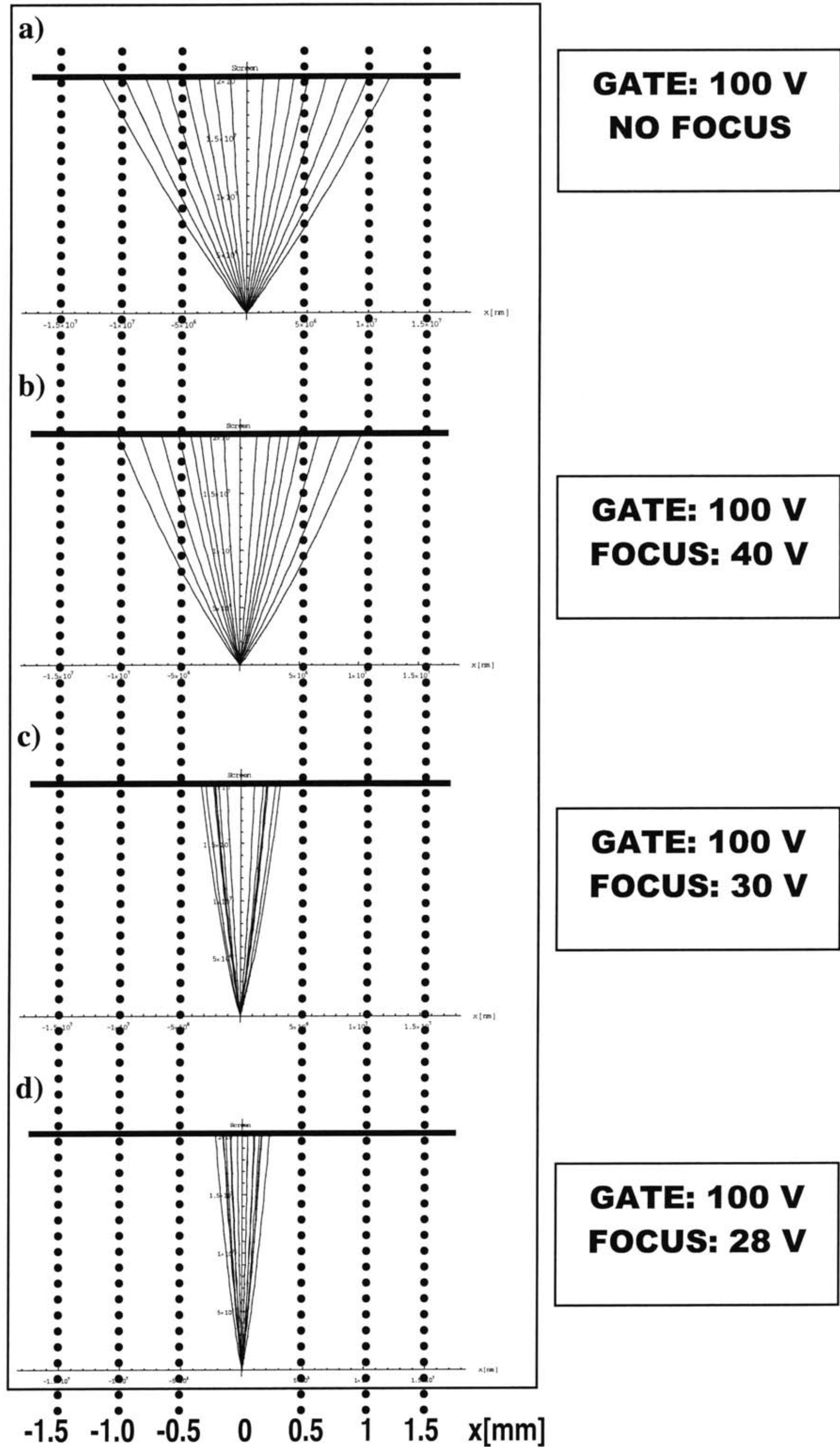

Figure 3-10. Trajectory calculations for a double gate device demonstrating the focusing effect (VG=100V) (a) no focus electrode (b) V_F=40 V (c) V_F=30 V (d) V_F=28V. Gate radius 700 nm; focus radius 900 nm. Gate co-planar with the tip, focus 600 nm above the tip. Tip ROC 10 nm; work function: 3.5 eV. Cone base angle: 126°. Trajectories launched at angles 5-40°, in 5° increments.

3.4 Chapter Summary

In this chapter we have developed an analytical model applicable to a conical field emitter with a single or multiple gates. The model is based on using the orthonormal basis of Legendre functions to expand the potential of charged ring(s) in the presence of a grounded "bowling pin", i.e. a cone with a sphere centered on its apex. The Bowling Pin Model enabled us to prove the validity of the empirical IV equation for field emitters (**Equation (3.2)**)

$$\ln\left(\frac{I}{V^2}\right) = a_{FN} + \frac{b_{FN}}{V}$$

and to derive closed form expressions for the coefficients a_{FN} and b_{FN} (**Equations (3.42) - (3.47)**) that depend only on the geometric parameters of the device – the tip radius of curvature and the gate radius:

$$a_{FN} = -8.5 + Log\left[\alpha' C_G'^2\right] + 2\nu_0 Log\left[\frac{R_T}{R_G}\right] + 2Log\left[\frac{\nu_0 + (1+\nu_0)\gamma^{1+2\nu_0}}{1-\delta}\right]$$

$$b_{FN} = -59\frac{R_G^{\nu_0} R_T^{1-\nu_0}}{C_G'\left(\nu_0 + (1+\nu_0)\gamma^{1+2\nu_0}\right)}(1-\delta)$$

R_T is tip radius of curvature (ROC) in *nm*;

R_G is the gate radius in *nm*, measured as the distance from the tip to the gate. The equations above have been confined to the case of the gate co-planar with the tip, since it is the most common. In this case, R_G is equal to half the gate diameter.

$0.2 < \nu_0 < 0.4$ ($\nu_0 = 0.2$ will be used in fitting data)

$0.4 < \gamma < 0.6$

$\delta \approx 0.92 C_G'\left(\frac{R_T}{R_G}\right)^{\nu_0}\left(1-\gamma^{1+2\nu_0}\right)$

$Log(\alpha') \approx -2$

C_G' is an adjustable parameter of order 1. It is independent of R_G and R_T. An analytical approximation to C_G' has been derived.

Equations for a_{FN} and b_{FN} can be recast into other useful forms, such as the expression for the total emission current, *I*, in terms of the emission current density at the apex, J_A (**Equation (3.27)**):

$$I = 2\pi R_{TIP}^2 \alpha' J_A = 0.14 \times 2\pi R_{TIP}^2 \times J_A$$

And also the expression for the gate field factor, β, which relates the the electric field at the apex to gate voltage (**Equation (3.26)**):

$$\beta \equiv \frac{E_A}{V_G} \approx 0.9\, C_G{}' \frac{1}{R_T}\left(\frac{R_T}{R_G}\right)^{\nu_0} \frac{\left(\nu_0 + \left(1+\nu_0\right)\gamma^{1+2\nu_0}\right)}{1-\delta}$$

The field factor, which effectively sets the operating voltage of the device, is seen to be strongly dependent on the tip radius of curvature. The exact form of this dependence given by the BMP is in agreement with the results from finite element (FEM) simulation, and is more accurate than other analytical models.

In addition, the BPM

- captures the true geometry of a circular gate around a conical field emitter and describes the dependence of the field factor on gate radius

- explains the effect of the vertical position of the gate with respect to the tip through gate-to-cone capacitance

- demonstrates the importance of tip eccentricity through the γ parameter.

Extension of the BPM to double-gated emitters produced expressions for the gate and focus field factors in terms of four capacitance coefficients (**Equation (3.54)**):

$$E_A = \beta_G V_G + \beta_F V_F$$

$$\beta_G = \left(\frac{A_0 P_{0.2}\left(\mu_G\right)\left(R_T/R_G\right)^{0.2} 0.2\left(1+6\gamma^{1.4}\right)}{R_T}\right)\left(C_{11}' + \omega^{0.2} C_{12}'\right)$$

$$\beta_F = \left(\frac{A_0 P_{0.2}\left(\mu_G\right)\left(R_T/R_G\right)^{0.2} 0.2\left(1+6\gamma^{1.4}\right)}{R_T}\right)\left(\frac{P_{0.2}\left(\mu_F\right)}{P_{0.2}\left(\mu_G\right)}\right)\left(C_{21}' + \omega^{0.2} C_{22}'\right)$$

A way to compute the capacitance coefficients for a given device geometry has been presented making it possible to predict the relative effects of the gate and focus electrodes on the apex electric field and hence on the emission current (**Equations (3.54) – (3.55)**).

Finally, by differentiating the potential expansion we obtained radial and angular electric fields. Converting these into Cartesian form, we carried out trajectory calculations, shown in **Figure 3-10**, which clearly demonstrate how lowering the focus bias collimates the electron beam. Thus, while the primary use of the BMP has been in the computation of the emission current, it also provided a proof of the focusing concept.

All of the preceding constitutes original contributions by the author.

4 Fabrication of IFE-FEA

4.1 Formation of 3-micron Tall Silicon Tip

First, thermal oxide is grown and patterned into 1 micron diameter disks by photolithography and reactive ion etch (RIE) (**Figure 4-1A**). It was found that to achieve vertical sidewalls in the oxide disk (**Figure 4-2 A**) – needed to get a good tip – it was necessary to get vertical sidewalls in the photoresist mask. This was obtained through careful monitoring of exposure and development parameters and addition of the post-exposure bake. Specifically, the photolithography step was as follows: coat—soft bake (115 °C) –expose—*post exposure bake* (100 °C) —develop (130 °C) —hard bake. High pressure, low power SF_6 plasma generated a fairly isotropic etch, the lateral to vertical etch ratio being about 0.57 (**Figure 4-2B**), which ultimately produced the desired tip geometry (**Figure 4-2C**). This part closely followed the work of Dr. Han Kim who developed a process for making uniform arrays of silicon tips by isotropic plasma etch and oxidation sharpening in our laboratory, as shown in **Figure 4-1A-B** [92].

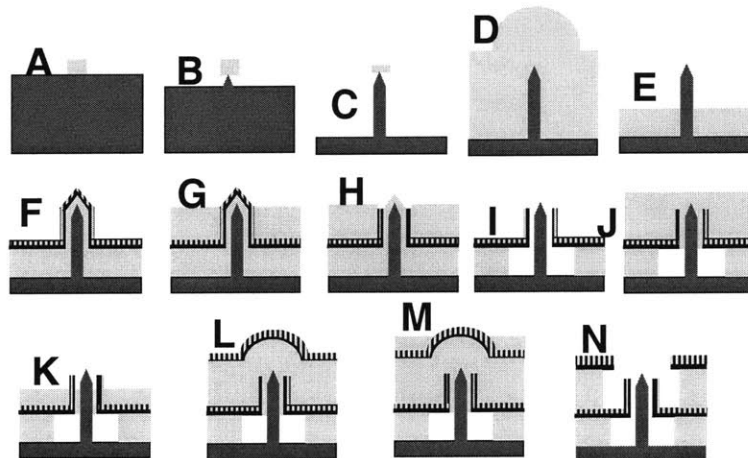

Figure 4-1. Self-Aligned CMP-based process for making L/OP silicon IFE-FEA.

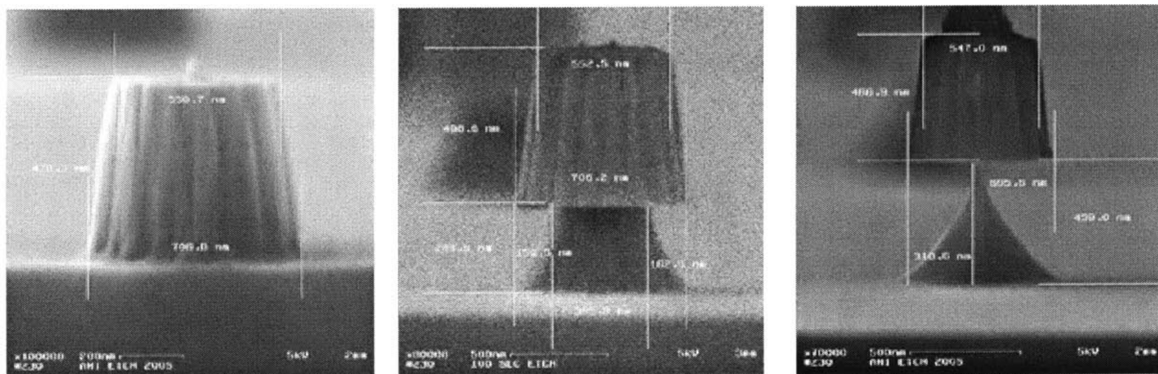

Figure 4-2. (A) Oxide disk serves as a mask for tip formation. (B) Partially formed silicon tip. (C) Fully formed tip (by isotropic plasma etch) [*c.f. Figure 4-1 A-B*]

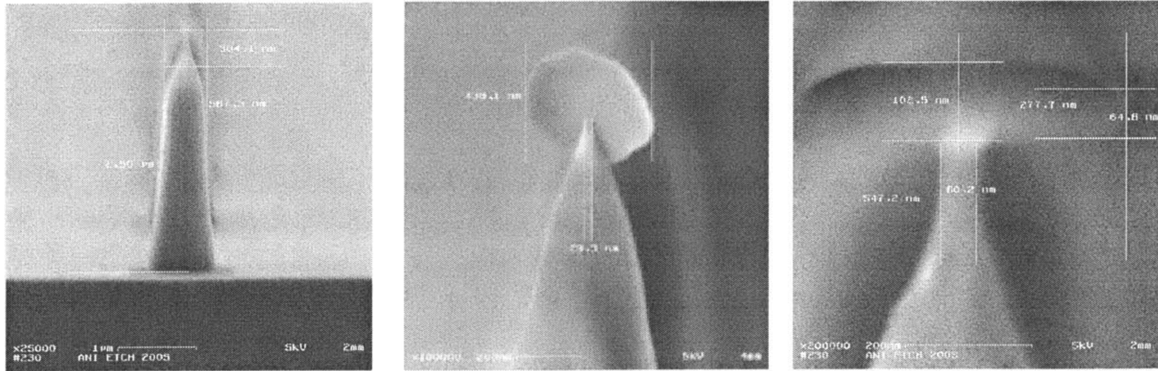

Figure 4-3. (A) High aspect ratio silicon tip after anisotropic RIE etch (60° tilt). (B) Close-up of the tip and oxide mask after RIE etch (C) Approx. 80% of the oxide mask was etched by RIE. ***[c.f. Figure 4-1 C]***

In Dr. Kim's process the tip would now be sharpened via dry thermal oxidation. However, for our purposes the tip height of 0.5-1 micron was insufficient. It was increased using high power, low pressure silicon reactive ion etch (RIE), as seen in **Figure 4-3 A**. **Figure 4-3 B-C** show that RIE also removed about 0.4 μm of the oxide cap, more around the edge. In fact, the necessary oxide mask thickness (0.5 μm) was determined in advance based on the silicon / oxide etch rate selectivity was (~6 : 1). (More accurately, being green I first tried to do it with 0.25 μm oxide layer, got to the RIE step, *then* measured selectivity and went back to step one.)

4.2 Deposition, Planarization and Etchback of Gate Insulator

The next two steps, shown in **Figure 4-1 D-F**, illustrate a novel technique, developed by the author and used several times in the process. Using LPCVD, we deposit a low temperature oxide (LTO) layer that is thick enough to "submerge" the tip; in other words, the thickness of the LTO layer is greater than the tip height (by about 1 μm). The reason for this will become clear in the next step, which is chemical mechanical polishing (CMP).

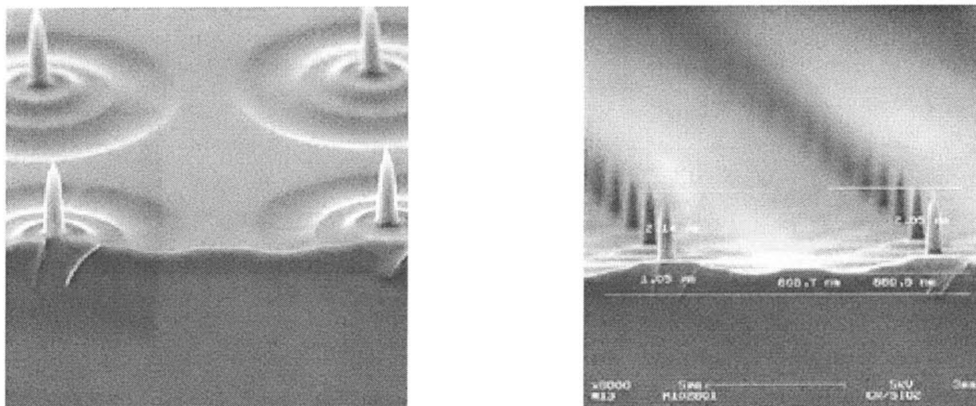

Figure 4-4. (A) Tips after LTO deposition, CMP, and etch back (60° tilt). (B) 90° tilt view with measurements. ***[c.f. Figure 4-1 E]***

In our lab, CMP does not offer a very uniform or controlled polish, and no SEM is available to examine the wafer between polishing steps without doing extensive cleaning. The thick LTO layer is meant to protect the silicon tip from damage in case of overpolishing, while CMP planarizes the oxide surface. In other words, CMP operates only on the sacrificial layer, whose exact thickness is immaterial, and never comes close to the tip. It can be seen in **Figure 4-4** that planarization is in fact imperfect. Somewhat better results were achieved in later runs by (a) replacing the single CMP step with the CMP – LTO deposition – CMP sequence and (b) not densifying the LTO until after the CMP. Undensified LTO, which consists of loose oxide particles, yields much better to planarization.

4.3 Oxidation Sharpening of the Tip and Formation of the Gate Electrode

No detailed micrographs are available for the next stage (**Figure 4-1 F**) because its five steps involve directly transferring the wafer between furnaces. Taking SEMs would slow down the process by necessitating extra cleans and is not necessary since monitoring is done on pilots. First, we grow 0.2 μm of dry thermal oxide, which serves a dual purpose of sharpening the tip and providing an insulator for the gate layer. Then, following Itoh's work [55], we deposit a thin nitride layer. The goal is to increase the length of the surface leakage path between the gate and the substrate (a.k.a. *creeping distance*), which would otherwise be equal to the thickness of the LTO layer. But in hindsight, this step probably makes no difference in our process, since the nitride film is most likely etched away during the subsequent extended buffered oxide etch (BOE) dip. Now we deposit a layer of *amorphous* silicon and dope it by ion implantation. Note that the high-temperature drive-in is not done until later to keep amorphous silicon from developing grain structure. The reason for this is that in our metal devices, described in Chapter 2, the gate was polysilicon and had a rough surface, which we believe contributed to oxide break-down via local field enhancement around surface protrusions.

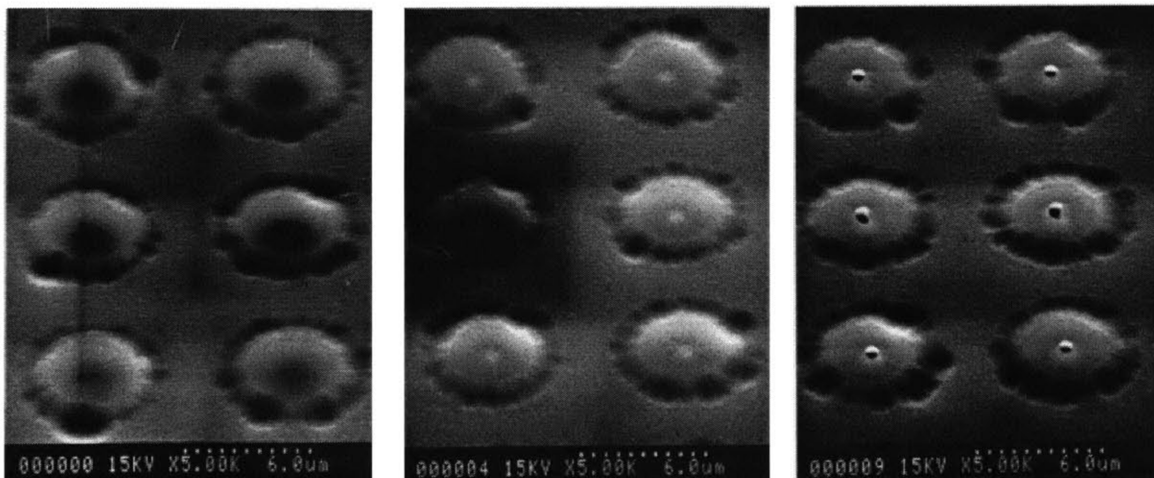

Figure 4-5. (A) LTO after planarization and densification (B) After 2 minute BOE dip, poly-Si gates are visible through thin LTO (C) After another 2 min BOE dip, which removes about 0.25 μm of densified LTO, poly-Si gates begin to protrude. ***[c.f. Figure 4-1 G]***

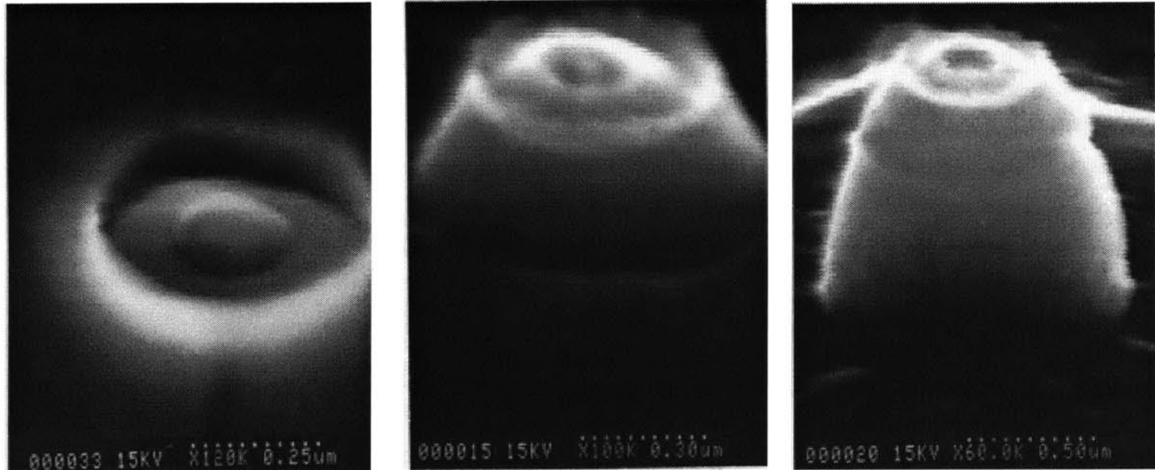

Figure 4-6. (A) Polysilicon gate recessed by isotropic etch ***[c.f. Figure 4-1 H]*** **(B) Polysilicon gate and tip after a two minute BOE dip (C) Fully exposed polysilicon gate and a partially etched tip after a 25 minute BOE dip.** ***[c.f. Figure 4-1 I]***

Now, the sequence of 'LTO deposition – CMP – BOE etchback' will be used to open gate aperture. In single-gate devices, gate aperture can be opened by carefully monitored CMP which stops on the upper surface of the gate electrode, without damaging the tip. (In theory at least... This method is tricky even in single gate devices.) Here this method is unusable because the tip protrudes far above the plane of the gate. Instead, planarized, densified LTO is gradually etched back until the top of the gate electrode begins to protrude (**Figure 4-5**). If the LTO is etched *past* this point, the gate aperture will end up being too far below the tip. As another solution to the LTO overetch problem, we made an attempt to open the gate aperture with thermal oxidation, reasoning that it would be self-limiting in propagating down the gate, but the right oxidation time proved elusive.

After the gate aperture is opened by a carefully monitored anisotropic silicon RIE (**Figure 4-6A**), an extended BOE dip (25 minutes) is used to etch the oxide all the way down to the substrate. The difference in the appearance of the tip between **Figure 4-6 B** and **Figure 4-6 C** shows that BOE also shortened the silicon tip by about 30 nm, as it no longer protrudes through the gate aperture. This is important because it necessitates another sharpening oxidation step at the end. In a lab where concentrated HF is available, it would preferable here. **Figure 4-7 A-B** shows the devices after this step.

4.4 Deposition, Planarization and Etchback of the Focus Insulator and Formation of the Focus Electrode

LTO deposition (**Figure 4-7 C**), followed by planarization (**Figure 4-8A**) and etchback (**Figure 4-8 B**), brings us back to the structure first shown in **Figure 4-6 B** (**Figure 4-8 B**). The only difference is that now there is no oxide between the gate and the tip. Now we deposit another 0.3 μm LTO, so that the top surface of the oxide is approximately level with the tip, followed by 0.3 μm of amorphous silicon to surface as

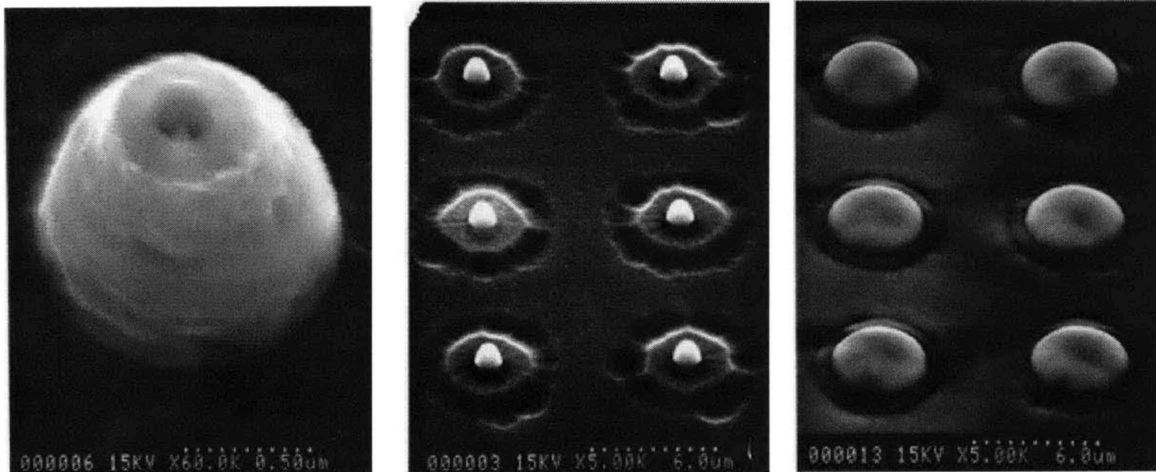

Figure 4-7. (A) and (B) Fully exposed polysilicon a 25 minute BOE dip. ***[c.f. Figure 4-1 I] (C) LTO layer covering the gate***

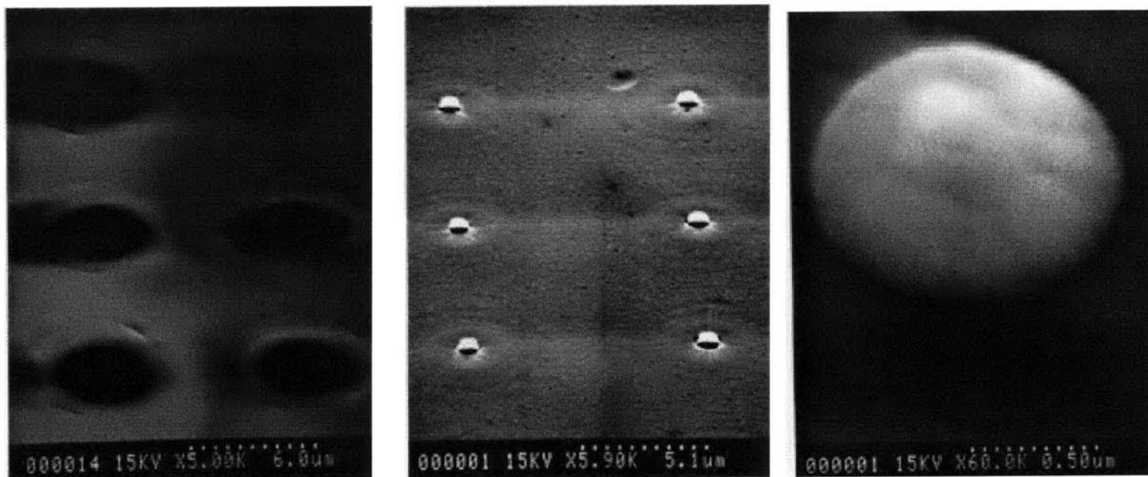

Figure 4-8. (A) LTO layer after CMP (c.f. Figure 4-1J) (B) Planarized LTO layer after a brief BOE etchback(c.f. Figure 4-1 K) (C) Thin LTO layer deposited over the exposed gate electrode.

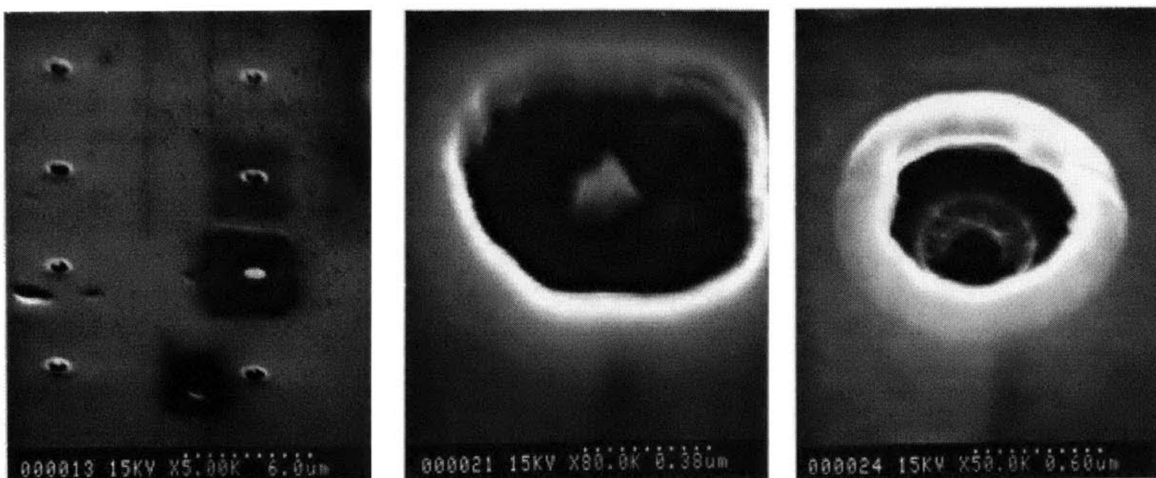

Figure 4-9. (A) Etched back LTO exposes the top of the focus electrode (c.f. Figure 4-1 M) (B) Focus electrode aperture opened with RIE, before BOE etch-back of the oxide (C) After BOE etch removes the masking LTO layer, the device is completed (c.f. Figure 4-1 N)

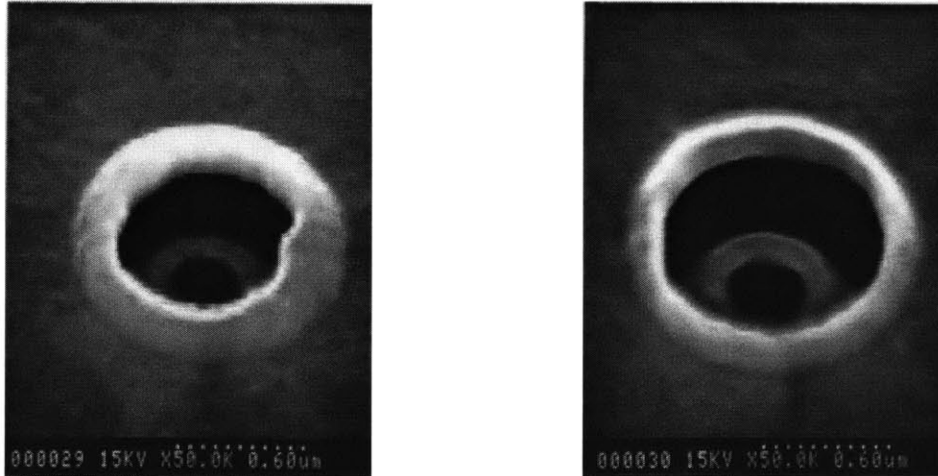

Figure 4-10. (A) and (B) Focus aperture and height varies somewhat between different dies.

the focus electrode. The focus aperture is opened in the same way as the gate aperture – LTO deposition, planarization, oxide etchback, and silicon dry etch (**Figure 4-9 B**). **Figure 4-10 A-B** shows that there is a slight difference in the diameter and vertical extent of focusing apertures of different devices, depending on the extent to which the corresponding oxide masks were etched back.

After contact patterning, and a brief oxidation resharpening, devices are basically completed (**Figure 4-11**). The last step is angular ion implant into the focus layer (avoiding the tip) and rapid thermal anneal (RTA).

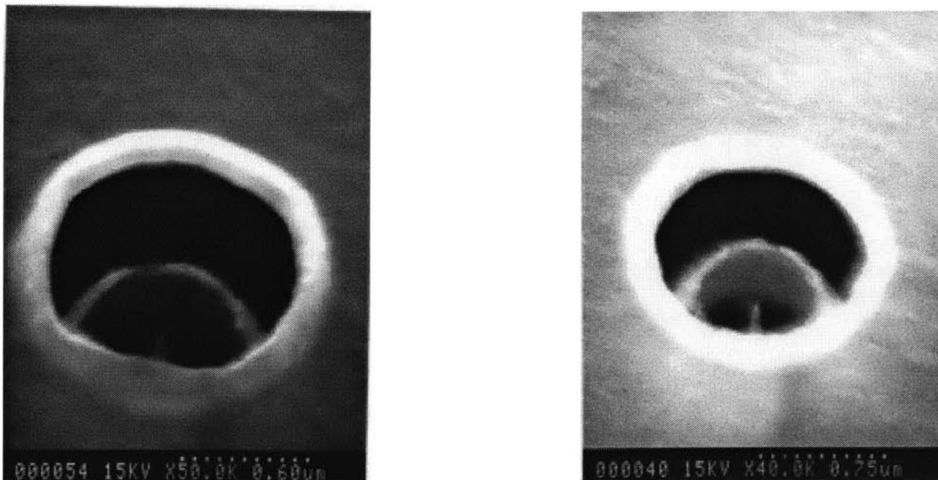

Figure 4-11. (A) and (B) 30° tilt SEM micrographs of completed IFE-FEAs (c.f. Figure 4-1 N)

4.5 Chapter Summary

This chapter presented the author's novel process for fabrication of IFE-FEA. The fabrication sequence was extensively documented with SEM micrographs of intermediate steps. Whereas the smallest devices with this geometry previously reported in the literature had gate and focus radii of 1.2. and 2.2 μm respectively, our process is capable of achieving gate and focus radii of 0.25 and 0.4 μm.

The most laborious step in the process is opening the gate aperture (**Figure 4-1H**, **Figure 4-5**, **Figure 4-6**), which requires several timed wet etch steps of the oxide and two or three timed dry etch steps of polysilicon, with SEM inspections after each step.

With the benefit of knowing final device performance, it would make sense to modify the process in a couple of ways. First, the tips could be made taller by about 1 μm to allow greater thickness of the insulator (1.5 μm of oxide in each insulating layer would be excellent). Second, it would pay to insure that planarization in step E (**Figure 4-4**) is highly uniform. In addition, we found out that CMP tends to damage focus electrodes of tips on the periphery of the array, most likely due to different polish rate. Emission beams from such tips cannot be collimated and add non-uniformities to the collimated beam coming from the inside part of the array. It makes sense to compensate for this by designing larger oxide disks around the array periphery. This would produce very dull tips that will not contribute to emission. Finally, 10 μm tip spacing was probably too much of a safety margin. Reducing the spacing to 4-5 μm would lead to more densely packed arrays which would produce more uniform and stable electron beams for given array footprint. As an added benefit, with reduced tip-to-tip spacing, it may be easier to achieve good planarization after step D (**Figure 4-1D**) because oxide bumps over neighboring tips will begin to merge.

5 IV Characteristics of IFE-FEA

5.1 Measurement Setup

Measurements were conducted in a UHV chamber, at pressures of about 2×10^{-9} Torr. Instrumentation included a high-resolution current meter, Keithly 6517; three Source-Measure units (Keithly 237), capable of simultaneously sourcing voltage and measuring current; and Labview, a computer interface program which provided remote control of the instruments and collected the data over the GPIB. This setup is shown in **Figure 5-1**.

Electrical contact to the gate and focus electrodes of the device was made through sharp probes positioned on the contact pads with the aid of a microscope and micromanipulators. To eliminate vibration that would break the probe contacts, the UHV chamber was mounted on a floating optical table. Since the cathode of the device was built right on the wafer substrate, it was contacted directly through the metallic stage on which the wafer was mounted. (The stage was isolated from ground.) Shielded triaxial cable was used for all signals to minimize noise and interference.

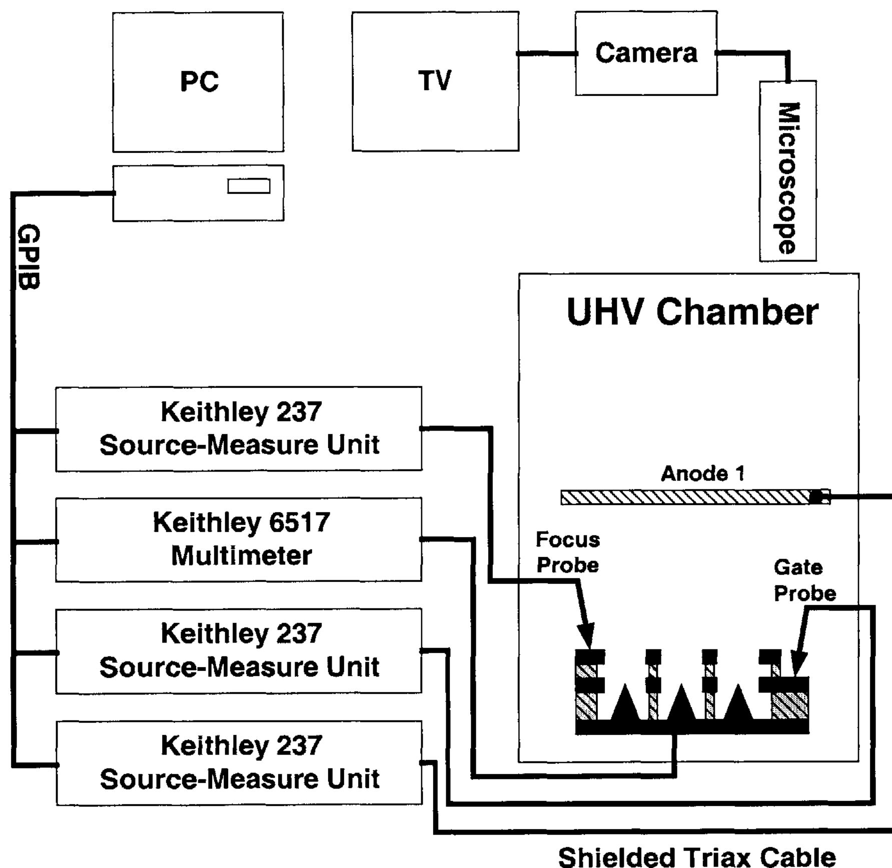

Figure 5-1. Diagram of the measurement setup.

In this chapter we will talk about two kinds of measurements – 3-terminal and 4-terminal. 3-terminal measurements refer to current and voltage measurements of the cathode, gate, and anode. In a single-gate FEA, which is the subject of the first half of this chapter, all measurements are by default 3-terminal. In a double-gate FEA, shown in **Figure 5-1**, there are in general 4 terminals: cathode, gate, focus, and anode. However, when the gate and focus electrode are always kept at the same voltage, the measurements are also referred to as 3-terminal. While not useful for focusing purposes, 3-terminal measurements on IFE-FEAs provide useful insight into device emission characteristics.

5.2 IV Characteristics of Single-Gate FEAs

5.2.1 Device Description

The devices we call single-gate FEAs (SG-FEAs) are in reality failed IFE-FEAs. Thus, arrays shown in **Figure 5-2A** actually have two contact pads, gate and focus. (The sizes of the arrays shown in that figure are 100x100, 50x50, 25x25, 10x10, 5x5, and 1x1, with the tips on a 10 μm pitch in all cases.) A processing miscalculation late in the process made the focus aperture about 8 times larger than intended (4.5 μm radius instead of 0.6 μm radius), so that it had no observable effect on any aspect of device behavior. However, since this SG-FEA wafer was in the same batch as the one with good IFE-FEA devices, and thus had identical gate geometry and tip structure **(Figure 5-2B)**, it provided a useful aid to characterizing IFE-FEAs.

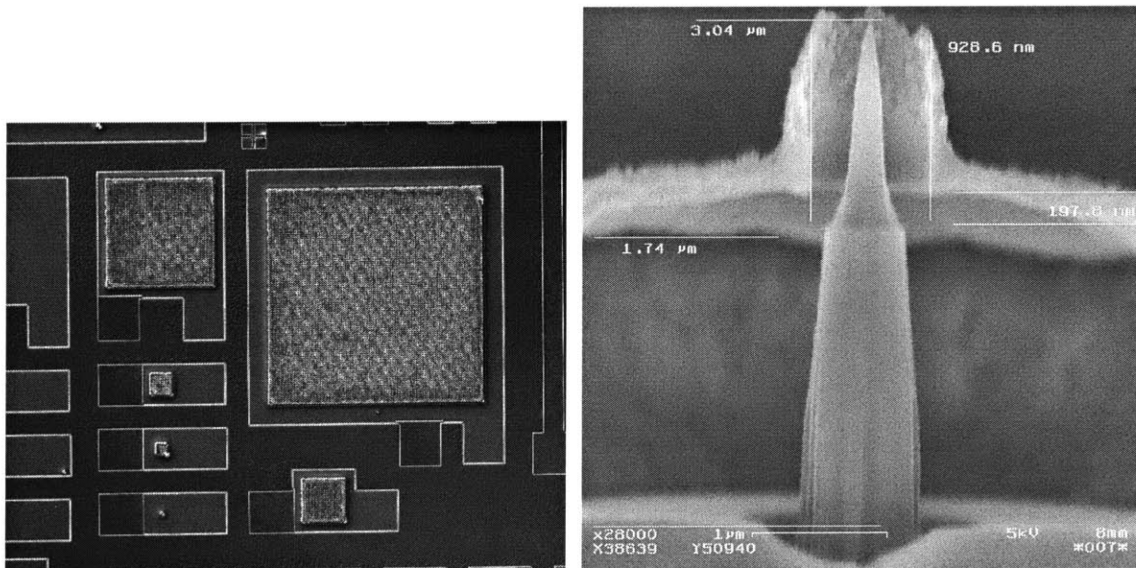

Figure 5-2. (A) Single-gate FEA arrays of different sizes. (B) Cross-section of a SG-FEA. (Photos courtesy of I. Kymissis)

5.2.2 Turn-on Voltage

Reports on FEA performance and comparisons of different devices often begin with the so-called "turn-on voltage [93,94]." It's a how-low-can-you-go game, and the authors – including yours truly [95] – proudly tout their accomplishments. The turn-on voltage (TOV) is attractive as a metric because, unlike the FN slope and intercept, it seems to have an immediate physical meaning, but this is illusory. Philosophically, the present definition is propagating a subjective view of field emission, since we say that the device turned on only when we can observe it. And that just means the emission current from an array of a given size (e.g. 100 x 100) has exceeded the noise floor of our particular measurement system (<5 pA for the data in **Figure 5-3**). While this author is too ignorant to opine on whether a tree makes noise when it falls in the forest where no one can hear it, he is convinced that emitters do actually produce femtoamp currents, be they as it may beyond our measurement capabilities. Thus, a more precise definition of the turn-on voltage could be useful. Assuming all tips are emitting equally, emission from a 100x100 array will exceed the noise floor of 5 pA when the current from each tip is 1 fA, with the corresponding total current equal to 10 pA. It seems convenient to define the corresponding voltage as the turn-on voltage, i.e.

$$I_{TIP}\left(V_{turn-on}\right) \equiv 1\, fA \qquad \textbf{(5.1)}$$

When the system noise is higher, or when the largest available array is smaller than 100x100, the value of the turn-on voltage can be computed from the FN parameters. The turn-on voltage is now well defined though still redundant. In the next section, the FN slope and intercept for array emission data normalized to the number of tips will be computed to be –500 and –8.3 respectively. Then the calculated turn-on voltage is 16 V. This is, of course, in perfect agreement with what is shown in **Figure 5-3** because the definition was developed based on the specifications of our particular measurement set-up.

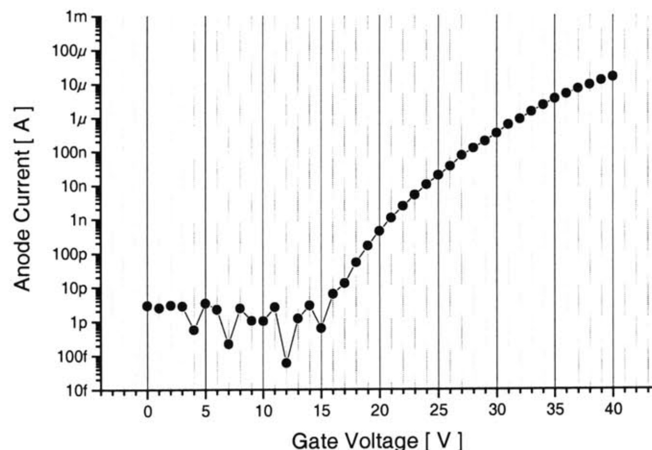

Figure 5-3. The observed turn-on voltage in this 50x50 array corresponds closely to the equivalent current of 1 fA per tip. In general, TOV is a redundant metric.

5.2.3 Measurement and Analysis of Fowler-Nordheim Coefficients

It was mentioned in the previous section that the turn-on voltage is essentially a redundant metric since the emitter is fully characterized by its Fowler-Nordheim coefficients. This section will demonstrate application of the FN coefficients to data analysis and device comparison. Obtaining a careful measurement of the FN coefficients requires more than a simple IV sweep. One needs to take into account inherent fluctuation in the emission current and make sure that it does not introduce systematic distortions into the data. The mechanisms causing current fluctuation are not well understood at present. In the words of a leading field emission expert [96]: *"To date many fundamental surface phenomena leading to flicker noise in microfabricated field emitters remain unknown. Changes in ϕ and β can be evoked; however, the details behind manifestation of these changes, such as the influence of various adsorbates on the local electric field if any, is unclear. Other factors arising from the adsorbate / surface interaction such as the modification of the local electron density of states and/or the electron tunneling barrier by resonant tunneling effects [97], are additional possibilities."* Our goal here is not to study noise but simply to ensure that it does not introduce spurious features into the data that will be used for the measurements of the FN coefficients. Of course, the fluctuation is expected to be less pronounced in larger arrays due to averaging. On the other hand, if only a single IV sweep data is available for a small array, there is no guarantee that it is indeed representative of device behavior. This problem can be addressed by doing a sequence of several IV sweeps. For the measurements presented here, 21 up-down IV sweeps were done in sequence. During the middle sweep (sweep # 11), at each value of the gate voltage, 20 current readings were taken and averaged. **Figure 5-4** through **Figure 5-6** show the data for 1x1, 5x5, 10x10, 25x25, and 50x50 arrays. (The current plotted on the y-axis is the anode current. Gate current was less than 5% – and often less than 1% – of the anode current at peak emission for all the data presented in this chapter.) Qualitatively it can be said that ensuring sweep-to-sweep uniformity in the data provides a guarantee against distortions due to adsorption-desorption (A-D) processes with a longer time constant, while averaging multiple current reading at each voltage point removes the effects of shorter time constant A-D processes.

Besides providing a careful measurement of the FN coefficients, the peak data is interesting in its own right. We note that 1x1 and 50x50 array exhibit clear effects of the burn-in period. It should be noted that investigation of the burn-in period was not a goal at the time data was collected. Therefore, some of the devices were probably run for other measurements, and hence underwent a burn-in period, immediately before the measurements presented here. This explains why 10x10 and 25x25 device data does not exhibit the burn-in effect, and why 5x5 data exhibits "inverse" burn-in effect. In practice, we always observed the emission current increase following a burn-in period, unless some tips were destroyed in the process. The data also exhibits the expected increase in peak-to-peak uniformity as a function of array size. Some arrays (10x10 and 50x50) exhibit systematic hysterisis in every peak, whereby current on the down sweep is higher than on the up sweep. In other words, tips emit better after being run at a higher current, possibly due to the effects of heating-induced desorption. However, other devices (5x5

and 25x25) demonstrate no such effect. **Figure 5-6B** illustrates the noise in the emission current of a 5x5 array through a plot of current vs. gate voltage as opposed to time.

The original plan was to extract the FN coefficients from peak # 11, which recorded the average of 20 current reading for each value of gate voltage. To eliminate the effects of hysterisis, the up-sweep (left) half of the peak is to be used. Bearing in mind that a variation of 20-30% is small for an exponential process, it can been seen that

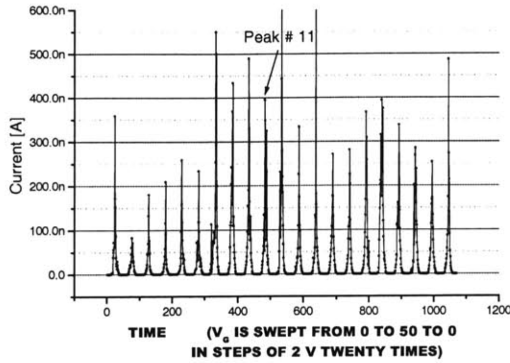

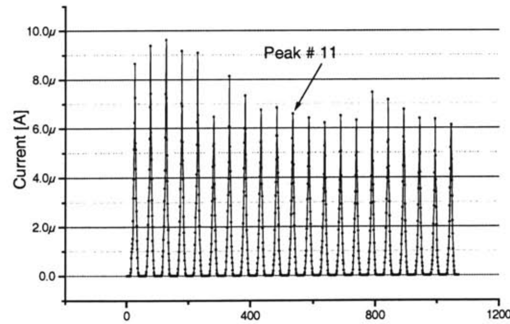

Figure 5-4. (A) IV sweeps for a 1x1 array (x: time) **(B) IV sweeps for a 5x5 array**

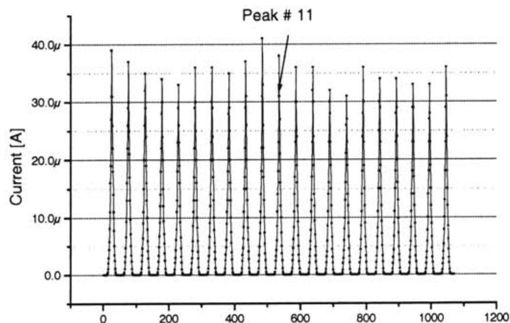

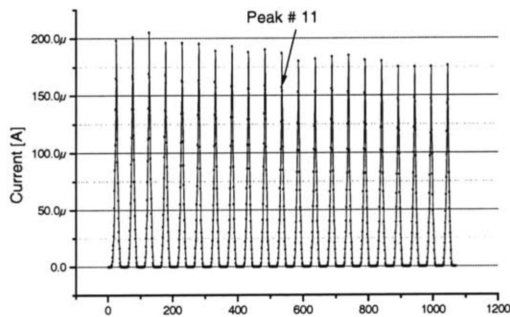

Figure 5-5. (A) IV sweeps for a 10x10 array **(B) IV sweeps for a 25x25 array.**

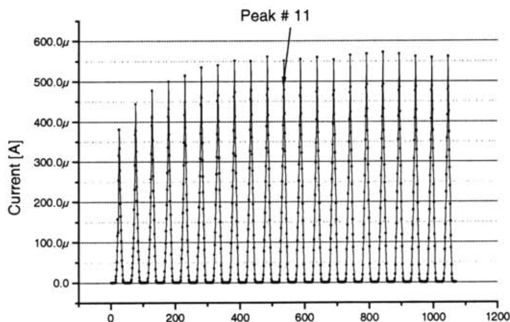

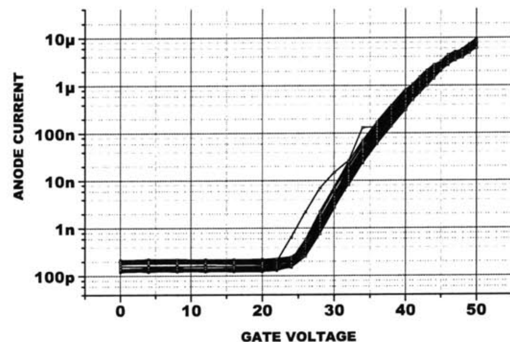

Figure 5-6. (A) IV sweeps for a 50x50 array **(B) Repeatability of current readings for a 5x5 array (same data as in Figure 5-5.)**

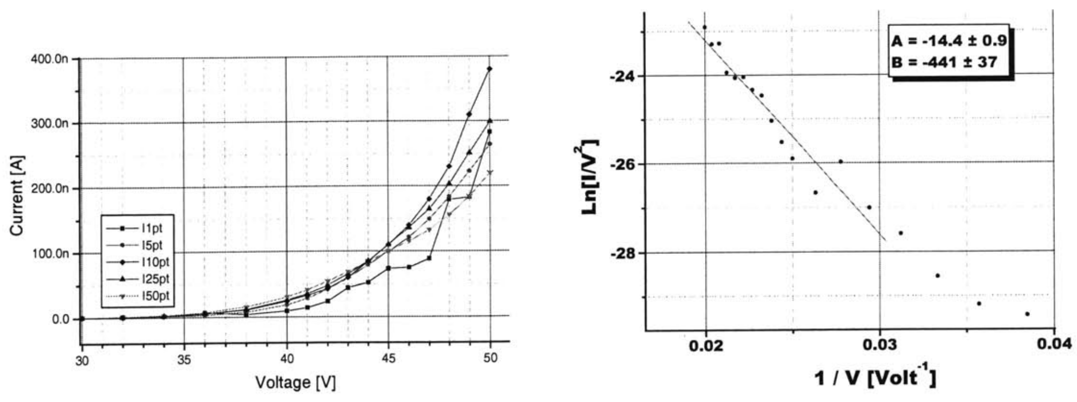

Figure 5-7 (A) Anode current as a function of gate voltage for different arrays, normalized to the number of tips. (B) FN plot for a 1 x 1 array.

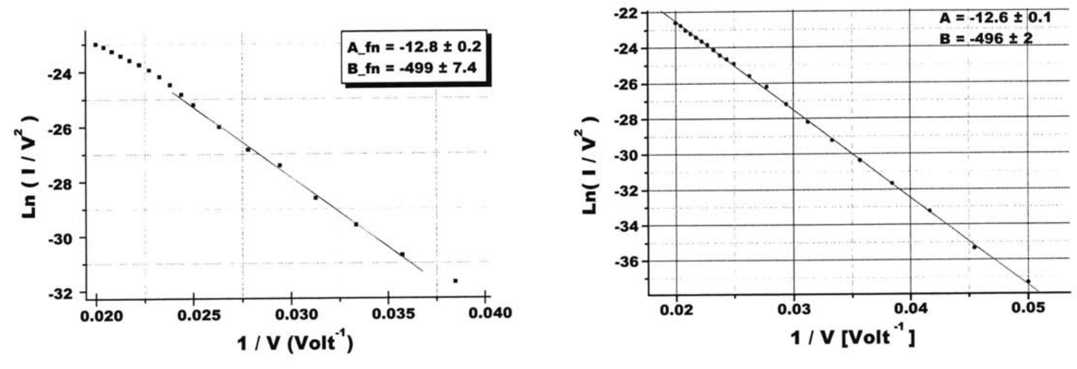

Figure 5-8. (A) FN plot for a 5 x 5 array. **(B) FN plot for a 10 x 10 array.**

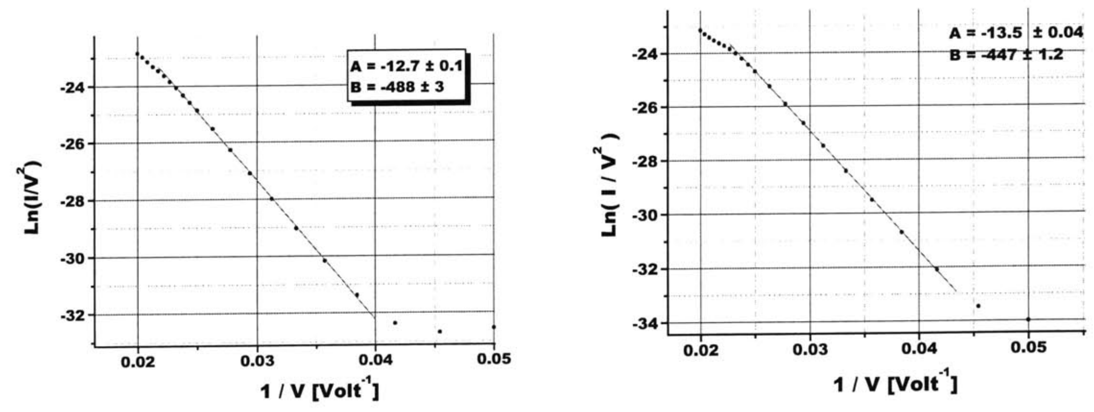

Figure 5-9. (A) FN plot for a 25 x 25 array. **(B) FN plot for a 50 x 50 array.**

peak # 11 is quite representative of device behavior, except in the case of the 1x1 array. Therefore, to compute the FN coefficient for the single tip device, current values for a given gate voltage from *all* 21 peaks were averaged (again, only data from the up-sweep

was included.) For all other devices, the left half of peak # 11 was used. The IV data thus obtained is shown in **Figure 5-7A**.

It can be seen from the FN plots (**Figure 5-7 — Figure 5-9**)that the FN coefficients show little variation from one array to another. This suggests that the total emitter current scales with the number of tips, or in other words, that the there is a high degree of tip-to-tip uniformity. In particular FN parameters of the 5x5, 10x10, and 25x25 arrays are virtually identical: a_{FN} = -12.7±0.1, b_{FN} = -493±5. If we include the data from the 50x50 array, the variation in b_{FN} among devices becomes about 10%.

To deduce the tip radius of curvature from the FN slope, a device model was built in Matlab (courtesy of Guobin Sha), and used via finite element method with the mesh shown in **Figure 5-10** to compute variation of the field factor $\beta = E_{APEX}/V_G$ with the tip ROC. The result, shown in **Figure 5-10**, comes out to:

$$\beta\left(10^5/cm\right) = 30.9/r^{0.76} \qquad \textbf{(5.2)}$$

From Equations (3-1) and (3-2) with the workfunction φ = 4.04 eV we have $\beta\left(10^5/cm\right) = -5500/b_{FN}$ which for the measured range of b_{FN} translates into

$$10.25 < \beta < 11.75 \quad \Rightarrow \quad 3.6\,nm < ROC < 4.2\,nm \qquad \textbf{(5.3)}$$

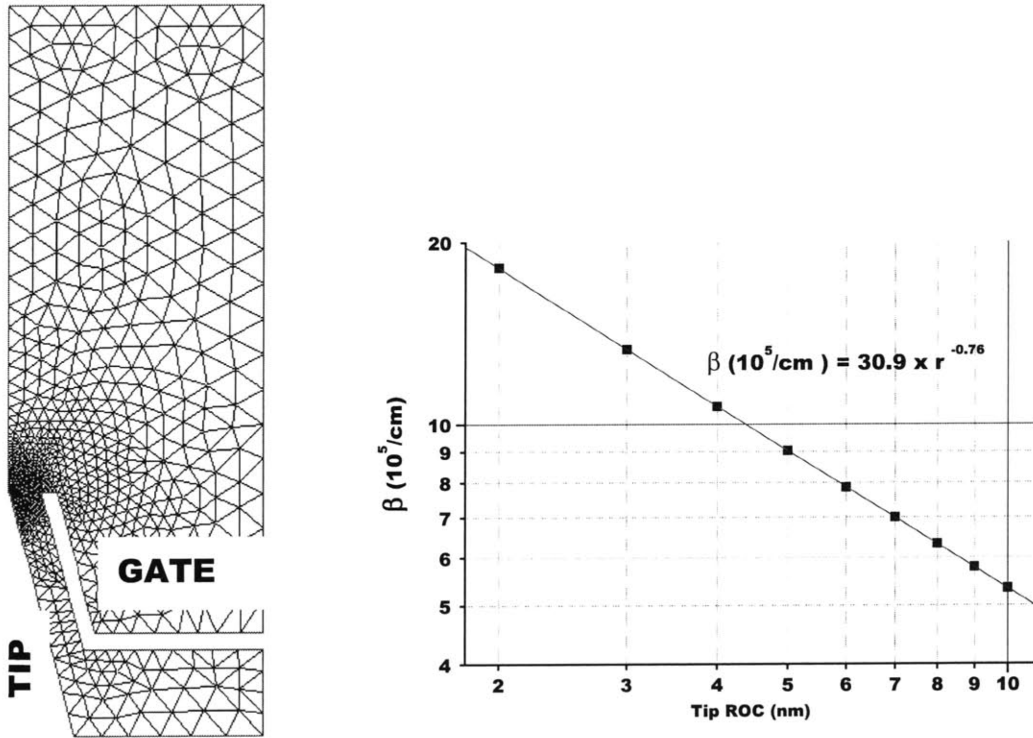

Figure 5-10. Mesh for a finite element method calculation of β vs. ROC and the resulting plot. Structure dimensions: Cone apex angle: 30°; cone height: 3000 nm; gate radius: 400 nm; gate thickness: 200 nm; gate to cathode plane distance: 1200 nm;

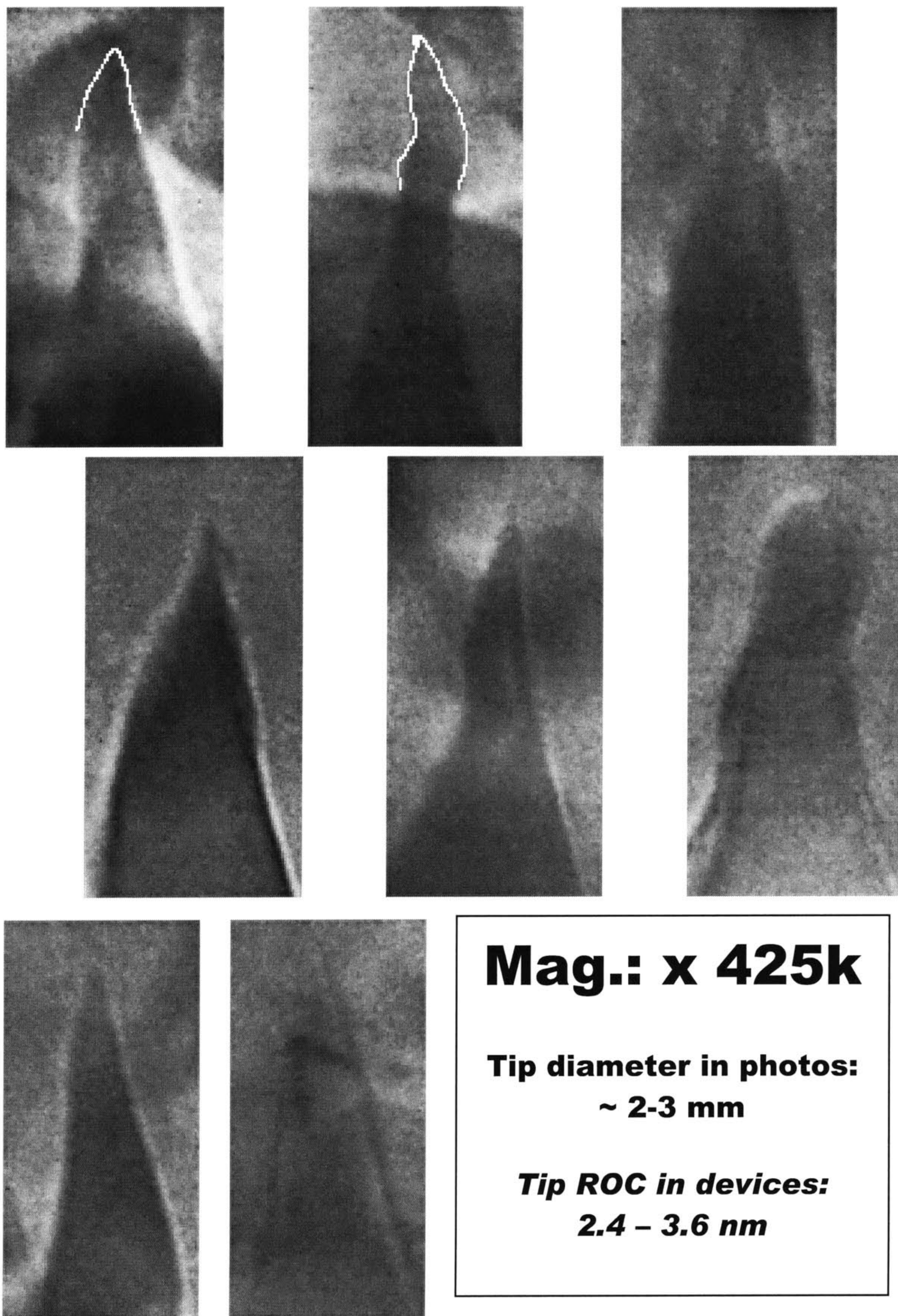

Figure 5-11. TEM micrographs of the emitter tips. (Courtesy of C-Y. Hong)

High magnification TEM micrographs of device tips, shown in Figure 5-11 produce ROC measurements falling in the 2.4 – 3.6 nm range.

There appears to be good agreement between measurements and calculations. A quick error analysis verifies this. The error in the measurement of tip diameter from the photos is about 0.5 – 1 mm, associated with the uncertainty in identifying tip boundary. Thus, $\sigma_{ROC}^{(TEM)} \sim 0.5-1\,nm$ or 25% of the ROC value. On the other hand, the error in the measured b_{FN} is, as we have seen, about 10%. The uncertainty in the resulting value of ROC is given by:

$$\sigma_r^{(B_{FN})} = \frac{\partial r}{\partial b_{FN}} \sigma_{B_{FN}}; \quad (r = ROC) \tag{5.4}$$

To evaluate the derivative we write an expression for b_{FN} as a function of ROC, take a logarithm of both sides, and differentiate with respect to b_{FN}:

$$\begin{aligned} &\beta = \frac{5500}{b_{FN}} = -\frac{30.9}{r^{0.76}} \\ &\Rightarrow 0.76 Log[r] + Log[c] = Log[b_{FN}] \\ &\frac{\partial}{\partial b_{FN}}: \quad \frac{0.76}{r}\frac{\partial r}{\partial b_{FN}} = \frac{1}{b_{FN}} \\ &\Rightarrow \frac{\partial r}{\partial b_{FN}} = 1.32\frac{r}{b_{FN}} \end{aligned} \tag{5.5}$$

The fractional uncertainty in ROC is thus about 1.3 times the fractional uncertainty in b_{FN}, i.e.

$$\frac{\sigma_r^{(b_{FN})}}{r} = 1.32\frac{\sigma_{b_{FN}}}{b_{FN}} \approx 13\% \tag{5.6}$$

The values of the ROC as deduced from TEM measurements and as computed from b_{FN} are thus seen to agree to within one sigma.

Having ascertained that the tip ROC is around 3.5 nm, we can use the Matlab model to compute the actual FN coefficients for the device in **Figure 5-10** and with the tip ROC = 3.5 nm. To accomplish this, we vary the voltage between 20 and 50 volts, and for each value of the voltage we compute the field along the tip and then numerically evaluate the integral in **Equation 3-27**. We obtain:

$$\textit{Finite Element Method}(\textit{Matlab}): \quad a_{FN} \approx -11; \quad b_{FN} \approx -475 \tag{5.7}$$

To get an independent calculation of the FN coefficients we turn to the BPM. From the summary of Chapter 3, we write down the BPM expressions for the FN coefficients and set them equal to the measured values:

$$\begin{cases} -10.5+2Log\left[C_G'\right]+2\nu_0 Log\left[\frac{R_T}{R_G}\right]+2Log\left[\frac{\nu_0+(1+\nu_0)\gamma^{1+2\nu_0}}{1-0.92\,C_G'\,(R_T/R_G)^{\nu_0}\left(1-\gamma^{1+2\nu_0}\right)}\right]=-12.7 \\ -59\frac{R_G^{\nu_0}R_T^{1-\nu_0}}{C_G'\left(\nu_0+(1+\nu_0)\gamma^{1+2\nu_0}\right)}\left(1-0.92\,C_G'\,(R_T/R_G)^{\nu_0}\left(1-\gamma^{1+2\nu_0}\right)\right)=-493 \end{cases} \tag{5.8}$$

We take $\gamma = 0.6$ rather than 0.4 because the tip TEMs are closest to Figure 5-4D (i.e. 'eccentricity' is lower). Other parameters are as before: $\nu_0 = 0.2$ and R_G = 400 nm for gate radius. Equation (5.8) is solved numerically to give:

$$BPM: \quad C_G' \approx 0.96 \quad R_T = ROC \approx 2.7\,nm \tag{5.9}$$

which is in excellent agreement with the TEM measurements. The value of the capacitance is also in good agreement with analytical estimates. The Bowling Pin Model has been validated!

As a final check, let's look at the value of the field factor obtained with this value of the capacitance. From the summary to Chapter 3,

$$\begin{aligned} \beta &\equiv \frac{E_A}{V_G} \approx 0.9\,C_G'\,\frac{1}{R_T}\left(\frac{R_T}{R_G}\right)^{\nu_0}\frac{\left(\nu_0+(1+\nu_0)\gamma^{1+2\nu_0}\right)}{1-\delta} \\ &= \frac{20.5}{\left(1-0.14R_T^{\;0.2}\right)}\frac{1}{R_T^{\;0.8}} \approx \frac{25.5}{R_T^{\;0.8}} \end{aligned} \tag{5.10}$$

The extra factor of $R_T^{\;0.2}$ in the denomitor comes from the δ term that accounts for the fact that the equipotential representing the tip is not at zero voltage. It is easy to see that it has very little effect on the difference $\left(1-0.14R_T^{\;0.2}\right)$. Beta is also slightly weaker in this case than in the FEM simulation (Equation 5-2) because the tip is actually modeled a having a grauduall y increasing radius of curvature, rather than as a section of a sphere.

5.3 IV Characteristics of Double-Gated FEAs (IFE-FEAs)

5.3.1 Device Description

The data for IFE-FEAs is mostly limited by low device yield. Out of six different array sizes (5x5, 10x10, 20x20, 50x50, and 100x100), the only working arrays were a couple of the 5x5s and 10x10s. As shown in **Figure 5-12,** in some of the arrays, the probes are in close proximity to the emitting area, while in others contact pads are connected to the emitters by 5 mm leads. Optical measurements showed that probe proximity strongly distorts the shape of the electron beam; thus, only devices with leads were suitable for measurements of beam collimation. It would be better to take all of the following electrical and optical measurements on 10x10 arrays since we saw that they provide more reliable data due to lower current fluctuations. However, the only working arrays that also had contact leads turned out to be 5x5s. Thus in this section we present data both for a 10x10 array without leads and for 5x5 arrays with leads. The 5x5 array that was used for the optical measurements, presented in Chapter 6, is labeled D64L5_3. (The label reflects position of the device. The die is in row 6, column 4 on the wafer, and the device is the 3rd 5x5 array with leads, counting from the left of the die.) Another 5x5 array with leads that demonstrated markedly different electrical behavior is labeled D63L5_5. The 10x10 array is labeled D43NL10_2 ('NL' stands for 'no leads.') Since the tips in all arrays are 10 microns apart, the 10x10 array has the emitting area of 90x90 μm, and the 5x5s have emitting areas of 40x40 μm.

Top and side view micrographs of a typical IFE-FEA are shown in **Figure 5-13**. Gate and focus diameters are seen to be 867 nm and 1240 nm respectively. Based on the parameters of the fabrication process, we assume for the purposes of analytical modeling that the gate opening is coplanar with the tip apex, and the bottom plane of the focus opening is 300 nm above the top plane of the gate opening.

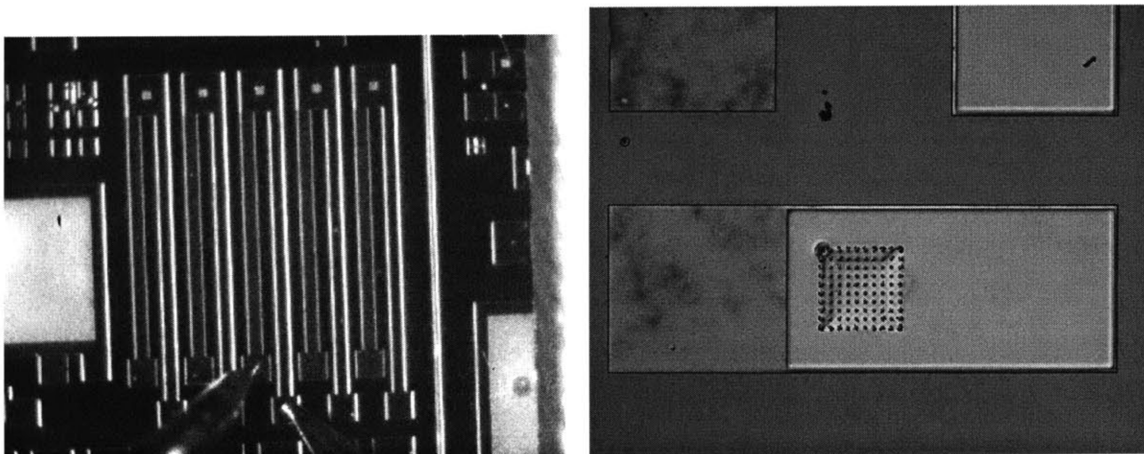

Figure 5-12. (A) A 5x5 IFE-FEA with leads, showing probes on the contact pads (D64L5_3). (B) A 10x10 IFE-FEA without leads (D43NL10_2)

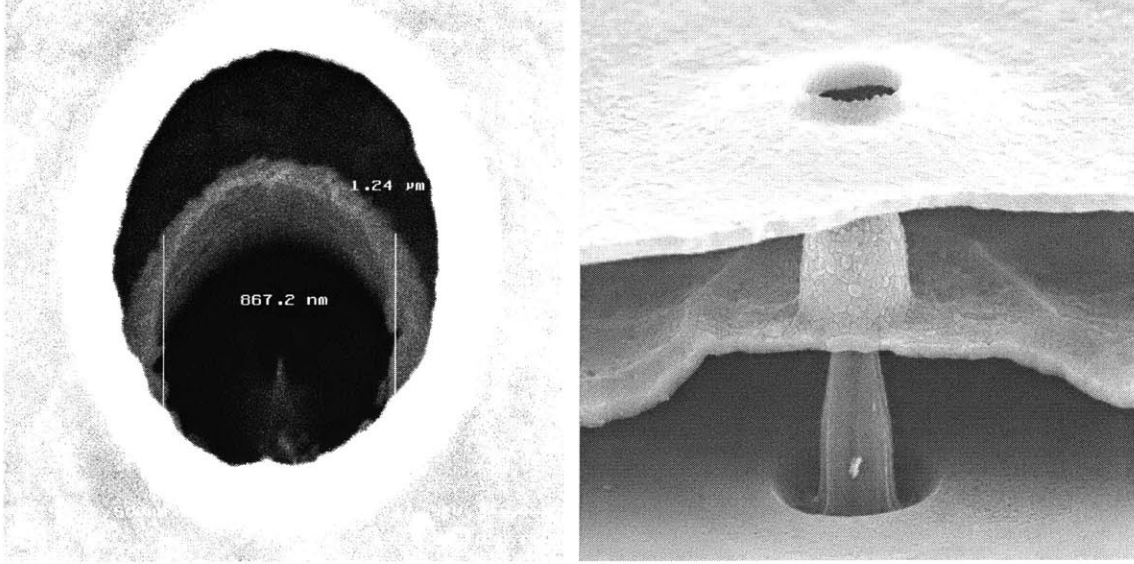

Figure 5-13. (A) Top and (B) cross-section views of IFE-FEA.

5.3.2 Three-Terminal Measurements

It was shown in Chapter 3 that the general IV equation for an IFE-FEA is:

$$I(V_G, V_F) = \alpha \times \left(4.27\times10^{-5}\right)\times\left(\beta_G V_G + \beta_F V_F\right)^2 \exp\left[\frac{-55}{\beta_G V_G + \beta_F V_F}\right] \tag{5.11}$$

$\beta_G, \beta_F \; in \; nm^{-1}$

In three-terminal measurements, where focus voltage is always equal to gate voltage, equation **(5.11)** simplifies to:

$$I(V_G, V_F) = \alpha \times \left(4.27\times10^{-5}\right)\times \beta_{TOT}^2 V^2 \exp\left[\frac{-55}{\beta_{TOT} V}\right] \tag{5.12}$$

$\beta_{TOT} = \beta_G + \beta_F$

So the FN plot is expected to be a straight line just as in the case of single-gate emitters:

$$Log\left[\frac{I}{V^2}\right] = a_{FN} + \frac{b_{FN}}{V} \tag{5.13}$$

$$b_{FN} = \frac{-55}{\beta_{TOT}}; \quad a_{FN} = Log\left[\alpha \times \left(4.27\times10^{-5}\right)\times \beta_{TOT}^2\right]$$

This behavior was indeed observed in every sample measured, as shown in **Figure 5-14** – **Figure 5-16**. In an ideal emitter the field emission current would be equal to the current at the emitter terminal, which in turn equals the current at the anode terminal, and the gate and focus electrodes would collect zero current. In our devices, the focus current, shown with the (▲) symbol in the figures, is approximately equal to the anode current, denoted by (●). Moreover, the FN slopes of focus and anode currents are seen to be virtually identical, which implies that they are both products of the same emission current. In other words, about 50% of the emission current is intercepted by the focus. For the data in **Figure 5-14** and **Figure 5-16**, where the gate current is negligible, the total emission current can be taken as the emitter current, denoted by (■). However, in the data in **Figure 5-15**, the gate leakage current far exceeds that emission current, so that the emitter current is approximately equal to the gate current. In that case, it is necessary to explicitly add the focus and anode currents to obtain the total emission current, denoted by (◇). The FN parameters are quite uniform for different devices, with b_{FN} between –425 and -515 and a_{FN} between –12 and –13.

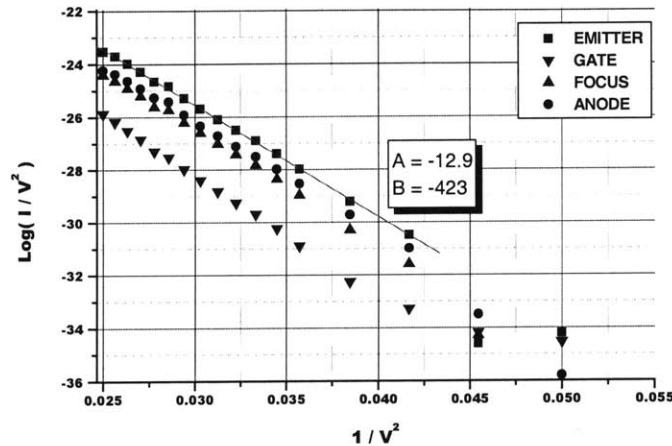

Figure 5-14. FN plots of the Emitter, Gate, Focus and Anode currents per tip vs. Voltage (V_G=V_F) for a 10x10 FEA, D43NL10_2

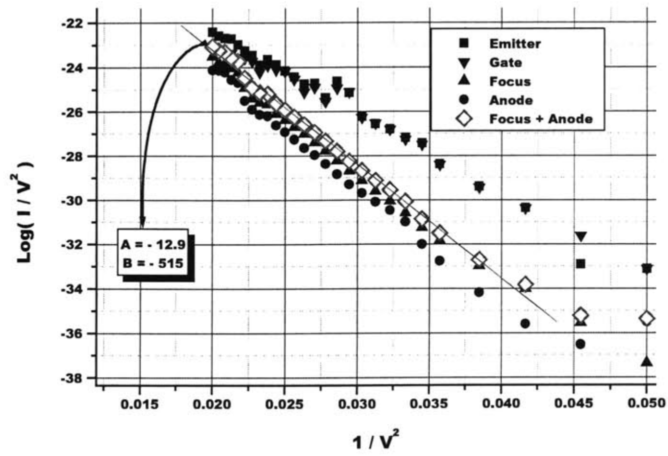

Figure 5-15. FN plots of the Emitter, Gate, Focus and Anode currents per tip vs. Voltage (V_G=V_F) for a 5x5 FEA, D64L5_3.

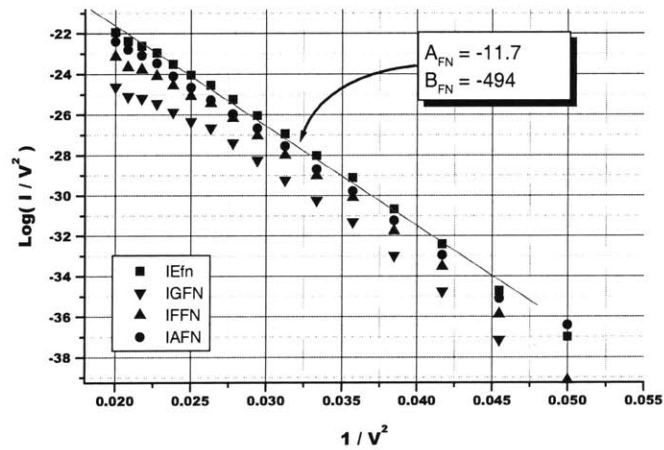

Figure 5-16. FN plots of the Emitter, Gate, Focus and Anode currents per tip vs. Voltage (V_G=V_F) for a 5x5 FEA, D63L5_5

It is interesting to compare the performance of the IFE-FEA in the triode mode (V_G=V_F) with that of the single gate FEA. As derived in chapter 3, the effective field factor of the IFE-FEA in the triode mode, β_{TOT}, and its ratio to the single-gate field factor are given by:

$$\beta_{TOT} = \beta_G + \beta_F = \frac{P_{0.2}(\mu_F)}{P_{0.2}(\mu_G)} \times \left(C'_{21} + \omega^{0.2} C'_{22}\right) + \left(C'_{11} + \omega^{0.2} C'_{12}\right)$$
$$\frac{\beta_{TOT}}{\beta_{Single-Gate}} = \frac{P_{0.2}(\mu_F)/P_{0.2}(\mu_G) \times \left(C'_{21} + \omega^{0.2} C'_{22}\right) + \left(C'_{11} + \omega^{0.2} C'_{12}\right)}{C_{Single-Gate}} \quad \textbf{(5.14)}$$

Following the procedure outlined in chapter 3, we can compute the values of the capacitance coefficients for the device parameters measured from the SEM micrographs of IFE-FEAs, shown in **Figure 5-13:**

$$\begin{aligned}
&\textit{With a Double Gate}: \\
&\textit{Gate radius}: R_G = 400\,nm; \quad \cos\ \textit{of gate angle}: \ \mu_G = 0; \\
&\textit{Focus radius}: R_F = \sqrt{600^2 + 300^2} = 670\,nm; \\
&\cos\ \textit{of focus angle}: \mu_F = 300/670 = 0.44; \\
&\omega = \frac{R_G}{R_F} = 0.6 \\
&C_{11} = 0.63; \quad C_{12} = -0.14; \quad C_{21} = -0.23; \quad C_{22} = 0.55
\end{aligned} \quad \textbf{(5.15)}$$

$$\textit{With a Single Gate} \quad R_G = 400\,nm, \quad \mu_G = 0: \quad C_G = 0.56$$

Thus, the ratio of the field factors becomes:

$$\frac{\beta_{TOT}}{\beta_{Single-Gate}} \approx 1.3 \qquad (5.16)$$

In other words, *assuming* identical tips in the single-gate (SG) FEA and IFE-FEA, the latter has a slightly higher field factor in triode mode. Since IFE-FEA samples are extremely brittle, it was not possible to cleave the wafer and examine the tips under a TEM, as was done for single-gate devices, without damaging the tips. However, we observe that the measured β_{TOT} for IFE-FEA is indeed slightly larger than the field factor in SG-FEA. The FN slope for IFE-FEA is between –425 and –515, whereas the FN slope for SG-FEA is about -500. This suggests that the tips in the SG-FEA and IFE-FEA are indeed very similar. Since the SG-FEA and IFE-FEA wafers underwent identical processing, this comes as no surprise.

5.3.3 Four-Terminal Measurements

In typical IFE-FEA operation, the gate voltage is kept high, while the focus bias is lowered to collimate the beam. An undesirable side effect of this is a drop in the emission current, which in turn can be eliminated by raising gate voltage. The influence of the gate and focus electrodes on the emission current are quantified by the gate and focus field factors, β_G and β_F, in **Equation (5.11)**. Our goal in this section will be to extract their values from the four-terminal IV data. In four-terminal IV measurements, one of the electrodes is kept at a constant bias, while the other is swept through the operating range. **Figure 5-17 – Figure 5-19** show the resulting values of the anode

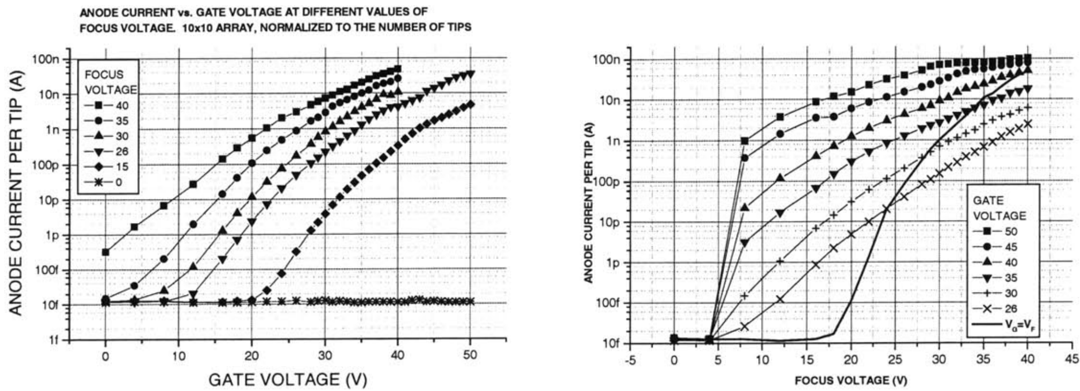

Figure 5-17. Four-terminal IV data for a 10x10 IFE-FEA (D43NL10_2). Left: I_A vs. V_G at fixed V_F; Right: I_A vs. V_F at fixed V_G.

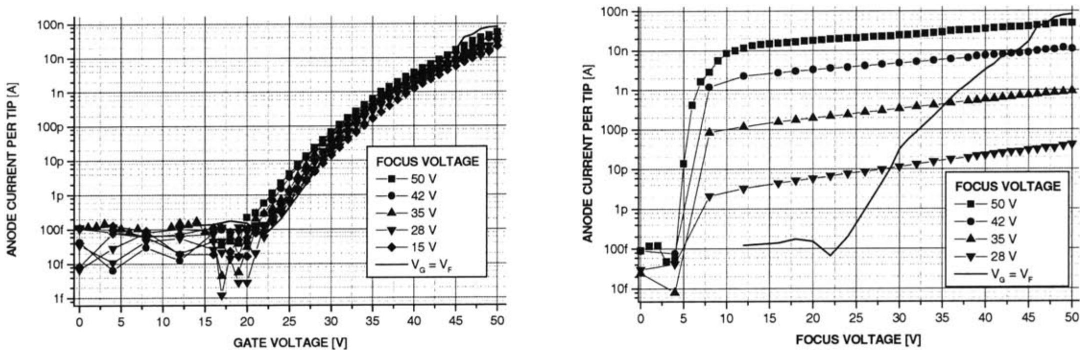

Figure 5-18. Four-terminal IV data for a 5x5 IFE-FEA (D64L5_3). Left: I_A vs. V_G at fixed V_F; Right: I_A vs. V_F at fixed V_G

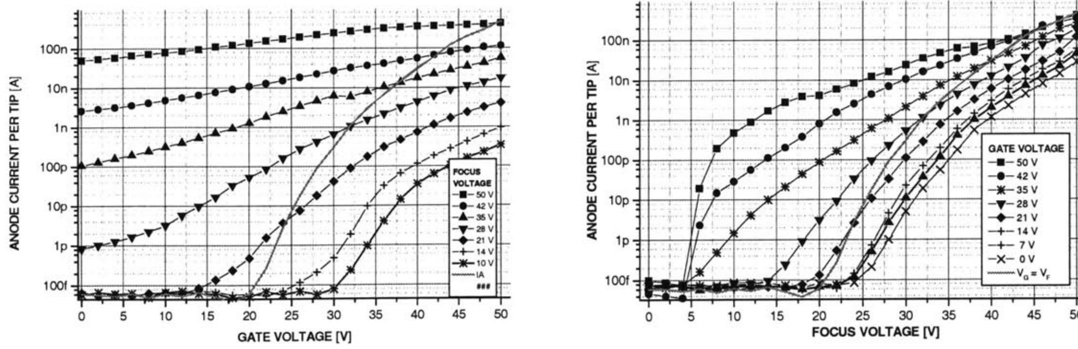

Figure 5-19. Four-terminal IV data for a 5x5 IFE-FEA (D63L5_5). Left: I_A vs. V_G at fixed V_F; Right: I_A vs. V_F at fixed V_G

current. The left half of each figure shows the variation of the anode current with gate voltage at fixed values of the focus voltage; the right half shows the variation as a function of focus voltage with the gate voltage being fixed. Complete plots of current values at all four electrodes are given in Appendix II.

Even before fitting the data, we can notice that the relative magnitudes of β_G and β_F differ considerably between devices. In D64L5_3, the anode current is only weakly dependent on focus voltage; in D63L5_5 the focus has a stronger effect on the current than the gate; and in D43NL10_2 the two appear approximately equal.

To quantify this effect, we compute the total emission current by adding anode and focus currents as described above, then combine all the different $I(V_G)\big|_{V_F}$ and $I(V_F)\big|_{V_G}$ sweeps for each device into a single data set $I(V_G, V_F)$, and perform a least squares fit to equation **(5.11)**. The results of this procedure are shown in **Figure 5-20—Figure 5-22.** We observe that the fit in **Figure 5-20** is quite good, while the fits in **Figure 5-21 – Figure 5-22** are markedly less so. Since equation **(5.11)** is a direct consequence of fundamental electrostatics, there is no question of its being invalid. Instead, the problem lies in the amount of noise contained in the dataset. In section 5.2, Figure 5-3, we saw how much current fluctuation is exhibited by a typical 5x5 array. We also saw that emission from a 10x10 array is considerably more stable (**Figure 5-4**). It is this factor that is responsible for how well the equation fits the data. Effectively, emission from 5x5 arrays is controlled by a generalized form of Equation **(5.11)**:

$$I(V_G, V_F) = a_J\left(\phi[t]\right) \times \left(\beta_G V_G + \beta_F V_F\right)^2 \exp\left[\frac{b_J\left(\phi[t]\right)}{\beta_G V_G + \beta_F V_F}\right] \qquad \textbf{(5.17)}$$

where the value of the workfunction ϕ fluctuates randomly with time. Thus, the different sweeps that we combined into a single dataset and fit to Equation **(5.11)** are in fact produced by different values of the workfunction and should be fit to Equation **(5.17)**. Of course, this is impossible since the variation of the workfunction with time was not, and probably could not, be recorded.

However, it turns out that excluding various data sweeps from the full data set only changes the gate and focus field factors by about 20% (incidentally, the errors in the estimates of field factors are about 2%, i.e. $\sigma_\beta / \beta \approx 0.02$). The *ratio* of the field factors, β_F / β_G, is even more stable with respect to data selection and thus can be viewed as a fairly reliable estimate. On the other hand, the "area factor" α is a very poor estimate, both as measured by its uncertainty, which is in the 20%-100% range, and its degree of variation as a function of data selection. **Table 5-1** summarizes these parameter estimates.

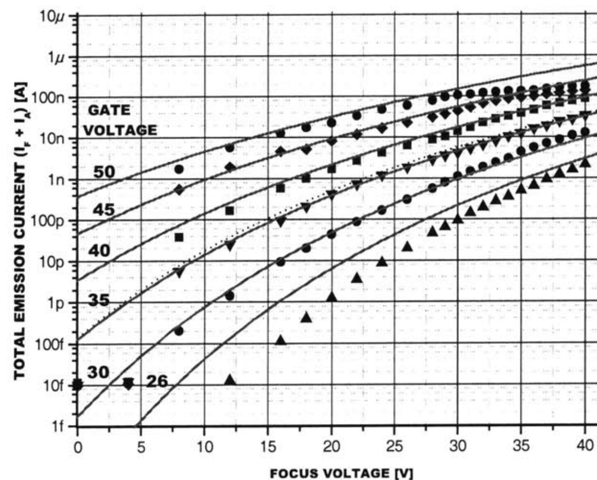

Figure 5-20. D43NL10_2: Emission current vs. focus voltage at fixed gate voltage, with the least squares fit lines based on Equation (5.11). Data from the 10x10 FEA is more stable and is thus in better agreement with the model.

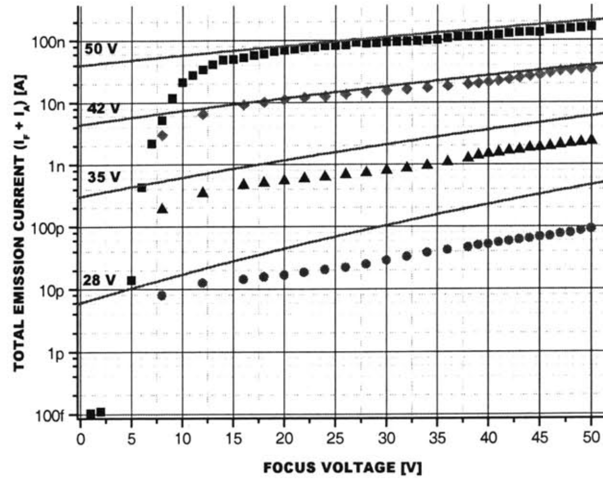

Figure 5-21. D64L5_3: Emission current vs. focus voltage at fixed gate voltage , with the least squares fit lines based on Equation (5.11). Data from the 10x10 FEA is more stable and is thus in better agreement with the model.

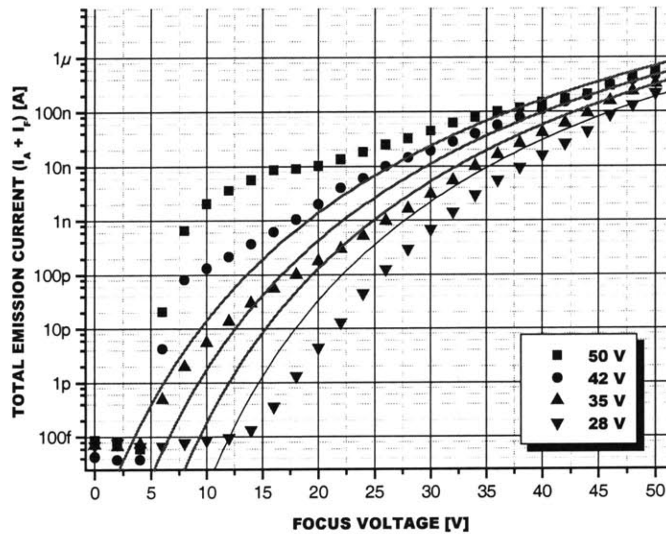

Figure 5-22. D63L5_5: Emission current vs. focus voltage at fixed gate voltage , with the least squares fit lines based on Equation (5.11). Data from the 10x10 FEA is more stable and is thus in better agreement with the model.

Table 5-1. Summary of area factors and gate and focus field factors for different IFE-FEAs, and comparison with the FN data for a single gate device.

*** Values for α are only rough estimates**

	4-TERMINAL DATA				3-TERMINAL DATA		
DEVICE	β_G [nm^{-1}]	β_F [nm^{-1}]	α* [nm^2]	$\frac{\beta_F}{\beta_G}$	A_{FN}	α	$\beta_{TOT} = \frac{-55}{B_{FN}}$
Single Gate 10x10	*N/A*	*N/A*	*N/A*	*N/A*	*-8.1*	*657*	*0.104*
D43NL10_2	*0.065*	*0.049*	*18.5**	*0.75*	*-12.9*	*3.46**	*0.130*
D64L5_3	*0.113*	*0.018*	*0.5**	*0.16*	*-12.9*	*5.11**	*0.107*
D63L5_5	*0.046*	*0.123*	*0.1**	*2.67*	*-11.7*	*15.76**	*0.111*
Bowling Pin Model				*0.56*			*0.13*

An approximation to the ratio of the gate and focus field factors, according to the equation derived in Chapter 3, is given by:

$$\frac{\beta_F}{\beta_G} = \frac{P_{0.2}(\mu_F)}{P_{0.2}(\mu_G)} \times \frac{\left(C'_{21} + \omega^{0.2} C'_{22}\right)}{\left(C'_{11} + \omega^{0.2} C'_{12}\right)} \cong 0.56 \qquad \textbf{(5.18)}$$

The data from a 10x10 array (D43NL10_2) is in fair agreement with the model and confirms what we would expect intuitively for the assumed device geometry, namely that the effect of the focus is somewhat less than the effect of the gate. However, as we already observed, data from D64L5_3 and D63L5_5 show anomalously small in case of the former or anomalously large in the case of the latter values of the focus field factor.
It was observed that the relative magnitude of the gate and focus field factors was correlated with the position of the device within the die. This suggests that it results from non-uniformities in the fabrication process.

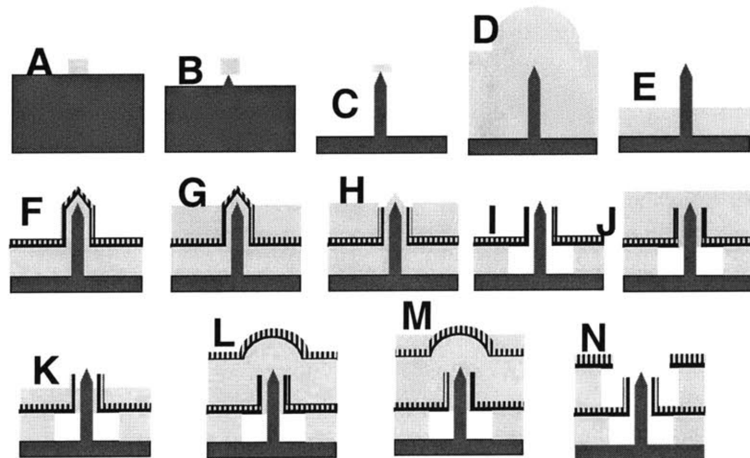

Figure 5-23. Fabrication process used in making IFE-FEAs (repeated from Chapter 4.)

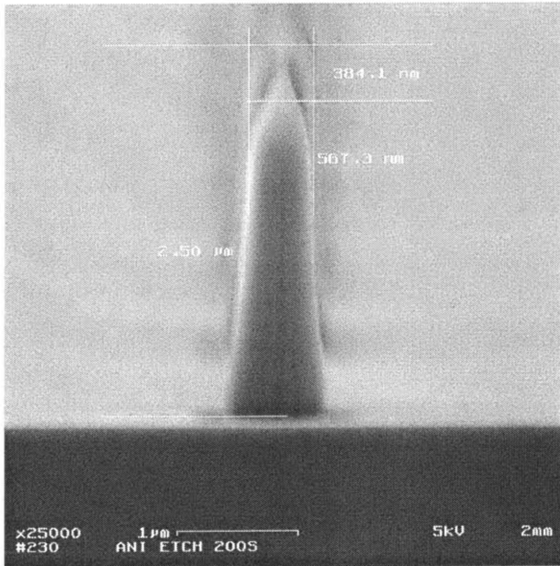

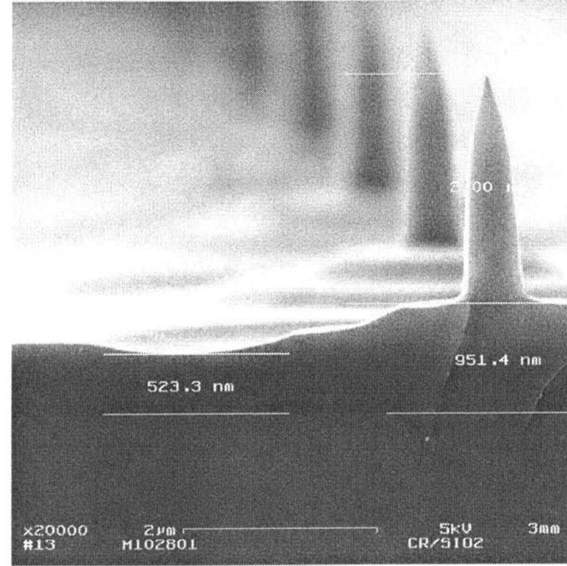

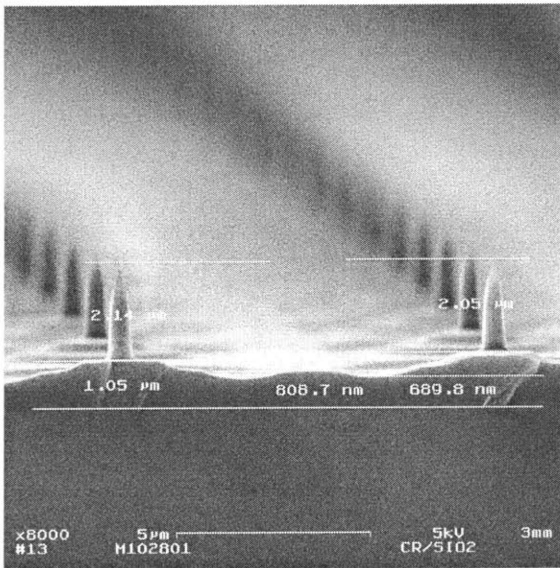

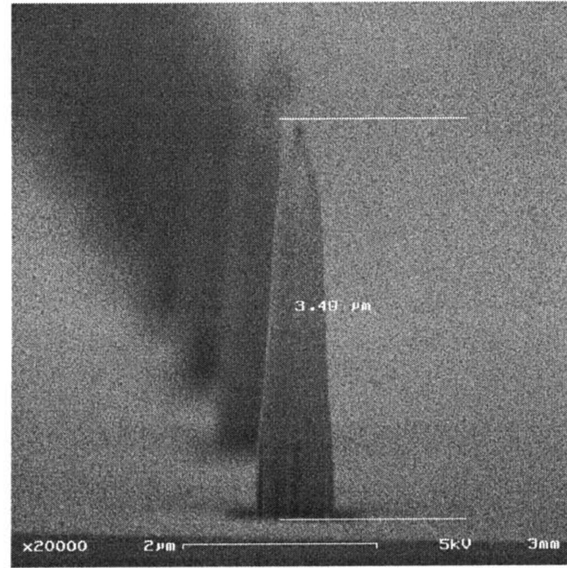

Figure 5-24. SEM micrograph show that the height of silicon tips formed in step C varies between 2.5 and 3.5 microns.

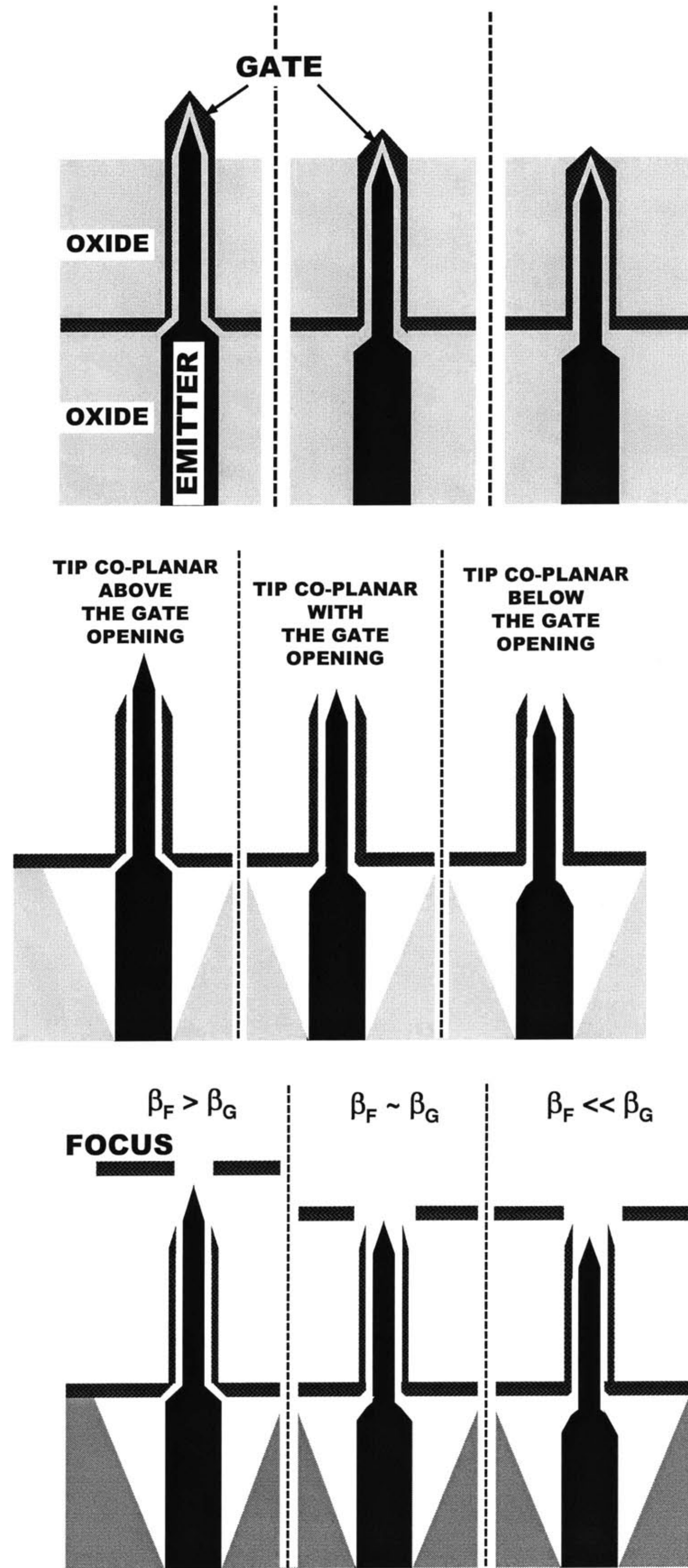

Figure 5-25. Differences in tip height translate into differences in the gate and focus field factors.

Figure 5-24 shows the fabrication process used to make these devices. It was described in detail in chapter 4. The figure also indicates that the height of high aspect ratio tips formed in step C of the process varies considerably – the shortest tips are 2.5 μm and the tallest tips are 3.5 μm. These SEMs were from arrays of tips in different locations within the die. Then, in **Figure 5-25** we see how differences in tip height translate into differences in the relative positions of the tip and the gate. Since CMP makes all gate opening lie in the same plane, shorter tips end up below their gate openings and shielded from the effect of the focus, which thus has a small field factor. Conversely, taller tips end up above their gate openings, and in fact closer to the focus electrode, which thus has a larger field factor than the gate.

To quantify this effect, we built models of these geometries in Matlab (courtesy of Guobin Sha), as shown in **Figure 5-26**. Gate radius and cone structure were the same as in the single gate simulation presented in the previous section. The height difference between the shorter tip, which was placed 200 nm below the plane of the gate, and the taller tip, which was 200 nm above the plane of the gate, was 400 nm. SEMs in **Figure 5-24** show that differences in tip height may in fact be as large as 1000 nm, so our value of 400 nm is by all means a conservative estimate. Using data from **Figure 5-13**, the focus opening was taken to be 600 nm in radius and positioned 300 nm (measured from the lower edge) above tip when the tip is in the plane of the gate opening (**Figure 5-26B**) or below the plane of the gate opening (**Figure 5-26C**).

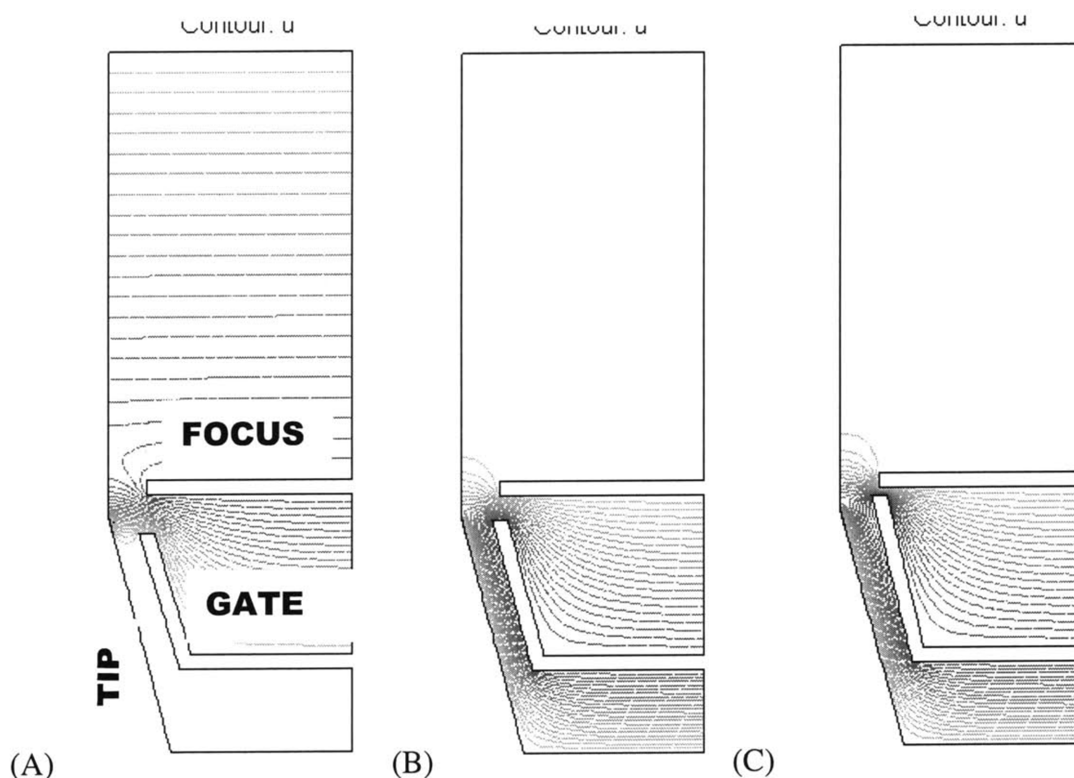

Figure 5-26. (A) Tall tip protrudes 200 nm above the gate; focus radius 500 nm, 300 nm above the tip (B) Average tip is coplanar with the gate; focus radius 600 nm; 300 nm above the tip (C) short tip is 200 nm below the gate and shieled from the focus. Focus radius 600 nm; 300 above the gate. Gate radius and other parameters as in Figure 5-10.

When the tip is protruding from the gate opening, the focus was taken to be 100 nm lower and 100 nm smaller in radius because in this case conformal oxide coating covers a smaller top – only the tip is at the top, instead of the opening of the gate aperture – and thus the outer oxide surface ends up closer to the tip. Hence, the final tip-to-focus spacing is expected to be smaller. With these assumptions we obtained fair – and in the case of the shielded structure (tip below the gate) excellent – agreement between the measured and calculated ratios of the gate and focus field factors, as shown in **Table 5-2**.

Table 5-2. Results of Matlab simulations show qualitative agreement with the measurements.

4-Terminal Data				Matlab Simulations			
DEVICE	β_G [nm^{-1}]	β_F [nm^{-1}]	$\frac{\beta_F}{\beta_G}$	Tip Position in relation to gate	β_G [nm^{-1}]	β_F [nm^{-1}]	$\frac{\beta_F}{\beta_G}$
D43NL10_2	*0.065*	*0.049*	*0.75*	*In-plane*	*0.107*	*0.043*	*0.4* *BPM: 0.56*
D64L5_3	*0.113*	*0.018*	*0.16*	*Below*	*0.129*	*0.02*	*0.15*
D63L5_5	*0.046*	*0.123*	*2.67*	*Above*	*0.054*	*0.091*	*1.7*

One *systematic* feature that is not explained by superposition is the anomalous drop in the emission current at focus voltages below 10 V. This phenomenon, excluded from the data fit to **Equation (5.11)**, is the subject of the next section.

5.3.4 Investigation of Space Charge at Focus Voltages below 10 V

Despite the differences in the response of emission current to changes in focus bias, evident in **Figure 5-20 –Figure 5-22**, one feature remains constant: an abrupt drop when V_F is reduced below ~ 10 V. This effect results from lowering the focus bias only; the gate bias can be reduced to 0 V while still getting non-zero emission current, as **Figure 5-22** illustrates. This fact, as well as the discrepancies between model and data in the range V_F<10 V in make it clear that we are observing a phenomenon that is not described by the generalized FN IV equation (5.11).

Figure 5-27 shows a close up of the data at V_F<10V.

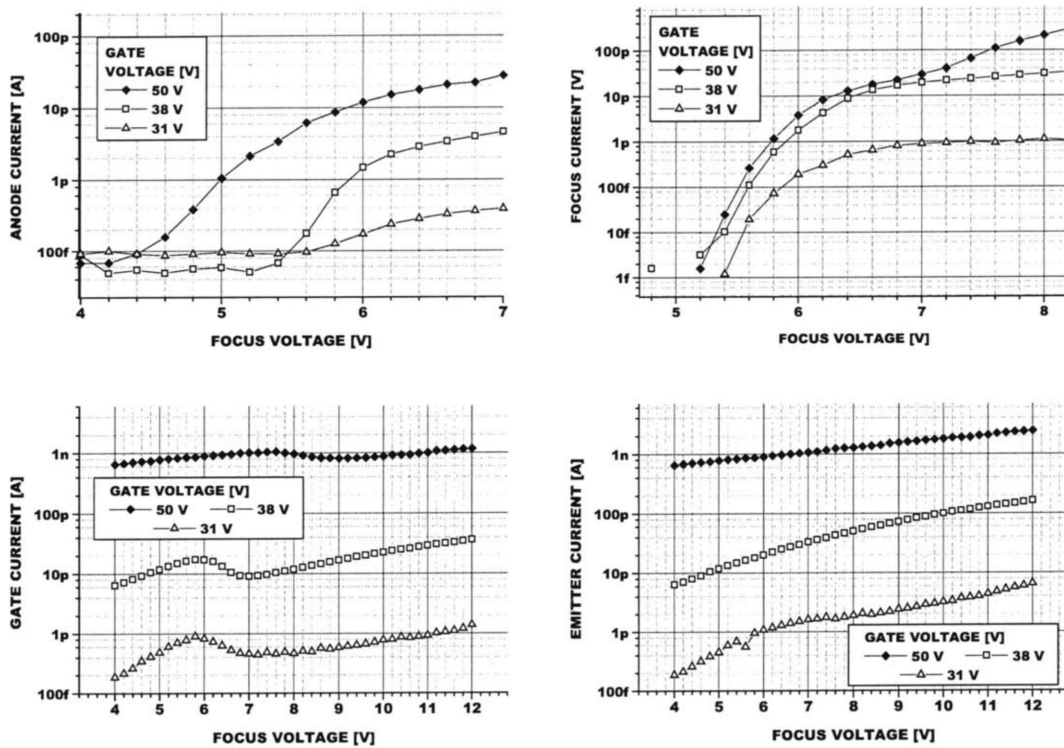

Figure 5-27. Anode, focus, gate and emitter currents as a function of focus voltage for different values of gate voltage in the region of space charge (V_{ANODE} = 1000 V). (D63L5_5)

J. Itoh, who first observed this effect in his devices, wrote [98]:

"In the region V_F<10 V, on the other hand, I_A shows a quite different V_F dependence and abruptly decreases down to a few nanoamperes. In such conditions, electrons are not repelled as shown in Fig. 2c [i.e. back to the tip or back to the gate—LD] because V_F is still positive. A possible explanation is space charge effect caused by the retardation effect of the upper gate. In order to clarify the cause of the present I_A behavior, however, it is necessary to measure all the currents (I_E, I_G, and I_A) carefully as a function of V_F. Especially, the dependence of I_A on V_A is essentially important for consideration of space-charge effect."

Observe that although Itoh's devices had larger aperture radii (R_G=1 μm, R_F=1.5 μm, with the gate coplanar with the tip and the focus 1 μm above the tip) and higher gate voltage (V_G=80 V), current suppression still occurred in the same region, $V_F<10$ *V*. Note also that in Itoh's devices this effect was not as pronounced: the array current was decreased down to a few nA, while in our devices the emission current went to zero in every case. Another relevant detail is that in our devices over 50% of the emission current is intercepted by the focus, whereas in Itoh's devices this figure is <5%.

Another piece to this puzzle comes from devices in which the focus is coplanar with the tip [99]. This effect is *not* present there. In fact, in that case optimal focusing is achieved when $V_F < -10V$, at which point the total emission current is unaffected, but a fraction of the electron beam is repelled back by the focus field and collected by the gate.

In our setup the electrons cannot be repelled back to the cathode by a positively biased focus electrode. Since there is no resistor between the emitter and ground, the emitter surface is at 0V and electron trajectories start with zero energy. When all the other electrodes are biased above zero, the potential is positive throughout all space. Therefore, there are no potential barriers high enough to turn back electron trajectories.

The hypothesis that the focus retardation effect causes space charge that suppresses the emission field is, in our view, also inadequate, simply because the current is so low. Let's quantify this. Suppose all current is emitted from the apex, one electron at a time, and at regular intervals [100]. A current of 10 nA (per tip) then corresponds to an electron being emitted every 16 ps. The field that an electron at position z above the apex induces at the apex is given by[100] $\alpha_{fs}\hbar c/z^2$, where α_{fs} is the fine structure constant equal to (1/137). According to this equation, an electron that is 3.7 nm above the emitter surface induces the field of 0.1 V/nm at the apex. Practically, the electron needs to be within 10 nm of the tip to have an effect on the emission density [100]. However, according to our trajectory calculations, it takes an electron less than 1 ps to move more than one micron away from the tip (This corresponds to the average velocity of 10^6 m/s). Thus, the emission current is seen to be a few orders of magnitude too low to produce the space charge effect by this mechanism.

We may arrive at the explanation for this effect by examining what happens to the anode current as the *anode voltage* is reduced to zero. As V_A is reduced below V_F, an increasingly greater fraction of the emission current is intercepted by the focus electrode and the anode current gradually drops, as shown in **Figure 5-28.** However, when V_A becomes less then the workfunction of anode material (5.6 V in Figure 5-28 A), the anode current abruptly goes to zero because electrons have insufficient potential energy to overcome the potential barrier at the anode surface. When this happens, the electrons get pulled back and collected by the focus electrode.

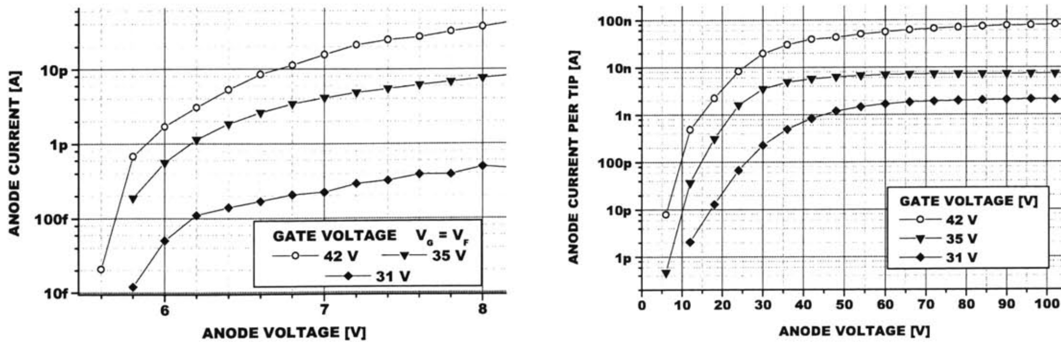

Figure 5-28. Anode current as a function of anode voltage (A) in the range 5-8 V (B) in the range 0-105V. The anode current goes to zero when V_A is becomes less than the workfunction of anode material (D63L5_5).

But what happens when the bias on the *focus electrode* is below its workfunction so that the electron impinging on its surface cannot be collected? The electron loses its velocity and is then accelerated by the focus field back to the cathode effectively retracing its trajectory but with a slight shift towards the gate. Of course, the electron also does not have sufficient energy to be collected back by the cathode, and thus ends up oscillating between the focus and the cathode gradually moving closer to the gate until eventually it is absorbed there. However, in the course of oscillation, the electron comes very close to the tip and suppresses the emission field, thus significantly reducing the emission current. **Figure 5-29** presents an example of such oscillating trajectory; for clarity, the figure shows only one and a half iterations.

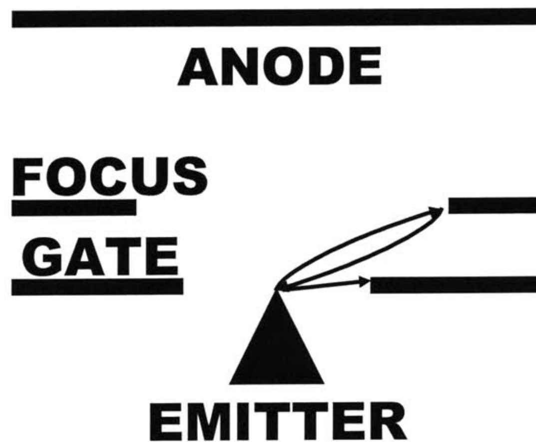

Figure 5-29. When focus voltage is less than the workfunction of the focus material, some electrons oscillate between the tip and the focus and eventually get collected by the gate. When they approach the tip, electrons reduce the electric field on the surface and thus suppress the emission current.

5.4 Chapter Summary

This chapter discussed the IV characteristics of IFE-FEA.

After describing the measurement setup, we began by analyzing IV data from single-gate emitters whose gate geometry and tip sharpness are very similar to those of IFE-FEAs. These devices had turn-on voltages of 16-18 V (**Figure 5-3**), though we argued that the turn-on voltage is not a precise metric since it depends on the array size and the noise floor of the particular measurement system. To get a unique value, it was proposed to define the turn-on voltage as the one at which the emission current per tip is equal to 1 fA, which is equivalent to the total current of 10 pA in a 100x100 array – a figure that is just above the noise floor in our measurement setup.

In Section 2, the IV data from arrays of single gate emitters was used to calculate the FN coefficients A_{FN} and B_{FN}. We looked at arrays of different sizes: 1x1, 5x5, 10x10, 25x25, and 50x50. To insure accurate measurements, IV sweeps on each array were repeated 20 times confirming the hypothesis that random fluctuations in emission current, due to adsorption and desorption of foreign particles on emitting surfaces, decrease with array size (**Figure 5-4 – Figure 5-6**). Multiple sweeps also insured against computing the FN parameters based on the data that is not representative of the device. The analysis showed that all of the arrays have very similar values of the FN coefficients, with many differing by only 1-2%: $a_{FN} = -12.6 \pm 0.1$; $b_{FN} = -493 \pm 5$ (**Figure 5-14 – Figure 5-16**). We built a model of the device in Matlab (courtesy of Guobin Sha) and found that for our device geometry, the measured value of b_{FN} correspond to the tip ROC of 3.6 nm. TEM micrographs of the tips showed that that tip ROC is between 2.4 – 3.6 nm, which agrees with the simulations to within one experimental error. We equated the BPM expressions for the FN parameters to the measured values and again extracted the value of tip ROC. The BPM result for tip ROC was 2.7 nm, in agreement with both TEM micrographs and numerical simulations – a triumph!

In Section 3, we progressed to the analysis of four-terminal IV data from IFE-FEAs. We began with 3-terminal measurements, in which the gate and the focus are kept at the same potential. Under these conditions, the FN plot of the IFE-FEA remains linear. We used the FN slope and intercept to conclude that (i) the tip ROC is very similar to that of the single-gate devices and (ii) about 50-60% of the total emission current is intercepted by the focus.

The starting point for the analysis of 4-terminal measurements, in which the gate (focus) electrode is kept at a constant bias while the voltage on the focus (gate) electrode is varied, was the FN IV equation generalized for the case of IFE-FEA (**Equation (5.11)**):

$$I(V_G, V_F) = \alpha J(E_{Apex}) = \alpha \times \left(4.27 \times 10^{-5}\right) \times \left(\beta_G V_G + \beta_F V_F\right)^2 \exp\left[\frac{-55}{\beta_G V_G + \beta_F V_F}\right]$$

β_G, β_F *in* nm^{-1}

Fitting this equation to several IV curves obtained by varying V_F while keeping V_G constant and vice versa (**Figure 5-17 – Figure 5-19**) yielded the values of gate and focus field factors and the area factor. We then calculated the (measured) value of the ratio of

field factors, which is an important characteristic of IFE-FEA. It was discovered that this ratio, β_F/β_G varied widely between devices with the measured values equal to 0.16, 0.76, and 2.67. We demonstrated that this ratio is probably determined by whether the tip is in the plane of the gate opening, below the plane, or above the plane. These differences in turn stem from the original differences in tip height at different points within the die and across the wafer. This hypothesis was verified by simulating the three device structures in Matlab, which produced values of the field factors quite close to those measured. It may be noted that this entire procedure, starting from the generalization of the FN equation to the case of IFE-FEA is an original contribution of the author.

Finally, the anomalous reduction in emission current at low values of the focus bias (V_F < 10 V) was studied. This phenomenon has been reported in the literature but not adequately explained. Following a critique of the existing hypothesis, we presented an alternative mechanism that we believe is responsible for this effect **(Figure 5-27 – Figure 5-29).**

To recap, we have learned the following main points from this chapter:

Single-gate devices:

♦ Noise in the emission current decreases with array size. Arrays of at least 10x10 are needed to get stable current.

♦ The tip radius of curvature was between 2.4 and 3.6 nm according to TEM images, with about 0.5-1 nm uncertainty. Finite element method simulation of the devices done in Matlab (courtesy of Guobin Sha), yield the ROC value of 3.7 nm.

♦ Solution of the closed-form BPM equations for the FN slope and intercept produced the ROC value of 2.7 nm, in excellent agreement with the measurement and with numerical simulations.

Double-gate devices (IFE-FEA):

♦ Tip radius of curvature is similar to that of single gated devices

♦ The focus electrode intercepts 50-60 % of the emission current

♦ The ratio of the gate and focus field factors β_F/β_G is controlled strongly by whether the tip is shielded by the gate. When the tip is shielded by the gate, the emission current is practically independent of the focus voltage – a highly desirable situation.

♦ When focus voltage drops below ~ 10 V, the emission current is completely suppressed. Earlier explanation of this phenomenon, given in the literature, in terms of space charge does not appear to be valid. We proposed an alternative mechanism which

involves electron trajectories oscillating between the focus and the tip. Accurate trajectory calculations are needed to test this hypothesis.

6 Optical Characterization of IFE-FEA

6.1 Measurement Setup for Image Acquisition

This chapter will examine the single most important aspect of IFE-FEA performance – reduction of spot size as a function of focus bias. The spot size effectively determines the minimum pixel size in a field emission display and typically needs to be less than 0.2 mm in diameter.

Figure 6-1 shows a schematic of our experimental setup. While IV characterization of field emitters done in the previous chapter is an established process, and its extension to IFE-FEA was done to some extent in our earlier work [58, 59], spot size measurements bring us into unfamiliar territory. Some of the prior IFE-FEA work sited in Chapter 2 had images showing spot size reduction and gave measurements of spot size. However, to the best of our knowledge, none went into detail of how those images were acquired and processed to obtain those spot size measurements. We will now argue that this problem deserves attention if one wants to make any kind of quantitative pronouncements on spot size.

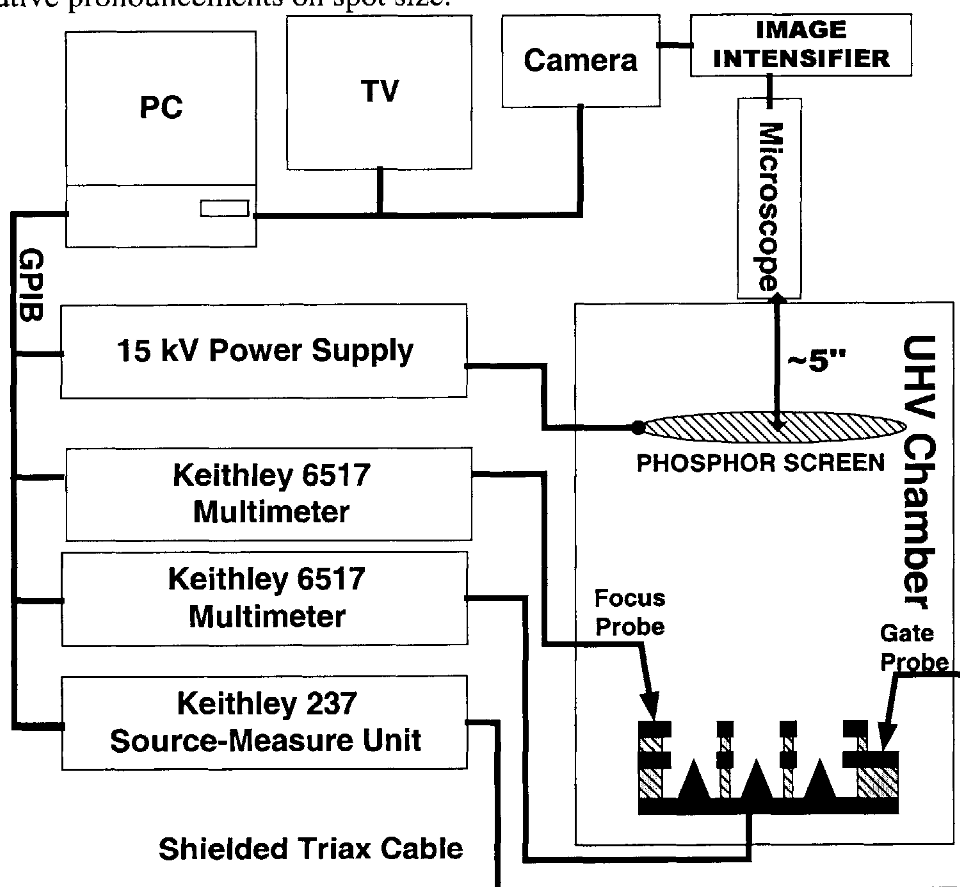

Figure 6-1. Diagram of the measurement setup.

Instrumentation plays an important role in spot size measurements. Since the spot produced on the phosphor anode by the electron beam is rather dim, and the anode in our setup is at least 5'' away from the camera, in the vacuum chamber, we could not obtain good images with a simple high-sensitivity monochrome CCTV (closed-captioned TV) camera. Therefore, an image intensifier (II) [Litton model M942] was inserted in front of the camera, which produced very bright and clear images. However, the image intensifier measurement method posed several problems. One is that it saturated the camera at a wide range of light intensities making it impossible to distinguish between, for example, a large and bright uniform spot and a small, bright spot surrounded by a dim halo. (It may be possible to solve this by placing a neutral density filter between the camera and the image intensifier.)

This effect can also make spot size reduction with decreasing focus bias appear more pronounced than it really is. This is because lower focus bias results in smaller emission current which does not saturate the camera except in the immediate vicinity of the center of the spot. (The spot size is taken to be the diameter of the saturated area.) After we finish the discussion of how images were *acquired*, we will talk in greater detail about *measuring* spot size from these images. Basically, we took the saturated part of the spot to be equal to the spot size because that was the only way to get an unambiguous measurement that would not be affected by light piping and dispersion in the phosphor screen, various aberrations, and other noise. Another problem with image intensifier measurement, is that it is a night vision tool rather than a precise scientific instrument and probably does not amplify the signals from different pixels by exactly the same factor. In summary, the data taken with image intensifier is good to determine trends and general dependencies, but not to extract quantitative results. The image intensifier data will be presented here because we did not have the opportunity to repeat these measurements with the more accurate setup that we will now describe.

It so happened that right around the time we were almost done collecting optical data, another student in the group purchased a scientific digital camera capable of timed exposure. Although the camera was intended for a different application, it proved to be an excellent tool for spot size measurements. Most images were taken with the exposure of 1 second, and then further contrast enhanced in Adobe Photoshop to insure legible reproduction.

The important point is that, as illustrated in **Figure 6-2**, the result of the spot size measurement is dependent on how the image was acquired and/or processed.

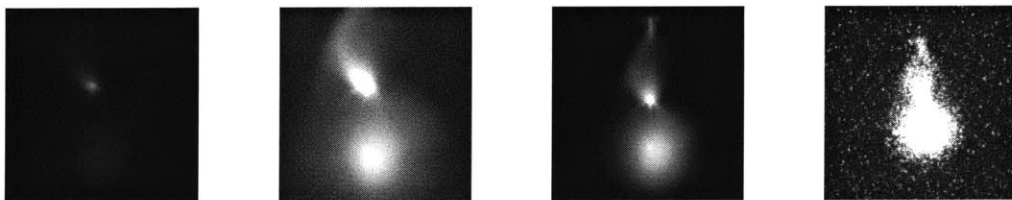

Figure 6-2. Dependence of spot size on the measurement method. Spot produced on the phosphor anode with V_G=50 V; V_F=7V; I_A≈30 nA; V_A=8KV; d_A=10mm. Left to right: original spot photo taken with a digital camera and 1sec expo; same photo with contrast and brightness adjusted; spot photo with 5 sec exposure; spot photo with a standard monochrome camera and image intensifier. (The image intensifier photo may be from a different 5x5 device). [The smaller spot, or 'tail', on top is due to an emitter on the upper boundary of the array whose focus electrode was damaged during CMP, as shown in Figure 5-2A and 5-12B.)

This fact has implications for making meaningful comparisons between published values of collimated spot size and the resultant beam current density. Ignoring noise issues, the most accurate spot size measurement, in the absence of a charge counter, is achieved by a timed exposure with a low-noise digital camera and subsequent numerical analysis of the grayscale image. It is also necessary to account for brightness/contrast adjustment done by the camera and for light loss and scattering between the phosphor screen and camera CCD. Moreover, most spots we observed had rather jagged edges since there were only 25 tips in our arrays, and not all of them were operating. For display applications it would be better to have larger arrays, 10x10 or 20x20, which can be expected to produce uniform spots of well-defined size. In the absence of all these conditions, the spot size data that we present was obtained by simply measuring the diameter of the brightest, inner part of the image, ignoring any halos and aberrations. Thus, we will be careful to draw only limited inferences from our results.

A measurement of current density on the screen is potentially even more useful than that of spot size alone. Although all of the optical data presented in this chapter was collected with device D64L5_3, whose IV characteristics were described in detail in the previous chapter, this is insufficient to obtain anything but rough estimates of current density values. While leakage current resulting from field emission by the probes can be measured and subtracted, it is impossible to know what fraction of the current is actually responsible for the spot being measured, and what fraction is contained in the "halos" around the main image. Basically, the image produced by a 5x5 array in which only 10-15 – and possibly fewer – tips are probably emitting is simply not uniform enough to provide reliable measurements of current density. We will come back to this point at the end of the section. Another relevant factor that will be addressed at that time is phosphor response.

To answer another potential question, there will be no comparison of the data to trajectory calculations. While trajectory calculations done with the BPM do a nice job of illustrating the collimation effect, there is not certainty that they are quantitatively correct. The approximation at the heart of the model – that a plane with a circular opening is equivalent to a charged ring – is reasonable inside the opening; however, when trajectories are traced above the plane, the field becomes different from that of a charged ring. Qualitatively, if the fields at the center of the ring and at the center of the opening in the plane are set equal, and then plotted along the vertical axis, the field of the ring is seen to rise faster and higher and then drop off faster. This is to be expected since all the charge on the ring is concentrated at one radius. It may be that the net effect on trajectories is the same in both cases, or at least the same to within experimental resolution; however, to be certain one needs to do accurate numerical calculation of trajectories. To these the BPM would provide a useful independent check. Also, trajectory calculations with BPM are by themselves complicated and time consuming. While the BPM produced closed-form expressions for the FN coefficients, it was not possible to obtain any closed form (i.e. z-x form) solutions for trajectories. All these circumstances make application of the BPM to trajectory calculations less worthwhile.

The right approach would be to build a model of our device using a much better FEA simulation tool developed by another student in the group [101]. However, building device models and doing trajectory calculation with that application is quite involved and cannot be incorporated into this work because of time constraints. When it *is* done, it

may also be worthwhile to re-evaluate our image data using numerical analysis of Tiff files. Ultimately, this may become the first demonstration of quantitative agreement between spot size data and modeling.

6.2 Collimation of the Electron Beam at Different Values of Gate Voltage

In this section we examine the variation of spot size with focus voltage at different values of the gate voltage. In the data shown in **Figure 6-3** and summarized in **Figure 6-4**, we observe four different trends, none of which rely on the absolute values of spot size measurements. First, the decrease in spot size starts out slow at higher values of V_F. For example, V_G=50V data shows no change in spot size for voltages above 30V. This is in qualitative agreement with J. Itoh's data, in which the gate was held at 80 V and spot size showed significant change only when the focus bias was reduced below 30 V. In the range of negative focus charge, there is the point of optimal beam collimation, i.e. the best value of V_F. For gate voltages of 50, 42 and 35V, the best V_F are respectively ~12, 10 and 8 V. A numerical study suggested that in fact, the *ratio* of the gate and focus voltages is what determines the spot size and that the optimal ratio was V_F/V_G=0.35, though electode radii were larger in that simulation [[101]]. Our data shows the "optimal ratio" to be approximately 0.24 , but with only three data points, it would be premature to claim that we have even proven the existence of the 'optimal ratio.'

On the other hand it is easy to explain qualitatively why lower gate voltage leads to a lower value of optimal focus bias. The optimal beam collimation is achieved with a certain amount of negative charge on the focus, and the focus acquires this negative charge due to the proximity of the positively biased gate. Thus, when the gate is less positively biased, the focus voltage needs to be lowered to obtain the same negative charge. An opposing effect is that when the gate voltage is lowered, there is a smaller positive charge on the gate and the beam is thus subjected to a weaker divergent field. However, this is less important since beam divergence is in large part due to the electrons being emitted at non-zero angles.

When the focus bias is reduced below the point of optimal collimation, the electron beam begins to diverge again. Now the electron trajectories are being overfocused, meaning they cross the optical axis. This is also predicted by simulations[101]. Finally, as we get into the space charge region, discussed in the previous chapter, the spot abruptly disappears at V_F=5V.

Note that we have not stated that higher gate voltage per se produces greater spot size, as could be concluded from **Figure 6-4.** Otherwise, the fact that spot size for $V_G=V_F$=50V is greater than the spot size for $V_G=V_F$=35V would conclusively disprove the hypothesis that the ratio of the gate and focus voltages in general determines spot size. What is probably happening is that higher current corresponding to larger gate bias is driving a greater part of the image area into saturation, which produces a seemingly larger spot.

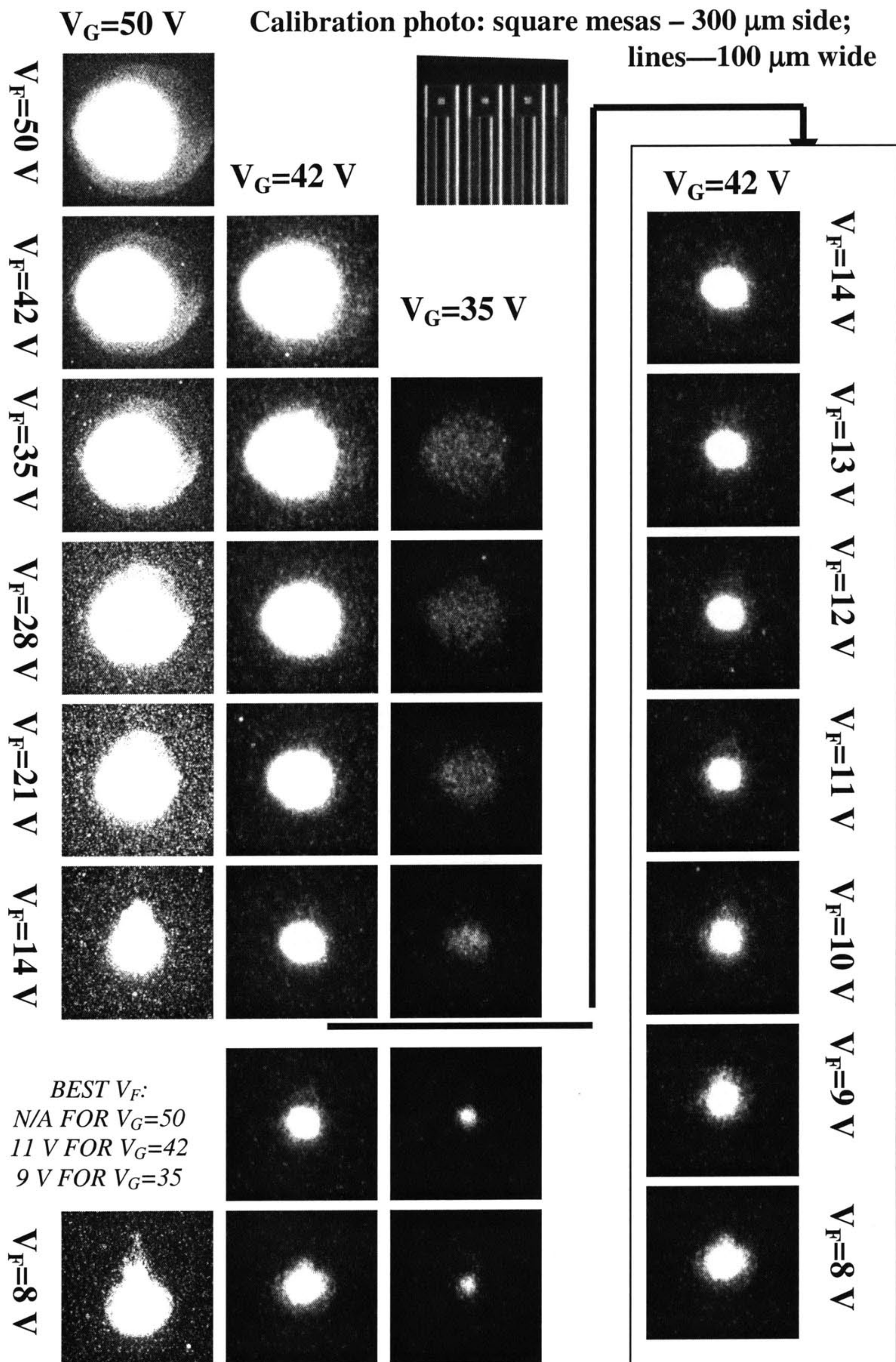

V_G=50 V
Calibration photo: square mesas – 300 μm side;
lines—100 μm wide
V_G=42 V
V_G=35 V
V_G=42 V
V_F=50 V
V_F=42 V
V_F=35 V
V_F=28 V
V_F=21 V
V_F=14 V
V_F=8 V
V_F=14 V
V_F=13 V
V_F=12 V
V_F=11 V
V_F=10 V
V_F=9 V
V_F=8 V
BEST V_F:
N/A FOR V_G=50
11 V FOR V_G=42
9 V FOR V_G=35

(continued from the previous page)

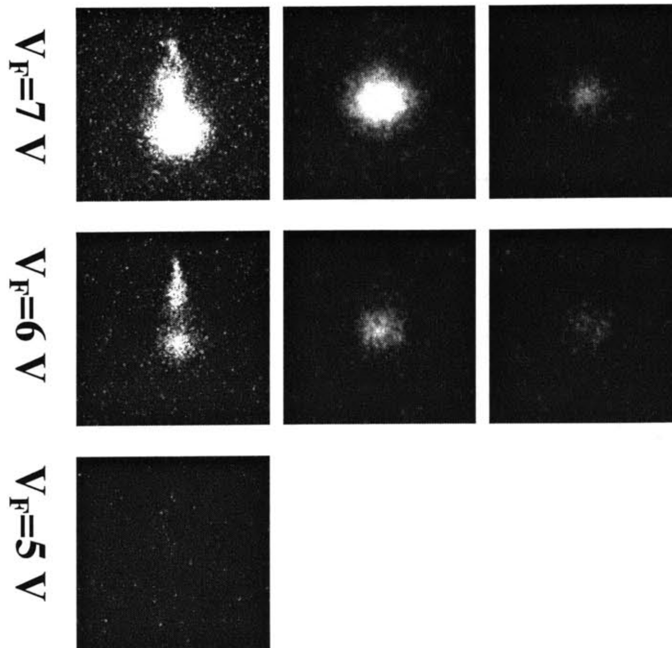

Figure 6-3. Variation of spot size with focus voltage at different values of the gate voltage.

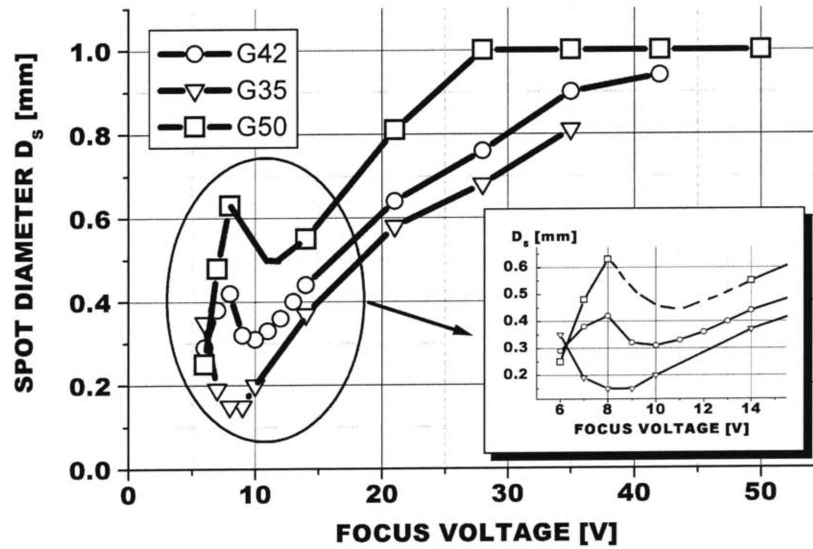

Figure 6-4.. Spot size at different values of gate and focus voltages. V_A=8kV; d_A= 10mm.

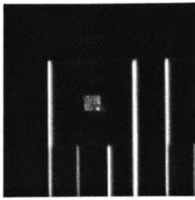

1.1.1.1 Calibration photo: square mesas – 300 μm side;

h=15 mm h=12.5 mm h=10 mm h=7.5 mm

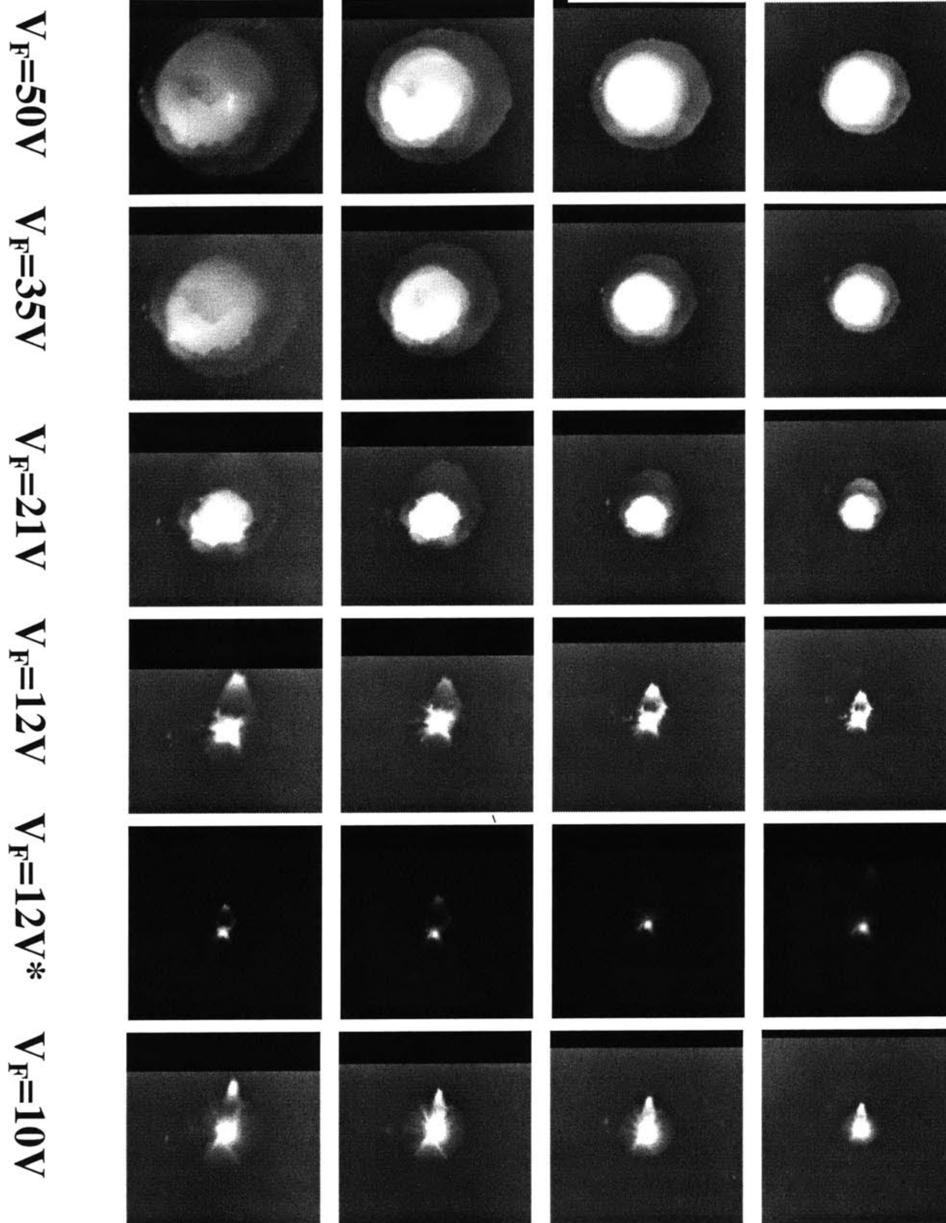

* This row shows photos with the original contrast and brightness. Contrast and brightness of all other photos were adjusted in Adobe Photoshop (to +6% Brightness, +90% Contrast) to ensure legible printout of photos of large, dim spots.

Figure 6-5. At the optimal value of focus bias, spot size is independent of anode height, which implies perfect collimation of the electron beam. At *lower* values of the bias, there is evidence of spot broadening due to beam crossover. V_A=5kV, V_G=50V, 1 sec exposure.

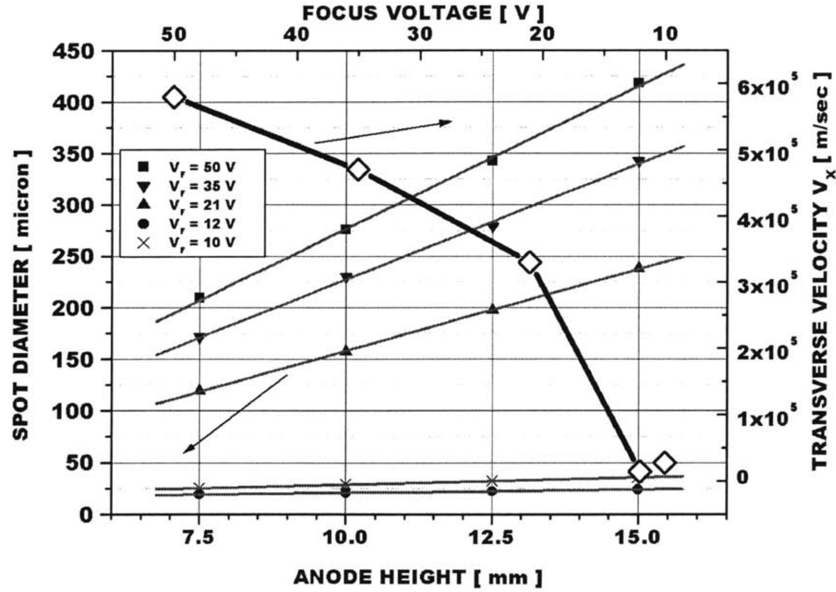

Figure 6-6. Slope of spot size vs. anode height gives asymptotic horizontal velocity, v_X. Reduction of v_X is beam collimation.

6.3 Collimation of the Electron Beam at Different Values of Cathode-Anode Separation — Reduction of Horizontal Velocity

For the analysis in this section, it is useful to think in terms of electrons' horizontal velocity. As we discussed in Chapter 1, when an electron is emitted at a non-zero angle, it acquires a certain horizontal velocity due to the roughly spherical field at the field emitter tip. This velocity is then increased by the horizontal electric field that exists up to several gate radii away from the tip. This field is produced by the positive charge on the gate electrode and is directed toward the z-axis. When the electron is more than ~10 gate radii away from the tip, a distance that rarely exceeds 10 μm, the horizontal field is almost zero and the electron travels to the anode under the influence of the uniform anode field. Its horizontal velocity, v_X, remains constant, and it hits the screen a distance $\Delta x = v_x \Delta t$ away from the axis of symmetry, where Δt is the travel time to the anode. The horizontal displacement acquired by the electron while in the range of the gate field is typically considerably less than 10 μm and can be neglected. Furthermore, the kinetic energy acquired by the electron in region of the gate field is less than eV_G, which is typically on the order of 50eV. The associated vertical velocity can be neglected for the purposes of computing Δt, which is then given by:

$$d_A = \frac{1}{2}\frac{e V_A}{m\, d_A}(\Delta t)^2 \quad \Rightarrow \Delta t = d_A\sqrt{\frac{2m}{e V_A}} \quad \Rightarrow \Delta x = v_x d_A \sqrt{\frac{2m}{e V_A}} \qquad \textbf{(6.1)}$$

where d_A is anode height (cathode-anode separation). By taking the horizontal velocity to be independent of d_A, we are assuming that the anode field is negligible in the region of the gate field, which is a good approximation. Δx is effectively a measure of spot size, which is thus proportional to anode height. Note also that the phosphor response, and hence spot size, depends on anode voltage but not on anode field.

Figure 6-5 shows images of spot size as a function of anode height at different values of the focus voltage. At the optimal collimation voltage (V_F=12V), the spot size is seen to be practically independent of anode height, which implies that the electrons' horizontal velocity has been reduced to zero. Reduction of horizontal velocity with lower focus bias is summarized in **Figure 6-6**, which also demonstrates that spot size is a linear function of anode height, as we suggested. Spot size was measured in Adobe Photoshop and taken to equal to the diameter of the brightest innermost part of the image, neglecting any halos and aberrations. To facilitate measurements and to ensure legible printouts, contrast and brightness of all photos were adjusted in an identical fashion. Only at the point of optimal collimation contrast adjustment was unnecessary and in fact obscured the true spot geometry. For this case both original and contrast adjusted photos are shown in **Figure 6-5**, with the former being used for spot size measurements. At V_F=12V, the spot size so measured is a somewhat unbelievable 25 μm diameter at 7.5 mm anode height and 31 μm at 15 mm anode height, which suggests that the horizontal velocity has been reduced practically to zero. The size of the original array is 40x40 μm^2 if all the tips are emitting, and 20x20 μm^2 if the tips on the periphery are not active. SEM micrographs showed greatly increased defect density around array periphery. We suspect it results from the CMP steps.
Assuming half of all anode current is concentrated in the bright central spot that was taken to define the spot size, we can estimate current density as

$$\frac{1}{2}\frac{250\,10^{-9}A}{\left(25 10^{-3}mm\right)^2} = 0.2 \,{}^{mA}\!\big/_{mm^2}$$

Incidentally, comparison of the data in **Figure 6-4** and **Figure 6-6** may appear to contradict our argument that spot size goes inversely with the square root of anode voltage. For example, according to **Figure 6-4**, the spot size for V_G=50 V, V_F=50 V, d_A=10 mm, and V_A=8 kV is 1 mm. However, according to **Figure 6-6**, the same parameters but with V_A=5 kV produce a spot that is only 0.42 mm in diameter. The explanation, aside from the differences in image acquisition that we have already discussed, has to do with the phosphor. The phosphor emits more light per unit charge when the anode voltage is higher. In general, the phosphor begins to emit light at about 5 kV, gets progressively brighter until about 10 kV, and remains constant thereafter.

In addition to the bright circular spot, some of the images in **Figure 6-3** and **Figure 6-5** show a vertical "petal" along the positive z-axis. The petal, which is probably present in all images though obscured by excessive background brightness, does not respond well to focusing. We suspect it is due to a defective focus electrode or two on the tips along the upper periphery of the array. SEM inspections showed an increased density of defects along array boundaries, which can be traced to a different polishing rate in this area during the CMP steps in the fabrication process. It would make sense to design arrays such that tips around the periphery are dummy pillars that do not emit. It would also be desirable to increase packing density, which should produce more a

uniform spot for given array area. For example in the present devices, tips are positioned on 10 μm spacing, and the area of a 5x5 array is 50x50 μm^2. With 4-5 μm spacing, 10x10 arrays would fit in this footprint.

6.4 Chapter Summary

This chapter demonstrated how lowering the focus bias reduces the diameter of the light spot produced on the phosphor screen by the electron beam. Strong evidence of beam collimation by the focus electrode was presented. We went beyond what has been reported in the literature in several aspects.

First, we presented a detailed discussion of the uncertainties and errors inherent in spot size measurement, related these to the experimental apparatus, and suggested that in the absence of a charge counter, the optimal spot size measurement requires one to start with large (e.g. 20x20) arrays to ensure spot uniformity, use a low-noise digital camera with timed exposure to capture the image, and then do automated processing on image files.

We examined beam collimation at different values of gate voltage and observed that spot size changes only slowly until the focus voltage is reduced significantly below the gate voltage. This pattern, which is also present in the data reported by others, probably occurs because spot size doesn't really begin to decrease until the charge on the focus electrode becomes negative. The optimal focusing voltage is also lower for lower gate voltage. This was again interpreted in terms of the negative charge on the focus electrode and compared to predictions from numerical simulations. We also observed, in agreement with simulations, an increase in spot size when the focus bias is reduced below the optimal value. This effect is due to "overfocusing."

Finally, we showed the spot size is proportional to cathode-anode separation, with the constant of proportionality being a multiple of the electron's horizontal velocity. Using measurements of spot size at different values of anode height, we were able to extract the horizontal velocity and demonstrate that it is effectively reduced to zero when the optimal bias voltage is applied to the focus electrode.

7 Thesis Summary and Suggestions for Further Work

7.1 Thesis Summary

This work deals with design, modeling, fabrication, and characterization of field emitter arrays with either a single gate or a stacked double gate. The latter configuration is referred to as field emitter with integrated focus, or IFE-FEA. The main application of this device is producing collimated electron beams to improve the resolution of high-voltage field emission displays (FEDs).

An original analytical model (the Bowling Pin Model, or BPM) of device electrostatics is developed and used to extract an expression for the emission current as a function of voltage and device geometry for single-gated field emitters. In other words, the model provides closed-form expressions for the Fowler-Nordheim slope and intercept (**Equations 3-42, 3-43**):

$$a_{FN} = -8.5 + Log\left[\alpha' C_G'^{2}\right] + 2\nu_0 Log\left[\frac{R_T}{R_G}\right] + 2Log\left[\frac{\nu_0 + (1+\nu_0)\gamma^{1+2\nu_0}}{1-\delta}\right]$$

$$b_{FN} = -59\frac{R_G^{\nu_0} R_T^{1-\nu_0}}{C_G'\left(\nu_0 + (1+\nu_0)\gamma^{1+2\nu_0}\right)}(1-\delta)$$

R_T is tip radius of curvature (ROC) in *nm*;

R_G is the gate radius in *nm*, measured as the distance from the tip to the gate. The equations above have been confined to the case of the gate co-planar with the tip – though the BPM is completely general in this respect – since it is the most common. In this case, R_G is equal to half the gate diameter.

$0.2 < \nu_0 < 0.4$ ($\nu_0 = 0.2$ will be used in fitting data)

$0.4 < \gamma < 0.6$ describes how close the tip is to the shape of a sphere

$$\delta \approx 0.92 C_G' \left(\frac{R_T}{R_G}\right)^{\nu_0} \left(1-\gamma^{1+2\nu_0}\right)$$

$$Log(\alpha') \approx -2$$

The only adjustable parameter is the gate capacitance, C_G', which can also be approximated analytically. The model is extended to double-gated field emitters (IFE-FEA) where it is used to generalize the Fowler-Nordheim equation to the case of IFE-FEA and then derive expressions for the gate and focus field factors. (**Equation 3-54**).;

The IFE-FEA extension also made it possible to compute electron trajectories at different values of the focus bias, illustrating the desired collimation effect (**Figure 3-10**).

A novel process for making IFE-FEA is presented (**Figure 4-1**). The process is self-aligned and relies on deposition, planarization via chemical-mechanical polishing (CMP), and etchback of low temperature oxide (LTO) layers. It achieved devices with gate and focus apertures of 0.8 and 1.2 μm diameter, respectively (**Figure 5-13A**). These dimensions are 1.5 times smaller than those of any previously reported IFE-FEA. There is strong evidence that with a few simple modifications, gate and focus apertures can be reduced by an additional factor of 2 (**Figure 4-7A, 4-9C, and 4-10**)

To facilitate the measurements, single-gate devices (SG-FEAs) were also fabricated, with gate geometry identical to that of the IFE-FEAs (**Figure 5-2B, 5-13B**). Per tip emission currents in SG-FEAs were about 100 nA at 45 V (**Figure 5-7A**), corresponding to the FN slope and intercept of –500 and –12.7 (**Figure 5-7B – 5-9**), respectively. Total emission current scaled closely with array size, suggesting a high degree of tip-to-tip uniformity. Gate current was less than 5%, and in most cases less than 1%, of the anode current. Device simulation using finite element method and implemented in Matlab was used to deduce the tip radius of curvature (ROC) at the apex from the FN slope (**Figure 5-10**). The value for ROC calculated with this method was 3.7 nm. Tip ROC as measured from TEM micrographs were in the range 2.6 – 3.8 nm (**Figure 5-11**). Tip ROC was also calculated with BPM by setting the analytical expressions for a_{FN} and b_{FN} equal to the measured values and solving for ROC and the gate capacitance, which is the adjustable parameter (**Equation 5-6**). The ROC obtained from this procedure was 2.7 nm (**Equation 5-7),** and the value for the capacitance was found to be in good agreement with analytical approximations. Thus, the BPM becomes the first analytical model capable of extracting the tip ROC from the measured FN parameters via closed form expressions.

For IFE-FEAs with the gate and focus biased at the same voltage, FN slope was between –423 and –515, and the FN intercept was between –11.7 and –12.9 (**Figure 5-14 – 5-16**). This suggests that the tip ROC in IFE-FEAs is very similar to that in the single gate devices. It was also observed that the FN slope of the focus current was equal to the FN slope of the anode current, which implies that part of the emission current (about 50%) is intercepted by the focus (**Appendix II**).

Gate and focus transfer characteristics of IFE-FEAs were measured (**Figure 5-17 – 5-19**). The FN equation was generalized to the case of IFE-FEAs (**Equation 5-15**) and used to extract the values of gate and focus field factors, which to the best of our knowledge constitutes an original contribution. It was found that the focus field factor was either less, comparable to, or greater than that of the gate (**Table 5-1**). The latter situation, corresponding to emission current being largely independent of the focus voltage, is the most desirable. It was speculated that these differences result from tips of different height that end up either shielded by the gate or protruding far above the gate (**Figure 5-24 – 5-25**). This was confirmed by numerical simulations (**Figure 5-26, Table 5-2**). Device in which the emission current was largely independent of the focus voltage was

used for measurements of the collimation effect. Finally, complete suppression of the emission current was observed when the focus voltage dropped below 6 V **(Figure 5-17 – 5-19)**. This feature, which has been reported in the literature, cannot be explained by the FN equation or by space charge arguments that have been put forth . We propose that it occurs when the bias on the focus is too low to overcome its workfunction barrier and collect electrons; the electron trajectories are then reversed and return to the emitter tip, suppressing the emission field **(Figure 5-29)**.

The most significant result of this work is measurements of the collimation of the electron beam by the focus electrode, presented in **Chapter 6**. Whereas earlier work provided only variation of spot size with focus voltage at one value of gate voltage, we have explored two other variables: collimation of the beam at different values of the gate voltage (**Section 6-2**) and at different values of cathode anode separation (**Section 6-3**). Collimation measurements at different values of the gate voltage demonstrated that the optimal focusing voltage is lower for lower values of gate voltage; the optimal V_F / V_G ratio was about 0.25 **(Figure 6-5)**. Results of simulations reported in the literature predicted that this ratio would be 0.35. It was also observed that when the focus voltage is lowered below the optimal value, the spot size increases again **(Figure 6-5)**. This is also in agreement with reported simulations and results from "overfocusing." Measurements of spot size vs. cathode-anode separation at different values of the focus voltage showed that when the beam is optimally collimated, spot size remains virtually the same as the anode height is increased **(Figure 6-6)**. It was further demonstrated, that this data can be used to compute the final horizontal velocity of electrons **(Equation 6-1)**. At the point of optimal beam collimation (V_G = 42 V, V_F = 11 V) the horizontal velocity was practically zero **(Figure 6-7)**, and the total spot diameter did not exceed 50 μm **(Figure 6-7)**, when the emitting area (i.e. array footprint) was between 20x20 and 40x40 μm^2.

7.2 Main Contributions

At the risk of repeating ourselves, here again is a brief list of the main contributions of this work:

1. The first analytical model of conical field emitters that captures all details of device geometry and produces closed-form expressions for the FN coefficients that allow extraction of the tip radius-of-curvature (ROC) from the measured FN slope and intercept. Results for tip ROC calculated from this model are in excellent agreement with both TEM micrographs and numerical simulations.

2. An original process for fabricating IFE-FEAs. As executed, the process produced devices with dimensions that were 1.5 times smaller than any IFE-FEA previously reported. There is strong evidence that with a few simple modifications the process could reduce IFE-FEA dimensions by at least an additional factor of 2.

3. Generalizing the FN equation to the case of IFE-FEA by introducing a new parameter – the focus field factor, β_F. Using 4-terminal measurements (i.e. transfer characteristics) of IFE-FEA to determine the values of the gate and focus field factors.

4. Study of electron beam collimation at different values of the gate voltage. Demonstration of the decrease in the optimal focus voltage with gate voltage.

5. Study of electron beam collimation at different values of cathode-anode separation – a novel experiment. This data made it possible to compute the final horizontal velocity of electrons, which is useful and intuitive measure of beam collimation.

6. With the anode at biased at 5kV and positioned 15 mm away, the size of the spot produced by the collimated beam was approximately equal to the footprint of the array. In other words, all beam divergence has been eliminated.

7.3 Suggestions for Further Work

A direct extension of our work would be to repeat the experiment with a greater level of accuracy. To start with, emitter arrays would be fabricated with a smaller pit (4-5 micron is sufficient), so that 10x10 – 20x20 arrays fit within 100 μm^2. Since we found that all defects are concentrated around array periphery, presumably due to a different rate of polish, new array design should replace the outer two rows of tips with non-emitting pillars. A station to test oxide breakdown during the intermediate stages of the fabrication process located in the cleanroom would help immensely to get predictable yield and low gate current. These devices should be modeled with the 3D FEA simulation tool that was developed in our group. On the metrology side, one would want to calibrate the phosphor response at different anode voltages and different anode currents. Then, stable current from relatively large IFE-FEAs can be expected to produce very uniform circular light spots on the phosphor screen. Images taken with a low-noise camera, at a timed exposure and with careful control of all relevant parameters, can be analyzed in digital form. Ultimately, this can be expected to produce for the first time quantitative agreement between measured and simulated spot size.

On a more applied note, the fabrication technology can be advanced from this point in two different directions: simplify the process for the same structure or fabricate more complicated electron structures. We have described the electron lenses that are potential candidates for miniaturization. However, practically speaking, this work may not be warranted for the display application, until it is determined that existing IFE-FEAs are insufficient. To make our process simpler, the main challenge is to simplify the step of opening the gate aperture. At present it requires each wafer to be examined under the SEM multiple times. It may be possible to do the oxide etch in a conducting solution, in an electroplating kind of setup, that would automatically indicate once the gate electrode has been exposed.

8 APPENDIX 1.

Mathematica Code to Compute Tip Radius of Curvature Based on the Values of FN Coefficients a_{FN} and b_{FN}.

```
<< Graphics`Graphics`
<< Statistics`DataManipulation`
<< Graphics`Graphics3D`
<< Graphics`MultipleListPlot`

(*==========================================================================
  READ IN VALUES OF LEGENDRE DEGREES ( idx = nu_k ), NORMALIZATION COEFFICIENTS
  (Ak = A_k), LEGENDRE FUNCTIONS OF DEGREES nu_0 THROUGH nu_200 (MyLegendreP),
 AND LEGENDRE FUNCTIONS OF DEGREES (nu0 - 1) THROUGH (nu200-1) (MyLegendreP2)
  ==========================================================================*)

idx = << idx.m;
Ak  = << Ak.m;
xc = Cos[Pi 17/18];
e = 1.6 10^-19;
m = 9.1 10^-31;

MyLegendreP = Table[0, {200}];
MyLegendreP2 = Table[0, {200}];
For[i = 1, i ≤ Length[MyLegendreP], i++,

  If[i ≤ 125, nt = 1800, nt = 909];

  filename = "pol" <> ToString[i] <> ".m";
  res = Get[filename];
  data = Transpose[{Table[1 - 0.0011 j, {j, 0, nt}], Take[res, nt + 1]}];
  MyLegendreP[[i]] = Interpolation[data];
  If[Mod[i - 1, 99] == 0, Print[i]; ListPlot[data, PlotJoined → True]];

  filename = "pol" <> ToString[i] <> "m1.m";
  res = Get[filename];
  data = Transpose[{Table[1 - 0.0011 j, {j, 0, nt}], Take[res, nt + 1]}];
  MyLegendreP2[[i]] = Interpolation[data];
  If[Mod[i - 1, 99] == 0, Print[i]; ListPlot[data, PlotJoined → True]];

 ];
```

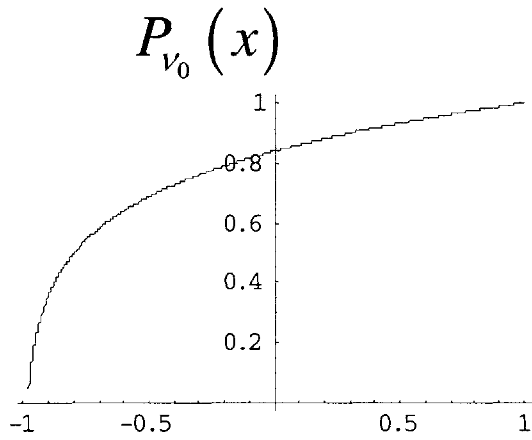

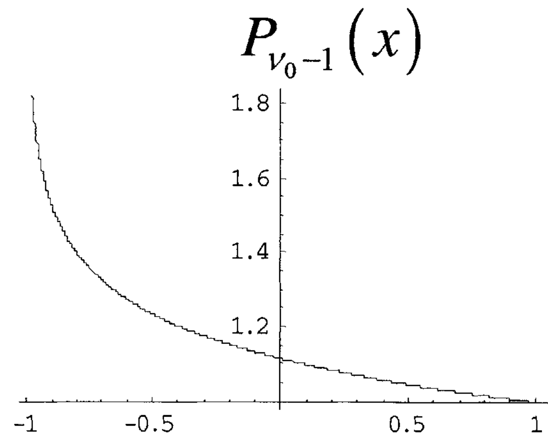

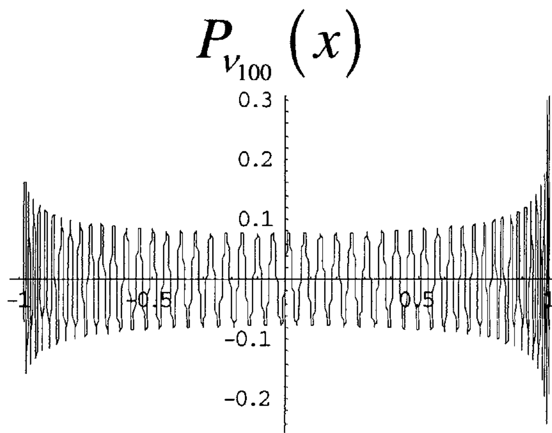

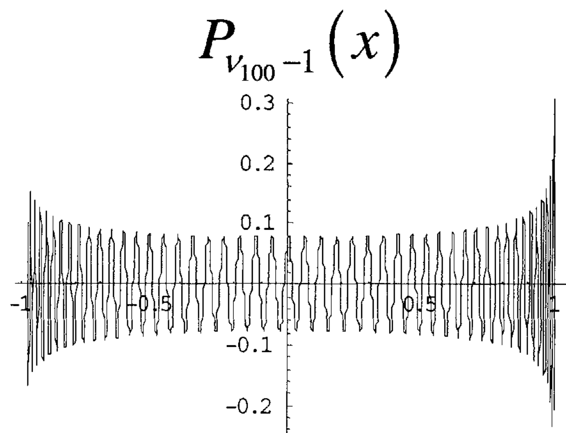

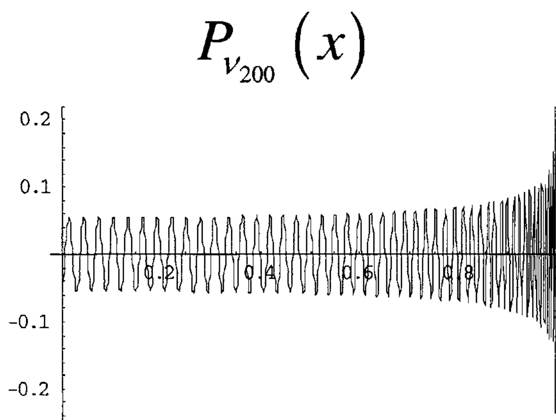

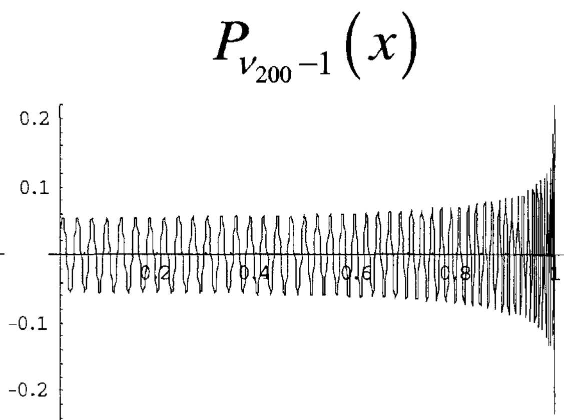

Note: For reasons I don't fully understand, computation of Legendre functions when $x<0$ is very slow; thus, for higher orders computation was confined to $x>0$, which is sufficient for the purposes of BPM.

```
Rg = 250;
alldata = Table[0, {40}, {6}];

(* 'k1' SETS THE TIP RADIUS OF CURVATURE (ROC) *)
For[k1 = 1, k1 ≤ 10, k1++,
 ROC = 2 k1;

 (* 'k2' SETS THE TIP ECCENTRICITY (gamma = s1) *)
 For[k2 = 1, k2 ≤ 4, k2++,
  allctr = 4 (k1 - 1) + k2 ;
  s1 = If[k2 > 0, 0.2 k2, 0.00001];
  Rt = s1 ROC;

  (* DEFINE VOLTAGE;  THE NUMBER OF TERMS IS SET TO TRUNCATE
     THE SUM WHEN ' (r/Rg)^nu_max ≤10^-5',  UP TO THE MAXIMUM
    OF 200 TERMS.  LINEAR INTERPOLATION IS USED BETWEEN
    0.96 Rg AND 1.4 Rg *)

  V[r_?NumberQ, x_?NumberQ] :=

   Which[
    r ≤ 0.96 Rg,
    Sum[ Ak[[k]] * MyLegendreP[[k]][0.0017453] * MyLegendreP[[k]][x] *
      ( (r/Rg)^idx[[k]] -
        Rt^(2*idx[[k]] + 1) / Rg^idx[[k]] / r^(idx[[k]] + 1) ),
     {k, 1, Min[200,  Ceiling[N[ 5 Log[10] / Log[Rg/r]]] ]}
    ],

    r < 1.04 Rg,
    ((260 - r) V[240, x] + (r - 240) V[260, x]) / 20,

    r ≥ 1.04 Rg,
    Sum[ Ak[[k]] * MyLegendreP[[k]][0.0017453] * MyLegendreP[[k]][x] *
      (  (r/Rg)^ -(idx[[k]] + 1) -
        Rt^(2*idx[[k]] + 1) / (Rg^idx[[k]]) / r^(idx[[k]] + 1) ),
     {k, 1, Min[200, Ceiling[N[ 5 Log[10] / Log[ r / Rg ] ] ]  ]}
    ]
   ];
```

```
(*==  DEFINE RADIAL AND ANGULAR ELECTRIC FIELDS, Er AND Ea,
   AS FUNCTIONS OF SPHERICAL COORDINATES r AND x=Cos[theta]) ==*)

Er[r_?NumberQ, x_?NumberQ] :=
  -(1 / r) *
   Which[
    r <= 0.96 Rg,
    Sum[ Ak[[k]] * MyLegendreP[[k]][0.0017453] * MyLegendreP[[k]][x] *
       ( idx[[k]] * (r / Rg) ^idx[[k]] + (idx[[k]] + 1) *
          Rt^(2 * idx[[k]] + 1) / Rg^idx[[k]] / r^(idx[[k]] + 1) ),
     {k, 1, Min[200,  Ceiling[N[ 5 Log[10] / Log[Rg / r]]] ]}
    ],
    r < 1.04 Rg,
    -r * ((260 - r) Er[240, x] + (r - 240) Er[260, x]) / 20,
    r ≥ 1.04 Rg,
    Sum[ Ak[[k]] * MyLegendreP[[k]][0.0017453] * MyLegendreP[[k]][x] *
       ( -(idx[[k]] + 1) * (r / Rg) ^ -(idx[[k]] + 1)  + (idx[[k]] + 1) *
          (Rt^(2 * idx[[k]] + 1)) / (Rg^idx[[k]]) / r^(idx[[k]] + 1) ),
     {k, 1, Min[200, Ceiling[N[ 5 Log[10] / Log[ r / Rg ] ] ]  ]}
    ]
   ]
 ;

Ea[r_?NumberQ, x_?NumberQ] :=
  -(1 / r) *
   Which[
    r <= 0.96 Rg,
    Sum[ Ak[[k]] * MyLegendreP[[k]][0.0017453] *
       ((x idx[[k]] MyLegendreP2[[k]][x] -
          idx[[k]] MyLegendreP[[k]][x]) / (1 - x x) ^0.5) *
       ( (r / Rg) ^ idx[[k]]  - Rt^(2* idx[[k]] + 1) / Rg^idx[[k]] / r^(idx[[k]] + 1) ),
     {k, 1, Min[200, Ceiling[N[ 5 Log[10] / Log[Rg / r]] ] ]  }
    ],
    r < 1.04 Rg,
    -r * ((260 - r) Ea[240, x] + (r - 240) Ea[260, x]) / 20,
    r ≥ 1.04 Rg,
    Sum[ Ak[[k]] * MyLegendreP[[k]][0.0017453] *
       ((x idx[[k]] MyLegendreP2[[k]][x] -
          idx[[k]] MyLegendreP[[k]][x]) / (1 - x x) ^0.5) *
       ( (r / Rg) ^ -(idx[[k]] + 1)  -
         Rt^(2 * idx[[k]] + 1) / Rg^idx[[k]] / r^(idx[[k]] + 1) ),
     {k, 1,  Min[200, Ceiling[N[ 5 Log[10] / Log[ r / Rg ] ] ] ] }
    ]
   ]
 ;
```

```
(*============= DEFINE THE TIP SURFACE (EQUIPOTENTIAL), =============
   ELECTRIC FIELD ALONG THE TIP SURFACE, AND THE EXPRESSION FOR J[E] ====*)

V0 = V[ROC, 1];
tip = Table[{1 - 0.01 j, z /. FindRoot[V[z, 1 - 0.01 j] == V0,
      {z, 0.9 * ROC, 1.2 ROC}]}, {j, 0, 120}];
tipfn = Interpolation[tip];
tipxy = Table[{tip[[i, 2]] * (1 - tip[[i, 1]] ^2) ^0.5,
    tip[[i, 2]] * tip[[i, 1]]}, {i, 1, Length[tip]}];
trange = Max[Abs[tipxy]];

Etip = Table[{ArcCos[tip[[i, 1]]] 180 / Pi, (Er[tip[[i, 2]],
         tip[[i, 1]]] ^2 + If[! i == 1, Ea[tip[[i, 2]], tip[[i, 1]]] ^2, 0]) ^0.5},
   {i, 1, Length[tip]}];

wf = 4.04;
j[E_] := (1.27273 10^-6 Exp[9.86814 / Sqrt[wf]] / wf) E^2
   * Exp[(-6.5265 * wf^1.5) / E];

nIV = 6;
IVdata = Table[{0, 0}, {nIV + 1}];
dV = 5;

(*== FIND THE VALUE OF THE CAPACITANCE 'CAP' THAT WOULD YIELD THE MEASURED
    B_FN VALUE AND THEN COMPUTE I (V) FOR V=20 TO 50 V IN STEPS OF dV=5;
 E is in V/nm; J is in A / nm^2 ==*)

BFN = 500;
CAP = (V0 + BFN * Abs[Etip[[1, 2]]] / (6.5265 * wf^1.5) ) ^-1;
For[ctr = 0, ctr ≤ 6, ctr++,
  Vg = ctr * dV + 20;
  jtip = Table[{Etip[[i, 1]] Pi / 180,
     j[CAP * Vg / (1 - CAP V0) * Etip[[i, 2]] ]}, {i, 1, Length[Etip]}];
  jfn = Interpolation[jtip];
  Itot = 2 Pi * NIntegrate[ tipfn[mu] ^2 * jfn[ArcCos[mu]], {mu, -0.2, 1}];
  IVdata[[ctr + 1]] = {N[1 / Vg], Log[Itot / Vg^2]};
 ];
```

```
(* FIT FN DATA TO A LINE AND OBTAIN FN COEFFICIENTS *)
    fit2 = Fit[IVdata, {1, x}, x];
    afn2 = FullForm[fit2][[1, 1]];
    bfn2 = FullForm[fit2][[1, 2, 1]];
    FormulaCoef =
      {-11.7 + Log[Itot / (2 Pi ROC^2 jfn[0]) * CAP^2] +
        0.4 Log[ROC / Rg] + 2 Log[(1 + 6 s1^1.4) / (1 - CAP V0)],
       -295 Rg^0.2 ROC^0.8 / (CAP* (1 + 6 s1^1.4)) * (1 - CAP V0)
      };
    Print[ ROC, "          ", s1, "          ", afn2, "          ",
     bfn2, "          ", CAP, "          ", FormulaCoef];
    alldata[[allctr]] = {ROC, s1, SetPrecision[afn2, 3], SetPrecision[bfn2, 3],
       CAP, SetPrecision[FormulaCoef, 3]};
   ];

  Print[];
 ];
Print[TableForm[alldata, TableDepth → 2]];
```

Summary of calculated results for R_G = 250 nm, b_{FN} = -500 V.
Measured parameters: -9 < a_{FN} < 8; -550 < b_{FN} < -500

ROC	gamma	a_{FN}	b_{FN}	C's.t. B=500	Eq.3-42,43 { a_{FN}, b_{FN} }
2	0.2	-12.7	-527.	1.1804	{-13.2 , -509. }
2	0.4	-12.5	-525.	0.887136	{-13.0 , -509. }
2	0.6	-12.2	-524.	0.679453	{-12.7 , -509. }
2	0.8	-11.9	-522.	0.535965	{-12.4 , -510. }
4	0.2	-11.2	-527.	1.5074	{-11.8 , -505. }
4	0.4	-11.1	-525.	1.26621	{-11.6 , -507. }
4	0.6	-10.8	-524.	1.05827	{-11.3 , -508. }
4	0.8	-10.5	-522.	0.891367	{-11.0 , -508. }
6	0.2	-10.4	-527.	1.6481	{-10.9 , -501. }
6	0.4	-10.2	-525.	1.48558	{-10.7 , -505. }
6	0.6	-9.94	-523.	1.32552	{-10.4 , -506. }
6	0.8	-9.66	-522.	1.18111	{-10.1 , -506. }
8	0.2	-9.76	-527.	1.71685	{-10.3 , -497. }
8	0.4	-9.61	-525.	1.62513	{-10.1 , -502. }
8	0.6	-9.33	-523.	1.52585	{-9.82 , -504. }
8	0.8	-9.05	-521.	1.42782	{-9.51 , -504. }
10	0.2	-9.26	-527.	1.75201	{-9.77 , -493. }
10	0.4	-9.12	-525.	1.71921	{-9.61 , -499. }
10	0.6	-8.84	-523.	1.68165	{-9.32 , -502. }
10	0.8	-8.57	-521.	1.6428	{-9.01 , -502. }
12	0.2	-8.83	-527.	1.76966	{-9.32 , -488. }
12	0.4	-8.71	-524.	1.78528	{-9.18 , -496. }
12	0.6	-8.44	-522.	1.80612	{-8.90 , -499. }
12	0.8	-8.17	-520.	1.83309	{-8.59 , -499. }
14	0.2	-8.45	-527.	1.77756	{-8.91 , -483. }
14	0.4	-8.35	-524.	1.83313	{-8.81 , -493. }
14	0.6	-8.09	-522.	1.9077	{-8.53 , -497. }
14	0.8	-7.82	-520.	2.00351	{-8.23 , -497. }
16	0.2	-8.10	-527.	1.77977	{-8.54 , -478. }
16	0.4	-8.02	-524.	1.86863	{-8.46 , -490. }
16	0.6	-7.77	-521.	1.99207	{-8.19 , -494. }
16	0.8	-7.52	-519.	2.15762	{-7.89 , -494. }
18	0.2	-7.77	-526.	1.77861	{-8.18 , -473. }
18	0.4	-7.73	-523.	1.89552	{-8.15 , -487. }
18	0.6	-7.49	-521.	2.06328	{-7.89 , -492. }
18	0.8	-7.24	-518.	2.29813	{-7.59 , -492. }
20	0.2	-7.44	-526.	1.77543	{-7.83 , -468. }

Results for γ = 0.4 only.

2	0.4	-12.5	-525.	0.887136	{-13.0 , -509. }
4	0.4	-11.1	-525.	1.26621	{-11.6 , -507. }
6	0.4	-10.2	-525.	1.48558	{-10.7 , -505. }
8	0.4	-9.61	-525.	1.62513	{-10.1 , -502. }
10	0.4	-9.12	-525.	1.71921	{-9.61 , -499. }
12	0.4	-8.71	-524.	1.78528	{-9.18 , -496. }
14	0.4	-8.35	-524.	1.83313	{-8.81 , -493. }
16	0.4	-8.02	-524.	1.86863	{-8.46 , -490. }
18	0.4	-7.73	-523.	1.89552	{-8.15 , -487. }
20	0.4	-7.45	-522.	1.91626	{-7.84 , -483. }

Summary of calculated results for R_G = 400 nm, B_{FN} = -500 , γ = 0.4.
Measured parameters: -9 < A_{FN} < 8; -550 < B_{FN} < -500

2	0.4	-12.5	-525.	0.973693	{-13.0 , -510. }
4	0.4	-11.1	-525.	1.38768	{-11.6 , -509. }
6	0.4	-10.3	-525.	1.6257	{-10.8 , -507. }
8	0.4	-9.66	-525.	1.77577	{-10.2 , -506. }
10	0.4	-9.19	-525.	1.87572	{-9.71 , -505. }
12	0.4	-8.80	-525.	1.9448	{-9.32 , -503. }
14	0.4	-8.47	-525.	1.99376	{-8.97 , -501. }
16	0.4	-8.18	-525.	2.02908	{-8.67 , -499. }
18	0.4	-7.91	-524.	2.05485	{-8.40 , -498. }
20	0.4	-7.67	-524.	2.07378	{-8.15 , -496. }

Simulation of Dave Pflug's devices.

R_G = 40 nm,
γ = 0.4.
B_{FN} = -230;
A_{FN} (per tip) = Log[0.4/500^2]=-13.35

1	0.4	-11.8	-251.	0.759146	{-12.2 , -232. }
1.5	0.4	-10.9	-251.	0.94426	{-11.3 , -230. }
2.	0.4	-10.3	-250.	1.08138	{-10.7 , -228. }
2.5	0.4	-9.77	-250.	1.18729	{-10.1 , -226. }
3.	0.4	-9.33	-249.	1.2717	{-9.67 , -223. }
3.5	0.4	-8.94	-248.	1.34072	{-9.24 , -221. }
4.	0.4	-8.59	-246.	1.3984	{-8.84 , -218. }
4.5	0.4	-8.28	-244.	1.44753	{-8.45 , -215. }
5.	0.4	-7.98	-241.	1.49013	{-8.08 , -212. }
5.5	0.4	-7.71	-238.	1.52767	{-7.72 , -209. }

9 Appendix II.
Details of Four-Terminal IV Data for IFE-FEA

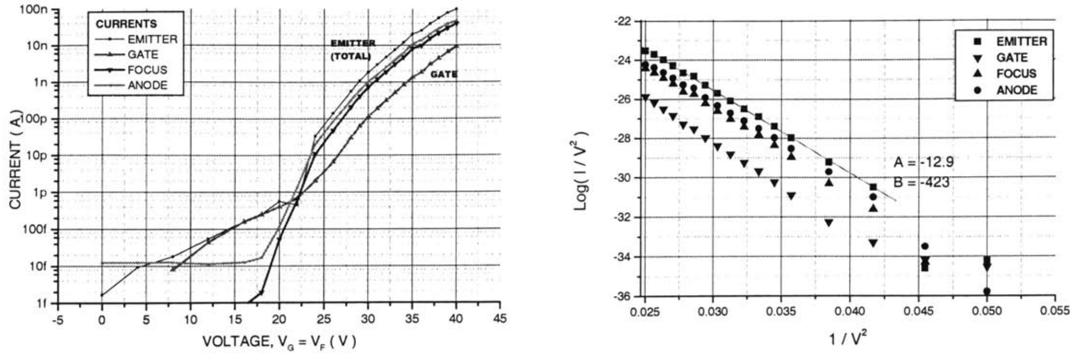

Figure AII-1. Log-Lin and FN plots of the Emitter, Gate, Focus and Anode currents per tip vs. Voltage (V_G=V_F) for a 10x10 FEA, D43NL10_2

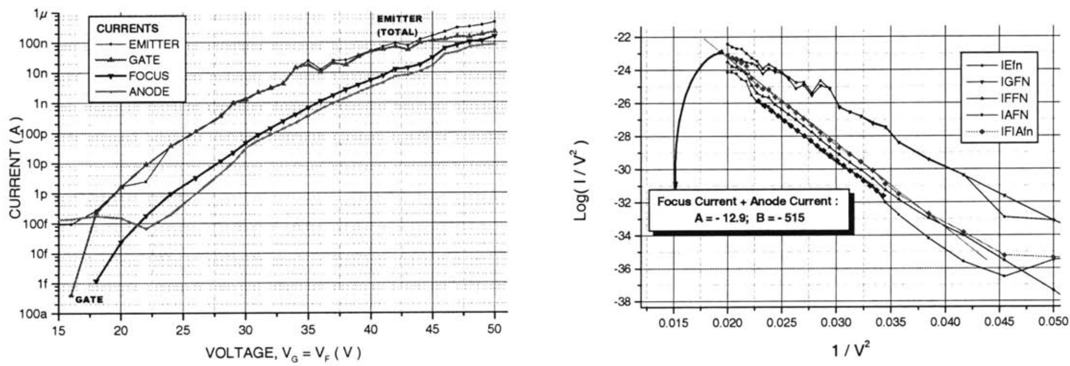

Figure AII -2. Log-Lin and FN plots of the Emitter, Gate, Focus and Anode currents per tip vs. Voltage (V_G=V_F) for a 5x5 FEA, D64L5_3

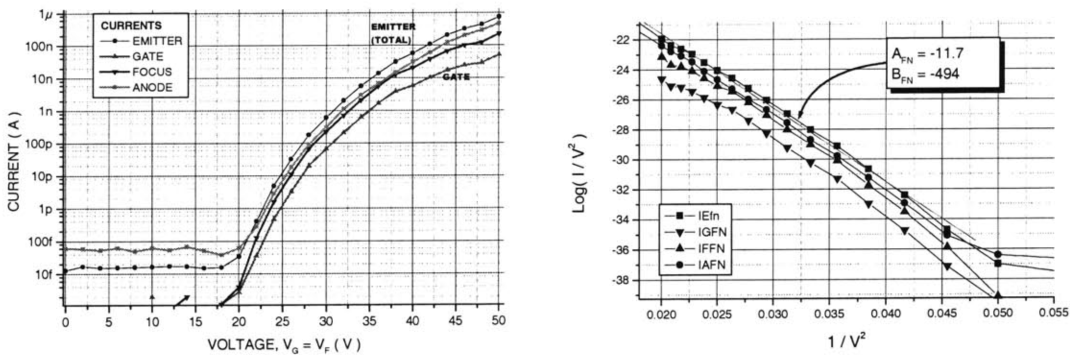

Fig

Figure AII -3. Log-Lin and FN plots of the Emitter, Gate, Focus and Anode currents per tip vs. Voltage (V_G=V_F) for a 5x5 FEA, D63L5_5.

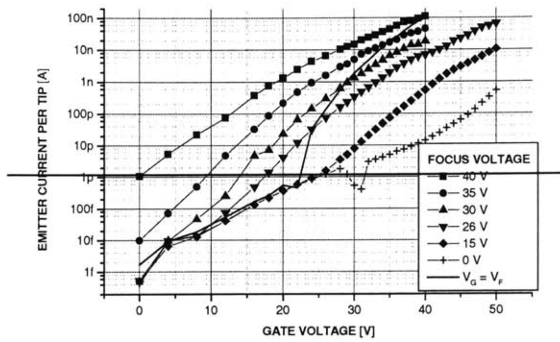

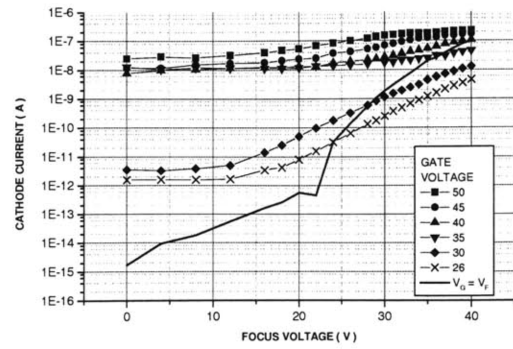

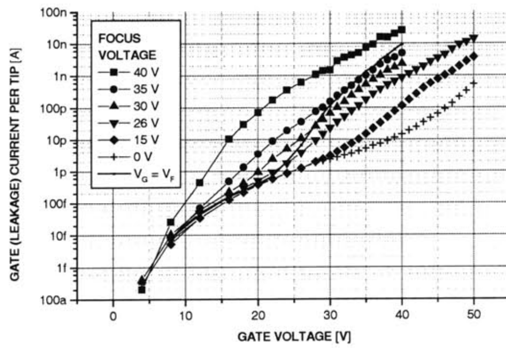

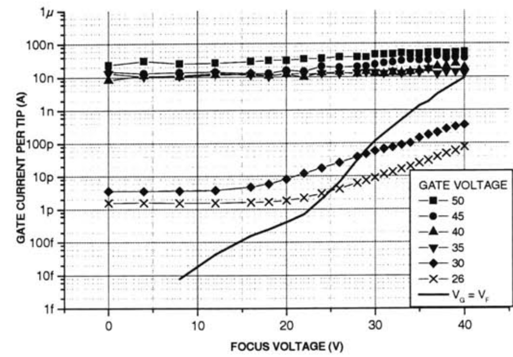

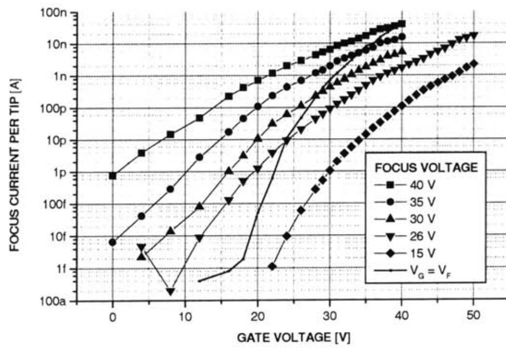

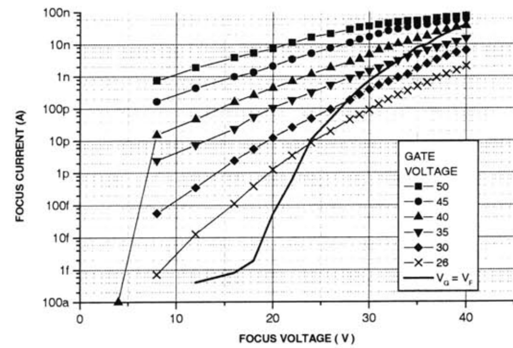

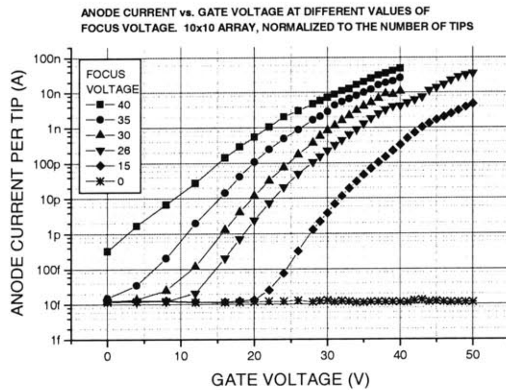

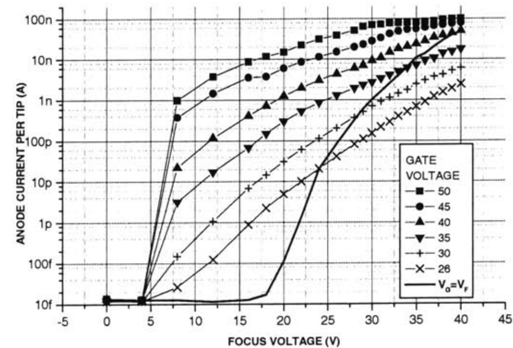

Figure AII -4. Raw IV data for a 10x10 FEA (D43NL10_2). Left Column: I_E, I_G, I_F, I_A vs. V_G at fixed V_F; Right Coluumn: I_E, I_G, I_F, I_A vs. V_F at fixed V_G.

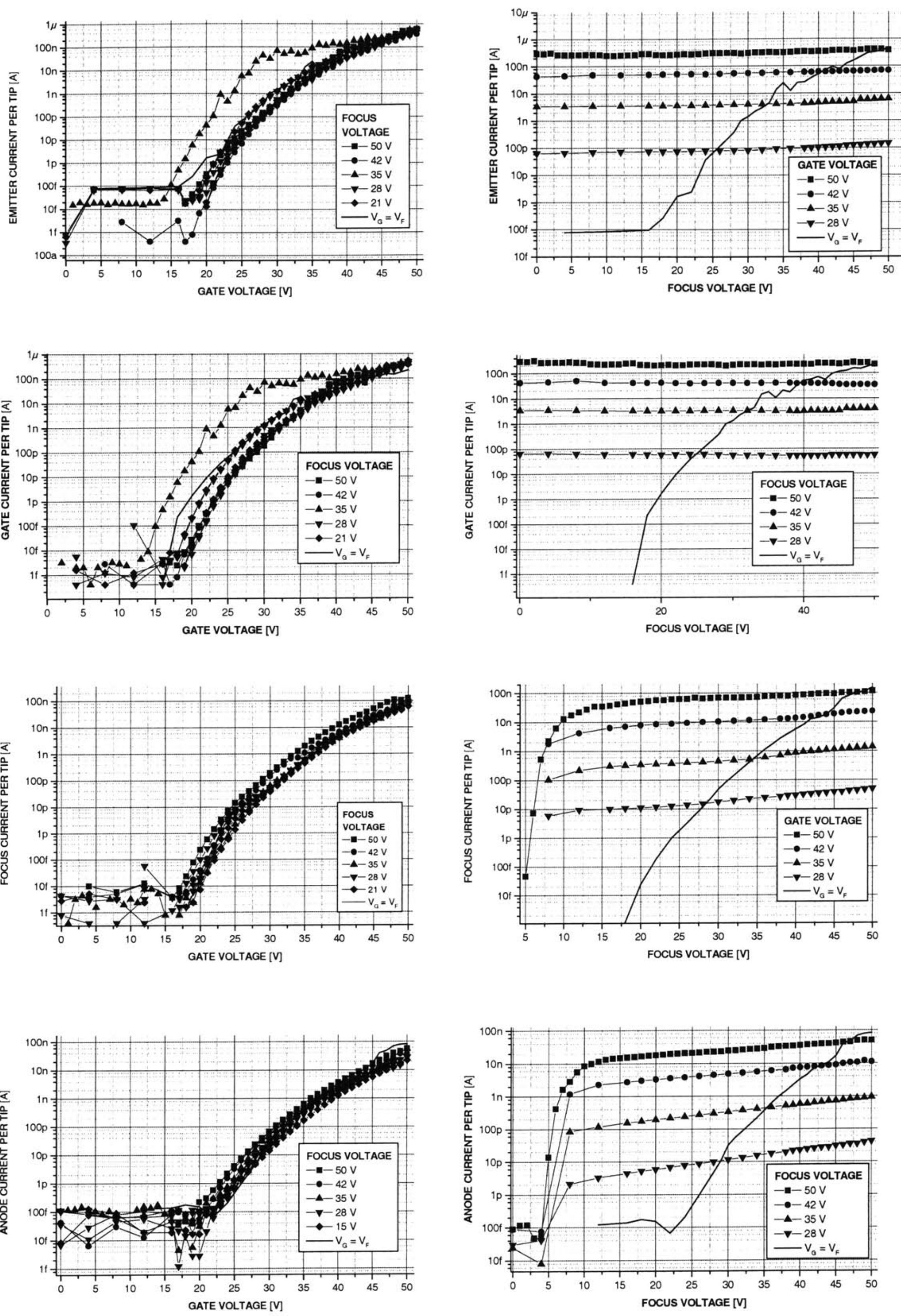

Figure AII -5. . Raw IV data for a 5x5 FEA (D64L5_3). Left Column: I_E, I_G, I_F, I_A vs. V_G at fixed V_F; Right Coluumn: I_E, I_G, I_F, I_A vs. V_F at fixed V_G.

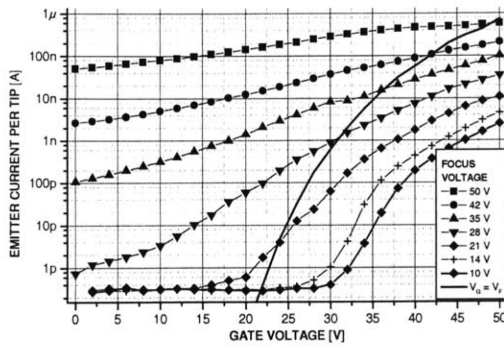

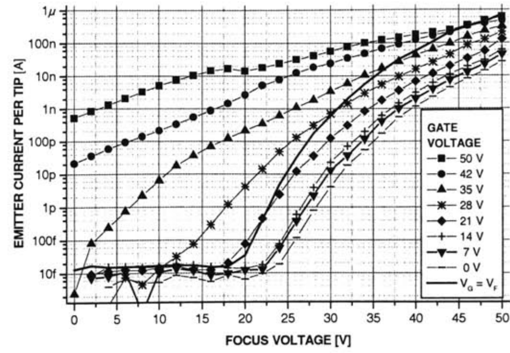

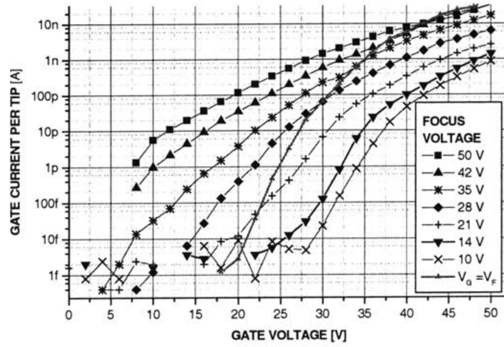

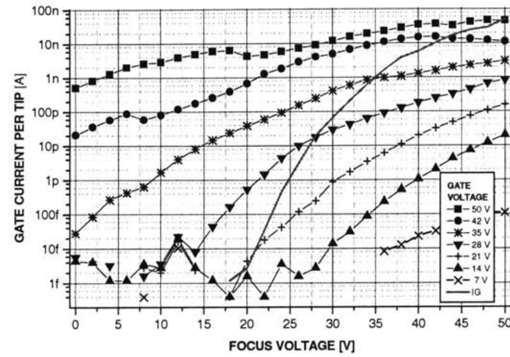

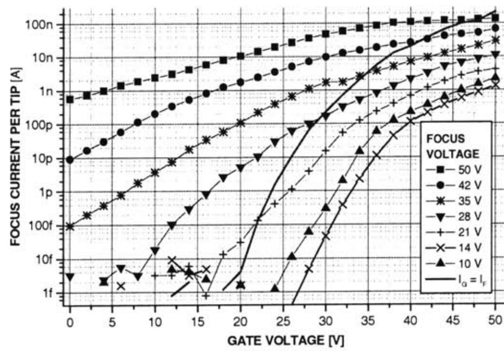

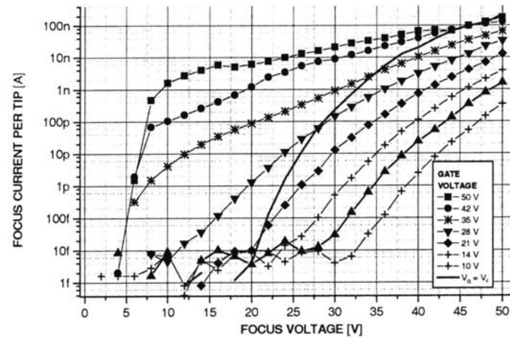

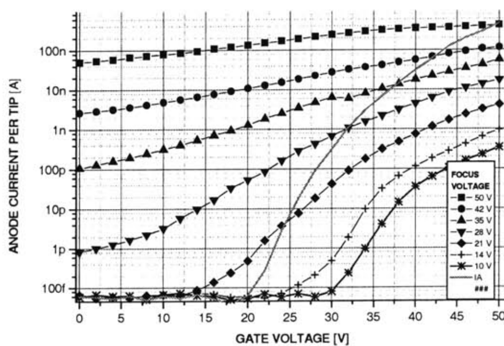

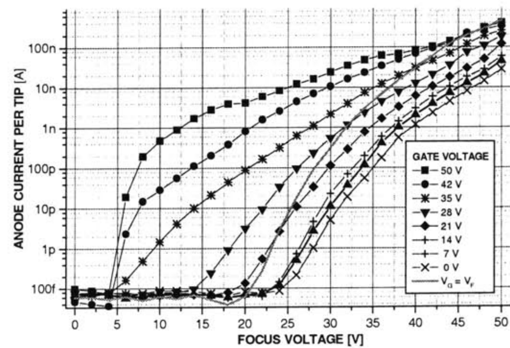

Figure AII-6. Raw IV data for a 5x5 FEA (D63L5_5). Left Column: I_E, I_G, I_F, I_A vs. V_G at fixed V_F; Right Coluumn: I_E, I_G, I_F, I_A vs. V_F at fixed V_G.

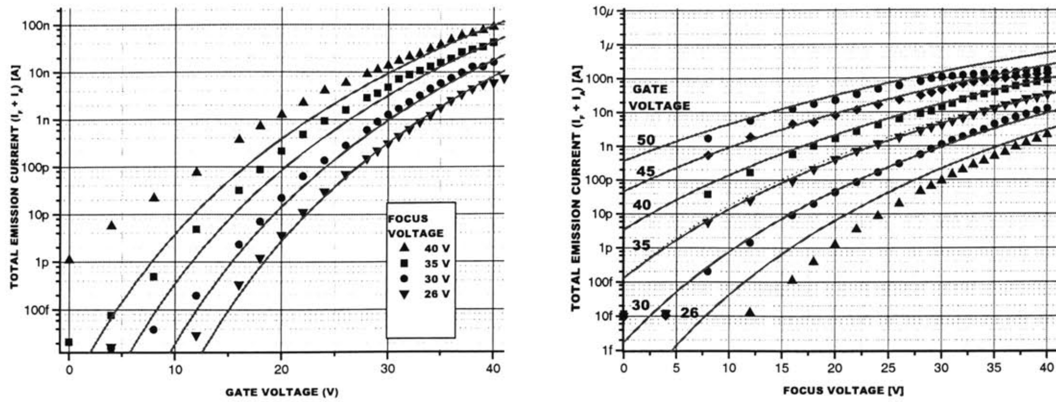

Figure AII -7. D43NL10_2. Emission current vs. Gate Voltage at fixed Focus Voltage (left) and vs. Focus Voltage at fixed Gate Voltage (right), with the least squares fit lines based on Equation (5.11). Data from the 10x10 FEA is more stable and is thus in better agreement with the model.

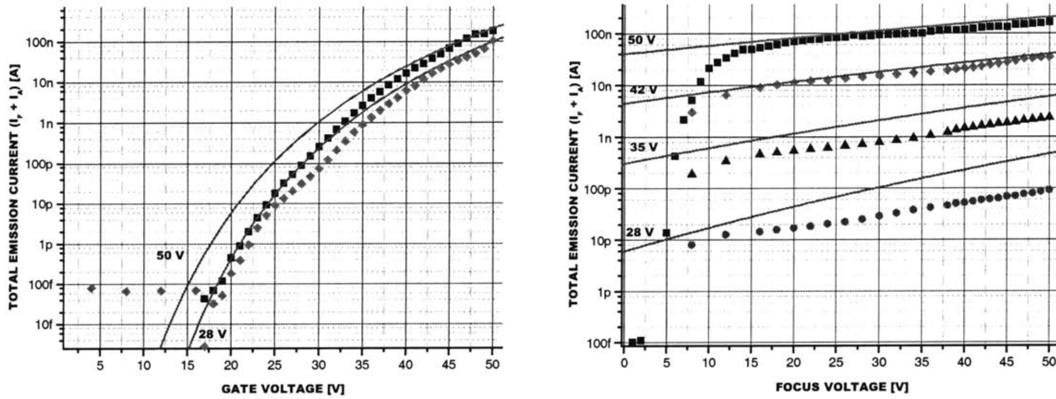

Figure AII -8. . D64L5_3. Emission current vs. Gate Voltage at fixed Focus Voltage (left) and vs. Focus Voltage at fixed Gate Voltage (right), with the least squares fit lines based on Equation (5.11). Data from the 5x5 FEA is noisy making for poorer agreement with the model.

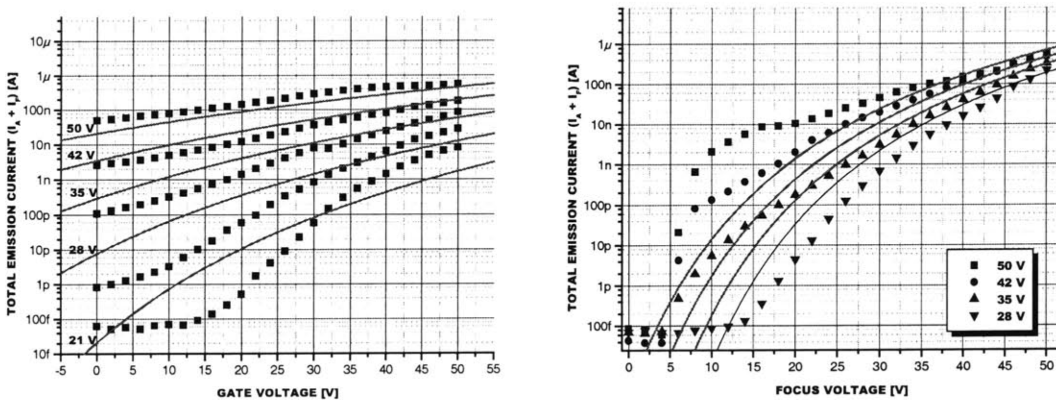

Figure AII -9. . D63L5_5. Emission current vs. Gate Voltage at fixed Focus Voltage (left) and vs. Focus Voltage at fixed Gate Voltage (right), with the least squares fit lines based on Equation (5.11). Data from the 5x5 FEA is noisy making for poorer agreement with the model.

Bibliography

[1] H. F. Gray, "State-of-the-art of field emission displays," *Int. Soc. Opt. Eng. Proceedings of SPIE*, vol. 3057, pp. 214-224,1997

[2] Pellizzari L., "From vacuum fluorescent display to field emission display," Elettronica Oggi, no.281, 15 Oct. 1999, pp.139-41. Publisher: Gruppo Editoriale Jackson, Italy.

[3] Talin AA. Chalamala B. Coll BF. Jaskie JE. Petersen R. Dworsky L., "Development of field emission flat panel displays at Motorola," Flat-Panel Display Materials - 1998. Symposium. Mater. Res. Soc. 1998, pp.175-7. Warrendale, PA, USA.

[4] Curtin C., "The field emission display: a new flat panel technology," Conference Record of the 1991 International Display Research Conference (Cat. No.91CH3071-8). IEEE. 1991, pp.12-15. New York, NY, USA.

[5] Ajluni C., "FED technology takes display industry by storm," Electronic Design, vol.42, no.22, 25 Oct. 1994, pp.56, 58, 60, 64, 66. USA.

[6] Petrovich T., "Industry trends favor low-power displays," Electronic Design, vol.43, no.1, 9 Jan. 1995, pp.95-6, 98, 100, 102. USA.

[7] "Cockpit Displays V: Displays for Defense Applications," SPIE-Int. Soc. Opt. Eng. Proceedings of Spie - the International Society for Optical Engineering, vol.3363, 1998, USA.

[8] Visinski JR., "Sunlight readable avionics displays," SPIE-Int. Soc. Opt. Eng. Proceedings of Spie - the International Society for Optical Engineering, vol.3363, 1998, pp.225-35. USA.

[9] Marticello DN. Hopper DG, "Insertion of field emission displays into high performance cockpits," SPIE-Int. Soc. Opt. Eng. Proceedings of Spie - the International Society for Optical Engineering, vol.2734, 1996, pp.32-7. USA.

[10] D. Temple, "Recent progress in field emitter array development for high performance applications," *Materials Science and Engineering Reports*, vol. R24, no. 5, pp. 185-239, Jan. 1999

[11] M. Ida, B. Montmayeul, and R. Meyer, "New microlithography technique for large size field emission displays," *Proceedings of the 16th SID International Research Conference*, pp. 177-180, 1996

[12] De Jule R, "Directions in flat-panel displays," Semiconductor International, vol.22, no.9, Aug. 1999, pp.75-6, 78, 80, 82. Publisher: Cahners Publishing, USA.

[13] Yoshida Y. Ishizuka A. Makishima H., "Present and future of vacuum fluorescent display and field emission display," Materials Chemistry & Physics, vol.40, no.4, May 1995, pp.267-72. Switzerland.

[14] Dance B., "Europe's FPD development offers a chance to compete. 2. Flat panel displays," Semiconductor International, vol.18, no.8, July 1995, pp.229-30, 232, 234. USA.

[15] Ghrayeb J. Jackson TW. Daniels R. Hopper DG, "Review of field emission display potential as a future (leap-frog) flat panel technology," SPIE-Int. Soc. Opt. Eng. Proceedings of Spie - the International Society for Optical Engineering, vol.3057, 1997, pp.237-48. USA.

[16] Wen-Chun Wang. Chun-Hui Tsai. Yui-Shin Fran. Chai-Yuan Sheu. Kuang-Lung Tsai. Hseu LK., "A high luminance FED with very low power consumption," SPIE-Int. Soc. Opt. Eng. Proceedings of Spie - the International Society for Optical Engineering, vol.3421, 1998, pp.69-76. USA.

[17] Palevsky A. Visinski JR., "Raytheon FED technology update," SPIE-Int. Soc. Opt. Eng. Proceedings of Spie - the International Society for Optical Engineering, vol.3057, 1997, pp.249-54. USA.

[18] Betsui K. Nakatani T., "Field emission display," Fujitsu, vol.49, no.3, 1998, pp.230-4. Publisher: Fujitsu, Japan.

[19] Shah I, "Field-emission displays," Physics World, vol.10, no.6, June 1997, pp.45-8. Publisher: IOP Publishing, UK.

[20] Giri R, "Field emitter display (FED) technology," SPIE-Int. Soc. Opt. Eng. Proceedings of Spie - the International Society for Optical Engineering, vol.2462, 1995, pp.66-74. USA.

[21] Meyer R., "Color field emission display: the ultimate flat CRT technology," IEE Colloquium on 'Novel Display Technologies'(Digest No. 1995/138). IEE. 1995, pp.2/1-3. London, UK.

[22] Park MY, Kim J, Lee DW, Park JS, Cho KI, Cho HJ. A 100 V, 10 mA high-voltage driver ICs for field emission display applications. [Conference Paper] *AP-ASIC'99. First IEEE Asia Pacific Conference on ASICs (Cat. No.99EX360). IEEE. 1999, pp.380-3. Piscataway, NJ, USA.*

[23] Young-Sun Na, Oh-Kyong Kwon, Chang-Ho Hyun, Jae-Won Choi. A new data driver circuit for field emission display. [Conference Paper] *Proceedings of the 18th. International Display Research Conference. Asia Display '98. Soc. Inf. Display (SID). 1998, pp.137-40. San Jose, CA, USA.*

[24] Kim JW, Hong SS, Choi JH, Kim SH, Kim JM. Driving method to improve display quality as current control with external circuitry. [Conference Paper] *Eleventh International Vacuum Microelectronics Conference. IVMC'98 (Cat. No.98TH8382). IEEE. 1998, pp.65-6. New York, NY, USA.*

[25] Smith RT. Drive approaches for FED displays. [Conference Paper] *Conference Record of the 1997 International Display Research Conference and International Workshops on LCD Technology and Emissive Technology. Soc. Inf. Display. 1997, pp.F35-41. Santa Ana, CA, USA.*

[26] Ho Young Song, Deog Kyoon Jeong, Jong Duk Lee. Current mode column driver for FED. [Conference Paper] *IVMC'97. 1997 10th International Vacuum Microelectronics Conference. Technical Digest (IEEE Cat. No.97TH8257). Electron. Display Ind. Res. Assoc. 1997, pp.701-5. Seoul, South Korea.*

[27] Peyre JF. Impact of the driving scheme on field emission displays performances. [Conference Paper] *Proceedings of the Sixteenth International Display Research Conference. SID's 16th International Display Research Conference. EURO DISPLAY. Soc. Inf. Display (SID). 1996, pp.169-72. New York, NY, USA.*

[28] Park S, Kim M. Fabrication method of spacers with high aspect ratio - used in a field emission display (FED). [Journal Paper] *Microsystem Technologies, vol.7, no.1, March 2001, pp.32-5. Publisher: Springer-Verlag, Germany.*

[29] Choi YS, Cha SN, Jung SY, Kim JW, Jung JE, Kim JM. Analysis for charged spacers in FED. [Journal Paper] *IEEE Transactions on Electron Devices, vol.47, no.8, Aug. 2000, pp.1673-7. Publisher: IEEE, USA.*

[30] Ma X, Sudarshan TS. High field performance of thin-wall spacers in a vacuum gap. [Journal Paper] *IEEE Transactions on Dielectrics & Electrical Insulation, vol.7, no.2, April 2000, pp.277-82. Publisher: IEEE, USA.*

[31] Xianyun Ma, Sudarshan TS. High field characteristics of dielectric spacers in thin-film electrode vacuum gaps. [Journal Paper] *Journal of Vacuum Science & Technology B, vol.17, no.4, July 1999, pp.1580-4. Publisher: AIP for American Vacuum Soc, USA.*

[32] Wada H, Kominami H, Kottaisamy M, Nakanishi Y, Hatanaka Y. Structure and low-voltage cathodoluminescent property of Y/sub 2/O/sub 3/:Tm thin film. [Journal Paper] *Bulletin of the Research Institute of Electronics, Shizuoka University, vol.35, 2000, pp.39-44.*

[33] Bolchouchine VA, Goldburt ET, Levonovitch BN, Litchmanova VN, Sochtine NP. Low voltage, blue phosphor for highly efficient field emission display screens. [Journal Paper] *Journal of Vacuum Science & Technology B, vol.19, no.1, Jan.-Feb. 2001, pp.14-16.*

[34] Sung Hee Cho, Seung Ho Kwon, Jae Soo Yoo, Chang Woo Oh, Jong Duk Lee, Kun Jo Hong, Sang Jik Kwon. Cathodoluminescent characteristics of a spherical Y/sub 2/O/sub 3/:Eu phosphor screen for field emission display application. [Journal Paper] *Journal of the Electrochemical Society, vol.147, no.8, Aug. 2000, pp.3143-7*

[35] Itoh S, Toki H, Kataoka F, Sato Y, Tamura K, Kagawa Y. Problems and present status of phosphors in low-voltage full-color FEDs. [Journal Paper] *IEICE Transactions on Electronics, vol.E82-C, no.10, Oct. 1999, pp.1808-13.*

[36] Jang JE, Jin YW, Jung JE, You YC, Park HS, Yi WK, Kim JM. Investigation of luminescent properties of low voltage phosphors for the FED applications. [Conference Paper] *Eleventh International Vacuum Microelectronics Conference. IVMC'98 (Cat. No.98TH8382). IEEE. 1998, pp.71-2.*

[37] Vecht A. Engineering phosphors for FEDs. [Conference Paper] *Eleventh International Vacuum Microelectronics Conference. IVMC'98 (Cat. No.98TH8382). IEEE. 1998, pp.51-2*

[38] Shea LE. Low-voltage cathodoluminescent phosphors. [Journal Paper] *Electrochemical Society Interface, vol.7, no.2, Summer 1998, pp.24-7*

[39] Bojkov C, Kumar N, Jacobsen SM, Yang S, Summers CJ. Considerations in selecting phosphors for low voltage FED applications. [Conference Paper] *Proceedings of Fifteenth International Display Research Conference. Asia Display '95. Inst. Telev. Eng. Japan & SID. 1995, pp.635-8.*

[40] Yang S, Stoffers C, Zhang F, Wagner BK, Penczek J, Jacobsen SM, Summers CJ. Low voltage properties of field emission display phosphors. [Conference Paper] *Proceedings of the Sixteenth International Display Research Conference. SID's 16th International Display Research Conference. EURO DISPLAY. Soc. Inf. Display (SID). 1996, pp.181-5*

[41] Jacobsen SM. Phosphors for full-color low-voltage field-emission displays. [Conference Paper] *Soc. Inf. Display. Journal of the Society for Information Display, vol.4, no.4, Dec. 1996, pp.331-5.*

[42] Chadha SS, Smith DW, Vecht A, Gibbons CS. New and improved phosphors for low-voltage applications. [Conference Paper] *1994 SID International Symposium Digest of Technical Papers. SID. SID. 1994, pp.51-4*

[43] R.H.Fowler and L. Nordheim, "Electron emission in intense electric fields," *Proceedings of the Royal Society of London*, Ser. A 119, pp. 173-181, Mar. 1928

[44] R. H. Good and E. W. Muller, "Field Emission," Handbook of Physics, vol. XXI, Springer 1956.

[45] P. W. Hawkes and E. Kasper, "Principles of Electron Optics," Vol. 2, Chapter 44, Academic Press 1989

[46] R. Stratton, *"Theory of Field Emission from Semiconductors,"* Phys. Rev. Vol 125, No. 1, Jan 1, 1962, pp. 67—82.

[47] K. L. Jensen, *"Exchange-correlation, dipole, and image charge potentials for electron sources: Temperature and field variation of the barrier height,"* J. of Appl. Physics, Vol. 85, No. 5, March 1 1999, pp. 2667—2680.

[48] P.H. Cutler, J. He, N. Miskovsky, T. Sullivan and B. Weiss, *"Theory of electron emission in high fields from atomically sharp emitters: Validity of the Fowler-Nordheim equation,"* J. Vac. Sci. Tech. B 11(2), Mar/Apr 1993, pp. 387—391.

[49] D. Pflug, "Low Voltage Field Emitter Arrays through Aperture Scaling," Ph. D. Thesis, MIT 2000

[50] W. B. Hermannsfeldt, R. Becker, I. Brodie, A. Rosengreen, and C. A. Spindt, Nucl. Intstrum. Methods A **298**, 39, (1990)

[51] P. W. Hawkes and E. Kasper, "Principles of Electron Optics," Volumes 1 and 2, Academic Press 1989.

[52] W. B. Hermannsfeldt, R. Becker, I. Brodie, A. Rosengreen, and C. A. Spindt, Nucl. Intstrum. Methods A **298**, 39, (1990)

[53] Py C, Itoh J, Hirano T, Kanemaru S. Beam focusing characteristics of silicon microtips with an in-plane lens. [Journal Paper] *IEEE Transactions on Electron Devices, vol.44, no.3, March 1997, pp.498-502.*

[54] Tang C-M, Swyden TA. "Analysis of beam collimation data from field-emitter arrays with linear planar lens." [Conference Paper] *IEEE Conference Record - Abstracts. 1996 IEEE International Conference on Plasma Science (Cat. No.96CH35939). IEEE. 1996, pp.255*

[55] Itoh J, Tohma Y, Morikawa K, Kanemaru S, Shimizu K. "Fabrication of double-gated Si field emitter arrays for focused electron beam generation." [Journal Paper] *Journal of Vacuum Science & Technology B, vol.13, no.5, Sept.-Oct. 1995, pp.1968-72.*

[56] Toma Y, Kanemaru S, Itoh J. "Electron beam characteristics of double-gated Si field emitter arrays." [Conference Paper] *IVMC '95. Eighth International Vacuum Microelectronics Conference. Technical Digest (Cat. No.95TH8012). IEEE. 1995, pp.9-13.*

[57] C.H. Tsai et al, SID 97 Digest, 10.2 (p. 119)

[58] L. Dvorson, "Field Emitters with Integrated Focusing Electrode," MS Thesis, MIT 1998

[59] L.Dvorson, A. I. Akinwande, *being published in JVST.*

[60] C. A. Spindt, I. Brodie, L. Humphrey, and E. R. Westerberg, "Physical properties of thin-film field emission cathodes with molybdenum cones," *Journal of Applied Physics*, vol. 47, pp. 5248-5263, Dec. 1976.

[61] R.H. Fowler and L. Nordheim, "Electron emission in intense electric fields," *Proceeding of the Royal Society of London*, Ser. A **119**, pp. 173-181, Mar. 1928

[62] P. H. Cutler, Jun He, N. M. Miskovsky, T. E. Sullivan, and B. Weiss, "Theory of electron emission in high fields from atomically sharp emitters: Validity of Fowler-Nordheim equation," *Journal of Vacuum Science and Technology*, B 11(2), pp. 387-391, Mar/Apr 1993

[63] D. Pflug, "Low Voltage Field Emitter Arrays through Aperture Scaling," Ph. D. Thesis, MIT 2000

[64] M. Ding, "Field Emission from Silicon," Ph. D. Thesis, MIT 2001

---

[65] D. Nicolaescu, "Physical basis for applying the Fowler-Nordheim J-E relationship to experimental I-V data," *Journal of Vacuum Science and Technology* G., vol. 11, pp. 392-395 (1993)

[66] G. N. A. van Veen, "Space-charge effects in Spindt-type field emission cathodes," *Journal of Vacuum Science and Technology*, vol. B 12(2), p. 655-661, Mar/Apr 1994

[67] R. N. Hall, "The Application of Non-Integral Functions to Potential Problems," *Journal of Applied Physics*, vol. 20, pp. 925-931, October 1949

[68] W. P. Dyke, J. K. Trolan, W. W. Dolan, and G. Barnes, "The field emitter: fabrication, electron microscopy, and electric field calculations," *Journal of Applied Physics*, vol. 24, pp. 570-576, May 1953

[69] J. A. Becker, "The use of field emission electron microscope in adsorption studies of W on W and Ba on W," *The Bell System Technical Journal*, pp. 907-932, Oct. 1951

[70] H. G. Kosmahl, "A wide-bandwidth high-gain small-size distributed amplifier with field-emission triodes (FETRODE's) for the 10 to 300 GHz Frequency Range," *IEEE Transactions on Electron Devices*, vol. 36, pp. 2728-2737, Nov.1989

[71] K. L. Jensen, E. G. Zaidman, M. A. Kodis, B. Goplen, D. N. Smithe, "Analytical and seminumerical model for gated field emitter arrays. I. Theory," *Journal of Vacuum Science and Technology* B 14(3), pp. 1942-1946, May/Jun 1996

[72] L. Dvorson, M. Ding, and A. I. Akinwande, "Analytical Electrostatic Model of Silicon Conical Field Emitters – Part I," IEEE Transactions on Electron Devices, vol. 48, No. 1, pp. 134-143, January 2001.

[73] M. Abramowitz and I. Stegan, *Handbook of Special Functions*, Dover Publications 1970.

[74] P. W. Hawker and E. Kasper, *Principles of Electron Optics Vol 2*, Academic Press 1989.

[75] E. W. Hobson, *The Theory of Spherical and Ellipsoidal Harmonics*, Chelsea Publ. Comp., 1965.

[76] Wolfram Research, Mathematica 4.0

[77] W. P. Dyke, J. K. Trolan, W. W. Dolan, and G. Barnes, "The field emitter: fabrication, electron microscopy, and electric field calculations," *Journal of Applied Physics*, vol. 24, pp. 570-576, May 1953

[78] Z.-H. Huang, P. H. Cutler, N. M. Miskovsky, and T. E. Sullivan, "Calculation of capacitance and electric field of a vacuum field effect device," *Journal of Vacuum Science and Technology*, vol. B 12(2), pp. 745-748 (1994)

[79] M. R. Rakhshandehroo and S. W. Pang, "Fabrication of self-aligned silicon field emission devices and effects of surface passivation on emission current," *Journal of Vacuum Science and Technology*, B 16(2), pp. 765-769, Mar/Apr 1998

[80] W. R. Smythe, *Static and Dynamic Electricity 2nd Ed.*, McGraw-Hill Book Comp., 1950

[81] M. Ding, "Field Emission from Silicon," Ph.D. Thesis, MIT 2001.

[82] W.D. Kesling and C.E. Hunt, "Beam Focusing for field-emission flat displays," *IEEE Transactions on Electron Devices*, vol. 42, no.2, pp. 340-347, Feb. 1995

[83] J. Itoh, Y. Tohma, K. Morikawa, S. Kanemaru, and K. Shimizu, "Fabrication of double-gated Si field emitter arrays for focused electron beam generation," *Journal of Vacuum Science and Technology*, vol. B 13(5), pp. 1968-1995, Sep/Oct 1995

[84] Nicolaescu D, Filip V, Itoh J. Electron-beam focusing and deflection properties for misaligned dual gate field emitters. [Journal Paper] *Japanese Journal of Applied Physics Part 1-Regular Papers Short Notes & Review Papers, vol.40, no.6A, June 2001, pp.3996-4001.*

[85] Nicolaescu D, Filip V, Itoh J. Field emitter magnetic sensor with steered focused electron beam. [Journal Paper] *Japanese Journal of Applied Physics Part 1-Regular Papers Short Notes & Review Papers, vol.40, no.4A, April 2001, pp.2173-7.*

[86] Zhuang Xuezeng, Xia Shanhong, Tao Xinxin. Double-gated field emitter arrays for microwave devices. [Conference Paper] *1997 Asia-Pacific Microwave Conference Proceedings APMC '97. Wireless Communication in the Era of Information (IEEE Cat. No.97TH8336). City Univ. Hong Kong. Part vol.2, 1997, pp.533-6 vol.2.*

[87] Ching-Wu Wang, Chih-Liang Chen, Yuan-Hsiu Yang, Tsung-Yu Yang. Simulation of geometric effects on double-gate field emission devices. [Conference Paper] *SPIE-Int. Soc. Opt. Eng. Proceedings of Spie - the International Society for Optical Engineering, vol.4079, 2000, pp.255-63.*

[88] Nicolaescu D, Filip V, Itoh J. Focusing properties of volcano-shaped dual-gate field emitters. [Journal Paper] *Japanese Journal of Applied Physics Part 1-Regular Papers Short Notes & Review Papers, vol.40, no.1, Jan. 2001, pp.83-6.*

[89] Qu Xiaosheng, Li Dejie, Yao Baolun. Simulation of electric field and electron trajectory of focus field emission arrays. [Journal Paper] *Zhenkong Kexue Yu Jishu Xuebao/Vacuum Science & Technology, vol.20, no.5, Sept.-Oct. 2000, pp.308-10.*

[90] Chenggang Xie, Lucero R, Dworsky L. Electrostatic analysis of field emitter arrays with focusing electrode using boundary element method. [Conference Paper] *Proceedings of the 18th. International Display Research Conference. Asia Display '98. Soc. Inf. Display (SID). 1998, pp.71-3.*

[91] L. Dvorson, M. Ding, and A. I. Akinwande, "Analytical Electrostatic Model of Silicon Conical Field Emitters – Part II: ," IEEE Transactions on Electron Devices, vol. 48, No. 1, pp. 134-143, January 2001.

[92] Meng Ding, Han Kim, Akinwande AI, "Highly uniform and low turn-on voltage Si field emitter arrays fabricated using chemical mechanical polishing," *IEEE Electron Device Letters, vol.21, no.2, Feb. 2000, pp.66-9.*

[93] D. Pflug, "Low Voltage Field Emitter Arrays through Aperture Scaling," Ph.D. Thesis, MIT 2001.

[94] M. Ding, "Field Emission from Silicon," Ph. D. Thesis, MIT 2001.

[95] L.Dvorson, "Field Emitters with Integrated Focusing Electrode," MS Thesis, MIT 1999.

[96] P. R. Schwoebel and I. Brodie, "*Surface-science aspects of vacuum microelectronics*," JVST B 13(4), Aug. 1995, pp. 1391—1410.

[97] C. B. Duke and M. E. Alferieff, J. Chem. Phys. 46, **923** (1966)

[98] J. Itoh et. al., "*Fabrication of double-gated Si field emitter arrays for focused electron beam generation*",
JVST B 13(5), Sep/Oct 1995

[99] C. Py, J. Itoh et. al., *"Beam Focusing Characteristics of Silicon Microtips with an In-Plane Lens,"* IEEE TED, Vol. 44, No. 3, March 1997

[100] K. Jensen, M.A. Kodis, R. A. Murphy, and E. G. Zaidman, *"Space Charge effects on the current-voltage characteristics of gated field emitter arrays,"* J. Appl. Phys. **82** (2), 15 July 1997, pp. 845-854.

[101] Y. Yang, *"Numerical Analysis and Design Strategy for Field Emission Devices,"* Ph. D. Thesis, MIT 1999.

3690 37